

# NAVAL POSTGRADUATE SCHOOL MONTEREY, CALIFORNIA



## THESIS

19960319  
11

### ULTRASONIC ACOUSTIC CHARACTERISTICS OF AIR BUBBLES IN THE SURF ZONE

by

Trevor A. McIntyre

September, 1995

Thesis Advisor:

Timothy P. Stanton

Approved for public release; distribution is unlimited.

## REPORT DOCUMENTATION PAGE

Form Approved OMB No. 0704-0188

Public reporting burden for this collection of information is estimated to average 1 hour per response, including the time for reviewing instruction, searching existing data sources, gathering and maintaining the data needed, and completing and reviewing the collection of information. Send comments regarding this burden estimate or any other aspect of this collection of information, including suggestions for reducing this burden, to Washington Headquarters Services, Directorate for Information Operations and Reports, 1215 Jefferson Davis Highway, Suite 1204, Arlington, VA 22202-4302, and to the Office of Management and Budget, Paperwork Reduction Project (0704-0188) Washington DC 20503.

1. AGENCY USE ONLY <i>(Leave blank)</i>	2. REPORT DATE	3. REPORT TYPE AND DATES COVERED
	September, 1995	Master's Thesis
4. TITLE AND SUBTITLE ULTRASONIC ACOUSTIC CHARACTERISTICS OF AIR BUBBLES IN THE SURF ZONE.		5. FUNDING NUMBERS
6. AUTHOR(S) Trevor Andrew McIntyre		
7. PERFORMING ORGANIZATION NAME(S) AND ADDRESS(ES) Naval Postgraduate School Monterey CA 93943-5000		8. PERFORMING ORGANIZATION REPORT NUMBER
9. SPONSORING/MONITORING AGENCY NAME(S) AND ADDRESS(ES)		10. SPONSORING/MONITORING AGENCY REPORT NUMBER
11. SUPPLEMENTARY NOTES The views expressed in this thesis are those of the author and do not reflect the official policy or position of the Department of Defense or the U.S. Government.		
12a. DISTRIBUTION/AVAILABILITY STATEMENT Approved for public release; distribution is unlimited.		12b. DISTRIBUTION CODE
13. ABSTRACT <i>(maximum 200 words)</i> Understanding the movement of sediment in the nearshore region due to wave motion and longshore currents is important in beach erosion studies, and has tactical significance in beach front mine warfare. In the surf zone, air bubbles and sediment are both suspended within the water column. At the Naval Postgraduate School in Monterey, California, a sediment flux probe has been developed to study small scale processes. Using ultrasonic acoustic backscatter, the Coherent Acoustic Sediment Flux Probe (CASP) is capable of tracking the movement of scatterers within the surf zone. As it is important that the CASP system is capable of distinguishing between sediment and entrained air bubbles, laboratory experiments were run to determine the ultrasonic acoustic backscatter characteristics of surf zone bubbles. Bulk void fraction and optical sizing methods were explored to develop a means of measuring bubble populations produced in the laboratory for calibration of the backscattered energy received by the CASP system in the presence of bubbles.		
14. SUBJECT TERMS Acoustics, Bubbles, Lasers, Optics, Void Fraction		15. NUMBER OF PAGES 119
		16. PRICE CODE
17. SECURITY CLASSIFICATION OF REPORT Unclassified	18. SECURITY CLASSIFICATION OF THIS PAGE Unclassified	19. SECURITY CLASSIFICATION OF ABSTRACT Unclassified
		20. LIMITATION OF ABSTRACT UL

NSN 7540-01-280-5500

Standard Form 298 (Rev. 2-89)  
Prescribed by ANSI Std. Z39-18 298-102



**Approved for public release; distribution is unlimited.**

**ULTRASONIC ACOUSTIC CHARACTERISTICS  
OF AIR BUBBLES IN THE SURF ZONE**

Trevor A. McIntyre  
Lieutenant, United States Navy  
B.S., United States Naval Academy, 1984

Submitted in partial fulfillment  
of the requirements for the degree of

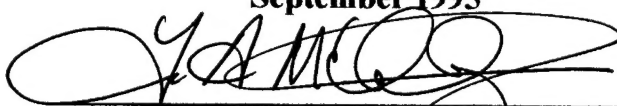
**MASTER OF SCIENCE IN PHYSICAL OCEANOGRAPHY**

from the

**NAVAL POSTGRADUATE SCHOOL**

September 1995

Author:



---

Trevor A. McIntyre

Approved by:



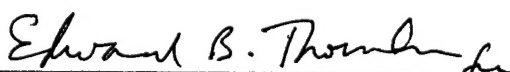
---

Timothy P. Stanton, Thesis Advisor



---

Edward B. Thornton, Second Reader



---

Robert H. Bourke, Chairman  
Department of Oceanography



## ABSTRACT

Understanding the movement of sediment in the nearshore region due to wave motion and longshore currents is important in beach erosion studies, and has tactical significance in beach front mine warfare. In the surf zone, air bubbles and sediment are both suspended within the water column. At the Naval Postgraduate School in Monterey, California, a sediment flux probe has been developed to study small scale processes. Using ultrasonic acoustic backscatter, the Coherent Acoustic Sediment Flux Probe (CASP) is capable of tracking the movement of scatterers within the surf zone. As it is important that the CASP system is capable of distinguishing between sediment and entrained air bubbles, laboratory experiments were run to determine the ultrasonic acoustic backscatter characteristics of surf zone bubbles. Bulk void fraction and optical sizing methods were explored to develop a means of measuring bubble populations produced in the laboratory for calibration of the backscattered energy received by the CASP system in the presence of bubbles.



## TABLE OF CONTENTS

I.	BACKGROUND.....	1
II.	EXPERIMENTAL PLAN AND DEVELOPMENT.....	5
	A. EXPERIMENTAL OUTLINE.....	5
	1. Development of Bubble Production System.....	5
	2. Selection of a Bubble Measurement System.....	5
	3. System Testing in Freshwater and Salt Water Filled Tanks.....	6
	B. EXPERIMENTAL SET-UP AND DEVELOPMENT.....	6
	1. Ocean Bubble Spectra Measurements.....	6
	2. Ocean Spectra Theory.....	13
	3. Laboratory Bubble Production Methods.....	15
	a. Electrolysis and Hypodermic Needles.....	15
	b. Underwater Jet Air Entrainment.....	15
	c. Above Water Jet Air Entrainment.....	16
	4. Bubble Production System Development.....	19
	5. Bubble Size Spectra Measurement.....	21
	a. Light Scattering Bubble Counter.....	22
	b. Photographic Bubble Imaging System.....	24
	c. Acoustic Resonator Array.....	25
	d. Laser Holography.....	27
	e. Coulter Counters.....	27
	6. Measurement Apparatus.....	28
	7. Optics Theory.....	31
	8. Geometrical Optical Approximations.....	38
III.	COHERENT ACOUSTIC SEDIMENT FLUX PROBE (CASP).....	41
VI.	ACOUSTIC EFFECTS OF AIR BUBBLES IN WATER.....	45
	A. BACKGROUND.....	45
	B. SOUND VELOCITY.....	45
	C. SOUND IN THE OCEAN.....	46

D. RESONANT BUBBLES.....	49
E. SCATTERING EFFECTS BY OCEAN BUBBLES.....	50
F. VOLUME REVERBERATION.....	51
G. BACKSCATTERED ENERGY.....	53
H. VOLUME BACKSCATTER MODEL.....	54
V. INITIAL EXPERIMENTAL TESTING.....	61
A. SINGLE NITROGEN BUBBLE TESTS.....	61
B. SINGLE REFLECTION METHODS.....	63
C. IMAGE PROCESSING.....	65
VI. EXPERIMENTAL RESULTS.....	67
A. BUBBLE PRODUCTION MEDIUM.....	67
1. Fresh Water.....	67
2. Simulated Sea Water.....	67
B. BUBBLE POPULATION VARIATION.....	69
C. OPTICAL BACKSCATTER RESULTS.....	70
D. CONDUCTIVITY CELL RESULTS.....	73
1. Calibration.....	73
2. Conductivity Results.....	76
E. BUBBLE PRODUCTION AND SPECTRA RESULTS.....	80
F. ACOUSTIC DATA.....	88
1. Backscattered Energy.....	88
2. Attenuation.....	89
3. Suspended Sediment Attenuation Comparison.....	91
VII. CONCLUSIONS.....	99
APPENDIX A. SPECIFICATION SHEET FOR OPTICAL BACKSCATTERANCE SENSORS.....	103
APPENDIX B. SPECIFICATION SHEET FOR CONDUCTIVITY CELLS.....	105
LIST OF REFERENCES.....	107
INITIAL DISTRIBUTION LIST.....	110

## I. BACKGROUND

The natural movement of coastal sand has long been documented and studied by coastal engineers, oceanographers and developers. The ability to predict and forecast the movement of sand and other bottom sediments within the surf zone can be environmentally, economically and tactically significant. In the development of coastal communities, man's efforts to protect and dredge channels and harbors has often adversely affected the longshore transportation of coastal sand and the natural evolution of barrier islands. Quite often, the efforts to protect man's investment in real estate and coastal structures has an adverse effect on the surrounding environment. During military operations, offensive and defensive mine warfare efforts can be seriously affected by the movement of sand.

The sand budget in a given coastal region is governed by a combination of sinks and sources of sand. Sinks can be either natural (submarine canyons, dunes, and aeolian transport), or man made (sand mining and harbor improvements such as jetties). Sources are primarily natural, in the form of cliff erosion and river runoff. As previously stated, natural sources and sinks balance each other reasonably well until man's influence distorts the balance.

Sand is transported throughout the surf zone by a variety of forcing mechanisms. Most dominant among these is movement due to wave forcing and longshore currents induced by deep water wave fronts breaking along the coastline obliquely. This forces a longshore component of momentum flux which, in turn, results in a longshore mass transport of sediment.

Locally, sand is known to move on and off shore, in a seasonal cycle, on some coastal beaches. For example, Carmel Beach, in central California, reaches maximum width in September and October. However, by April, it is quite narrow, almost non-existent. The sand which makes up the scenic and famous expanse of the beach in the late summer and early fall is transported off shore and deposited in a sand bar. The sand bar seems to be relatively constant and predictable in its location and depth. It is reasonable to assume that this movement of the beach sand is dependent on the frequency and amplitude of the waves, which are significantly different in the winter and

summer. Tactically, this offshore movement and formation of bars can be very significant during military operations. In the area of mine warfare, this movement can negate offensive mining efforts by scouring the concealing sand from around buried mines. This can, of course, lead to much simpler hunting and sweeping efforts. The effort of planting mines on a beach to contain an enemy force could be wasted if the beach is likely to vanish completely in a matter of weeks. Defensively, it is quite obviously easier to hunt and sweep exposed mines than buried mines. On the other hand, proud mines could end up being buried by the deposit of ephemeral beach sand, requiring that the time of planting these mines be chosen appropriately.

The underlying physical processes responsible for the movement of sand and sediment within the surf zone have been widely studied. However, the physical study of the movement of sediment within the surf zone is quite difficult. The surf zone itself is a highly turbulent and physically complicated region. A primary hurdle to scientific understanding of this region as it relates to sediment transport is the opacity, both visual and acoustic, of the water. The presence of bubbles entrained by breaking waves makes it difficult to track sediment movement. Without the presence of bubbles, it would be a relatively simple matter to study sand movement visually from above or, or acoustically *in situ*. In reality, however, the presence of bubbles makes visual tracking of sand nearly impossible and acoustic tracking quite difficult. Tactically, the opacity of the region makes it very difficult to detect and sweep mines within the surf zone. The presence of strong scattering conditions due to high concentrations of both sediment and bubbles severely reduces the utility of acoustic mine countermeasures systems.

There is a need to measure the physical processes contributing to surf zone sediment movement, which can resolve the small scale turbulent processes responsible for sediment suspension and transport. These studies would provide data concerning the nature of sand transport, and could eventually lead to tactical improvements in the areas of surf zone mine warfare and mine countermeasures. In an effort to develop a method to track and predict the movement of coastal sand, a series of experiments were conducted on the beaches of Duck, North Carolina, a few miles north of Kitty Hawk. The experiments of DUCK 94 utilized the Coherent Acoustic Sediment Probe (CASP) developed by Professor Timothy P. Stanton at the Naval Postgraduate School in

Monterey, California to conduct acoustic observations of the movement of entrained sediment in the surf zone, (Stanton [1993]). The CASP system uses ultrasonic acoustic backscatter information to track the movement of scatterers (sand particles, bubbles, and biotics in the water column). The capabilities of the CASP system will be discussed in detail. A difficulty with using ultrasonic sound in the surf zone is that both air bubbles and sand have the ability to scatter the sound energy, although with different characteristics. The objective of this thesis is to develop a discriminator to distinguish acoustic energy backscattered by entrained air bubbles from scattering by entrained sediments to measure sand and sediment fluxes at turbulent scales.



## **II. EXPERIMENTAL PLAN AND DEVELOPMENT**

In order to distinguish between acoustic backscatter from air bubbles and sediment, a method to measure the effects of bubbles on the Coherent Acoustic Sediment Flux Probe (CASP) backscatter level measurements was developed in a series of laboratory experiments. This required a means to produce a distribution of bubbles in a test volume, and a method to size and count the bubbles produced. The primary objective was to develop a method to discriminate bubbles from sediment, using dual frequency backscatter level and attenuation characteristics, and Optical Backscatterance Sensors (OBS) measurements.

### **A. EXPERIMENTAL OUTLINE**

#### **1. Development of Bubble Production System**

A bubble production system was required which was both simple to implement and capable of producing bubble clouds with size spectra similar to those in the ocean and of controllable densities. The production system had to produce a distribution of bubbles in the test vessel whose total density could be easily controlled while having a size spectrum representative of ocean / surf zone conditions. Implementation was constrained by the physical size of the test vessel, a plexiglass tube 19 centimeters in diameter. A stirring mechanism was used to create a homogeneous population of bubbles, and a conductivity cell directly measured void fraction within the test volume. The specific range of sizes required is discussed in a later section.

#### **2. Selection of a Bubble Measurement System**

As with the production system, a method of estimating the bubble size spectrum was required to be simple to implement, and to have a wide size measurement range and not perturb the bubble field. To allow robust size spectra to be estimated, an automated method of sizing was desired. Manual and visual methods of sizing and counting bubbles within the population were deemed to be too cumbersome for easy implementation.

### **3. System Testing in Fresh Water and Salt Water Filled Tanks**

Controlled laboratory experiments were conducted in both fresh water and salt water. Initial tests were conducted in fresh, deionized water in an effort to reduce the influence of biologic impurities. This reduced the effectiveness of the conductivity cell, but provided a good baseline comparison with later tests using salt water. Sea water was not used, as control of biological contaminants was again a major concern. These tests were broken down into four major subcategories:

- a. Clear, bubble-free tank.
- b. Bubbles only.
- c. Sediment only.
- d. Bubble and sediment mix.

## **B. EXPERIMENTAL SET UP AND DEVELOPMENT**

A literature search revealed many methods to both produce and measure air bubbles in a laboratory test tank. It was hoped that a proven method for both production and measurement could be utilized, to reduce the amount of time involved with the development of a laboratory experiment and apparatus, and minimize the need for validation of either the production method or the chosen means of determining bubble population characteristics.

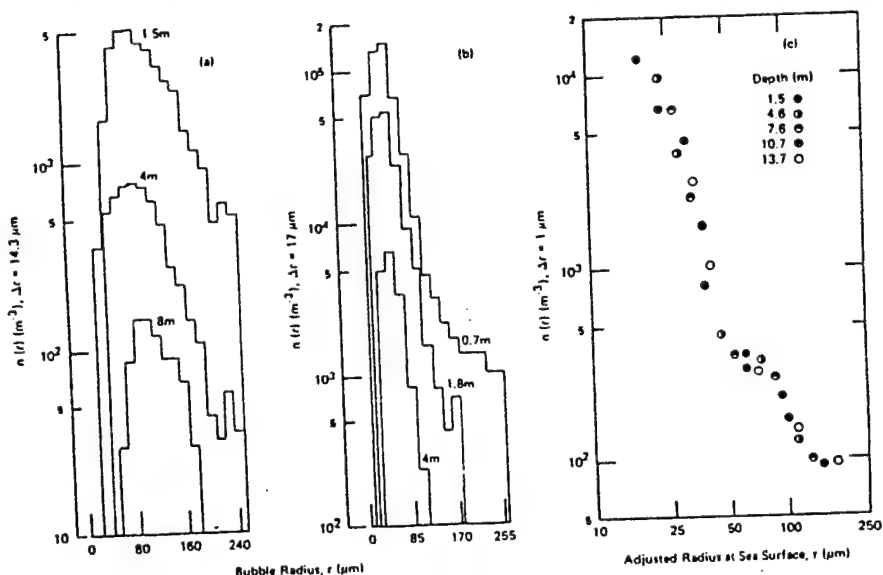
### **1. Ocean Bubble Spectra Measurements**

The primary criteria for selecting a bubble production system was that it simulate bubbles produced in the ocean during the spilling and breaking of waves, either in open ocean or in the surf zone. Several studies of the phenomenon of bubble production during the breaking of ocean waves have been performed. Published reports of field measurements of bubble populations in seawater have found a fairly consistent form for the entrained bubble spectra. Wu [1981] published a comprehensive summary of the results of several field measurements, most notably those of Medwin [1970], Kolovayev [1976] and Johnson and Cooke [1979]. Table (1) from Wu, shows a summary of field experimental conditions.

Investigator	Measurement Method	Minimum Bubble Radius, $\mu\text{m}$	Maximum Bubble Radius, $\mu\text{m}$
Medwin	Acoustic Scattering	18	176
Kolovayev	Bubble Trap	14	250
Johnson & Cooke	Photography	17	260

Table (1) Summary of Filed Experimental Conditions (after Wu [1981])

Wu compared not only of the results obtained by these three investigators, but also of the limitations of each of the selected measurement systems. In order to obtain a meaningful comparison, Wu limited his study to size ranges common to all three data sets, 17 - 176  $\mu\text{m}$ . The lower limit of this range was set by the results of Medwin and Johnson and Cooke, while the upper limit of this range, 176  $\mu\text{m}$ , was imposed by Medwin's measurement techniques. Wu normalized the spectra measured by the three investigators to obtain a probability density function (pdf) of bubble radii. Figure (1a) shows the pdf of Kolovayev's results with a distinct peak near 80  $\mu\text{m}$ . Figure (1b) shows Johnson and Cooke's results with a peak in the spectrum near 50  $\mu\text{m}$ . Figure (1c) shows Medwin's results with no distinct peak between approximately 15 - 200  $\mu\text{m}$ . The various plots



Figures (1a), (1b) and 1(c). Distribution of Measured Ocean Spectra (from Wu [1981])

shown depict spectra measured at different sample depths. These figures clearly show the depth dependence of the number of bubbles present. In open ocean conditions, the entrainment level is shallow, although highly dependent upon wind speed and turbulent mixing. Deeper sampling levels result in fewer bubbles sampled, as shown in Figures (1a) and (1b). Kolovayev measured bubble spectra at 1.5, 4 and 8 meters depth. Johnson and Cooke measured spectra at 0.7, 1.8 and 4 meters. Medwin conducted measurements at 1.5, 4.6, 7.6, 10.7, and 13.7 meters. Direct comparison of the pdf of Kolovayev's results with those of Johnson and Cooke, at 4.0 meters, shows that the peak of the distribution of the bubble radii for both investigators is near 80  $\mu\text{m}$ . Figures (2a) and (2b) show plots of bubble spectra at various depths and under different wind conditions as obtained by Kolovayev and Johnson and Cooke respectively. Figure (2c) shows Wu's plot of combined results without dependence on depth or wind velocity.

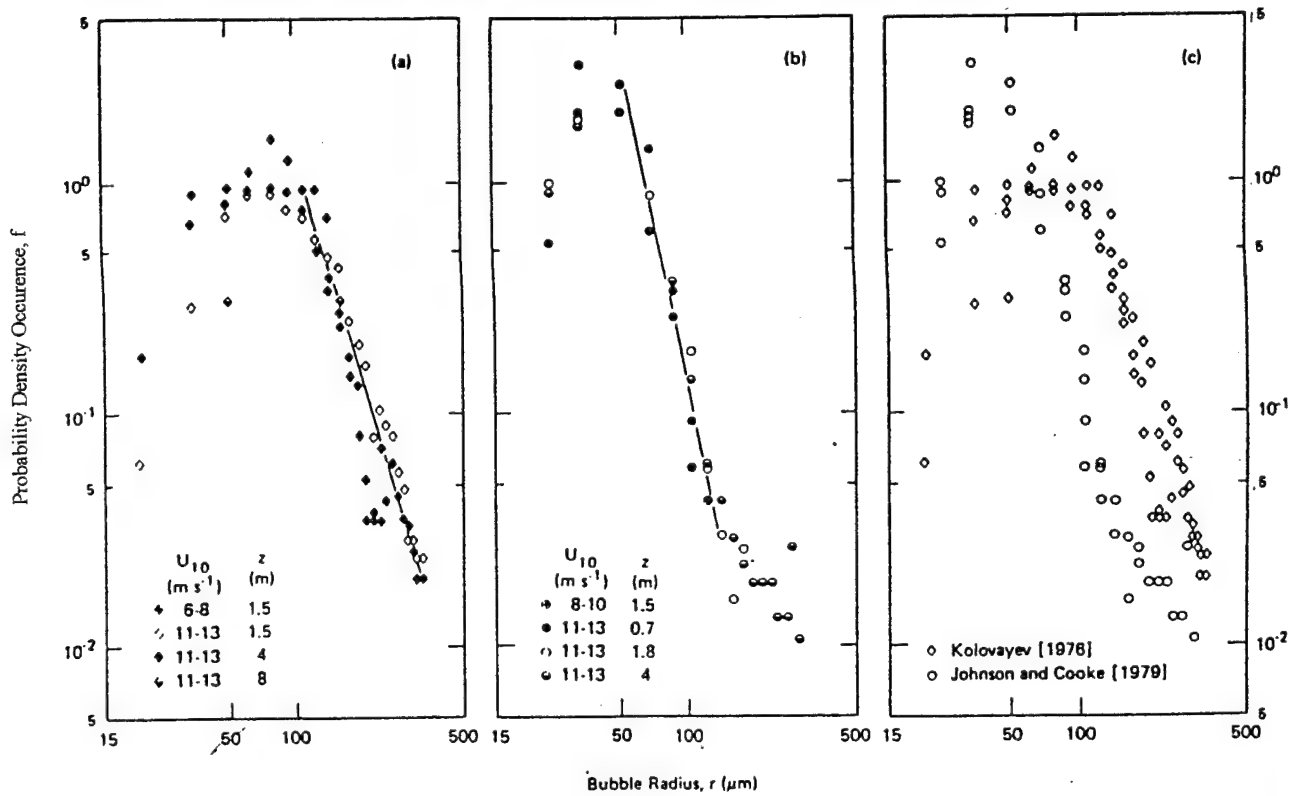


Figure (2). Ocean Bubble Spectra at Various Depths (from Wu [1981])

Closer examination of Figure (1c) shows that Medwin's data does, in fact, have a plateau near 80  $\mu\text{m}$  radius. While this does not represent a peak in his distribution, it does correlate with peaks shown in the data shown in Figure (2). The difference in magnitude

of the three plots can be attributed to errors associated with the sampling volume of the methods used to measure the bubbles and the smallest bubble resolved size. Medwin's method, using resonant acoustic scattering, has a much larger potential sample volume than the other methods.

Su, et al, [1988] measured microbubbles in the North Sea optically, using dark field specular reflection, in a manner similar to the Light Scattering Bubble Counter technique, Su et al [1994]. At a depth of 2 meters, they found microbubbles to fall within a range of 20-400  $\mu\text{m}$ . Figure (3) shows a comparison of results reported by Su et al [1988] with results reported by Johnson and Cooke [1979]. Although the measured concentrations do not compare too well below 50  $\mu\text{m}$  radius, the spectrum shape and concentration levels compare well at large bubble sizes.

Using an Acoustic Resonator Array, Medwin and Breitz [1989] and Breitz and Medwin [1989] reported results which were consistent with those of Su, et al [1988]. Figure (4) illustrates the close comparison between the results of Medwin and Breitz and Johnson and Cooke [1979]. Medwin and Breitz [1989] found bubble populations under spilling breakers at sea to have diameter of 25 - 270  $\mu\text{m}$ , but very significantly, no spectral roll off at small sizes.

These field measurements all show distributions within the range of approximately 20 - 400  $\mu\text{m}$  despite the use of a variety of different measurement techniques, but with small radius cutoffs often influenced by the measurement technique. Details of the operation of the photographic and acoustic techniques, as well as others, will be discussed in detail later.

Prior results of bubble generation in freshwater and seawater filled test tanks were researched to determine the diameter range which was attainable in the laboratory. Additionally, this would provide some insight into the effects of freshwater and seawater on bubble production, size and residence time. Glotov, et al [1962] determined a lower bound of bubble diameters to be 50  $\mu\text{m}$  in a freshwater tank with mechanically generated wind waves. Bubble sizes were determined using a bubble trap, similar to that used by

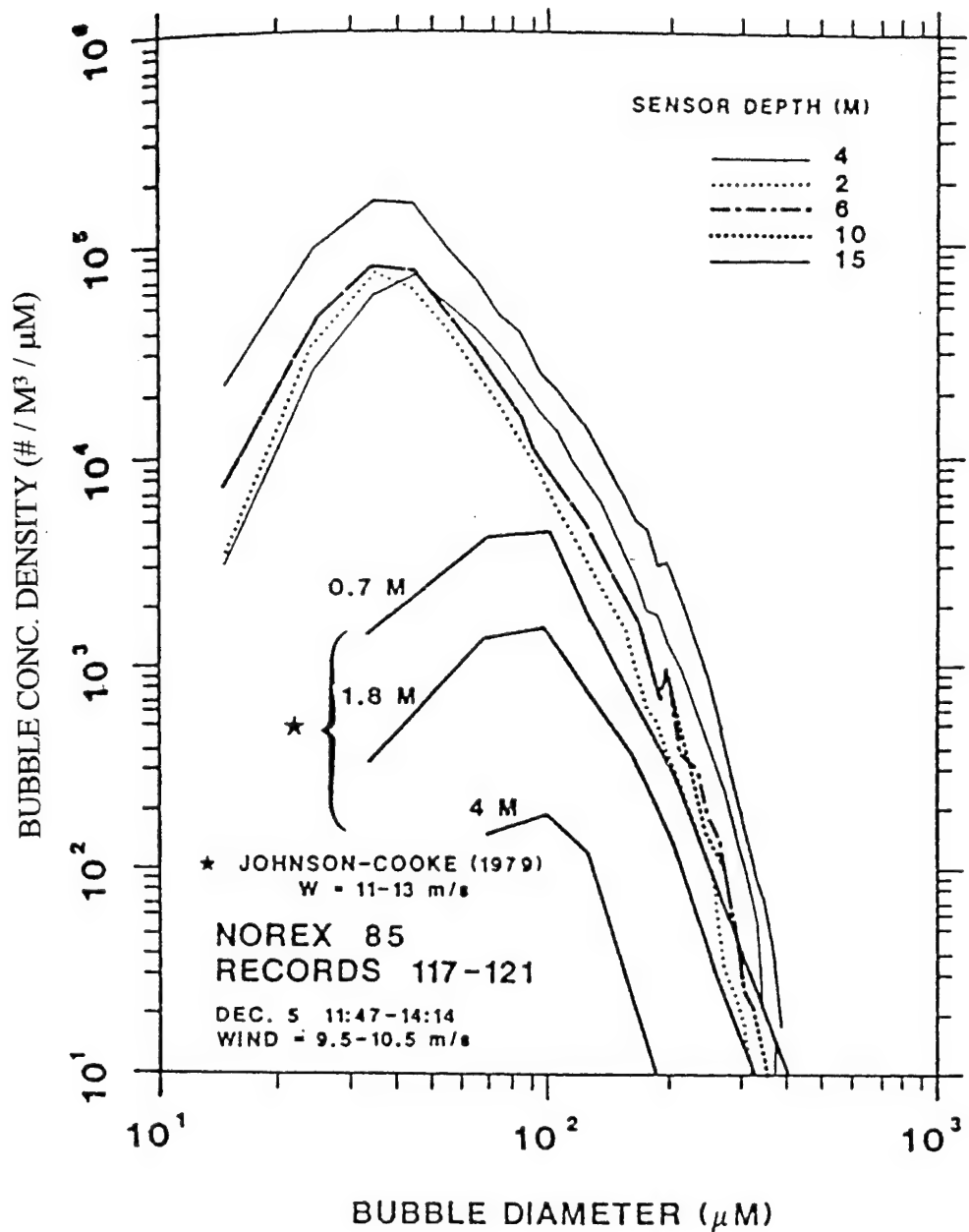
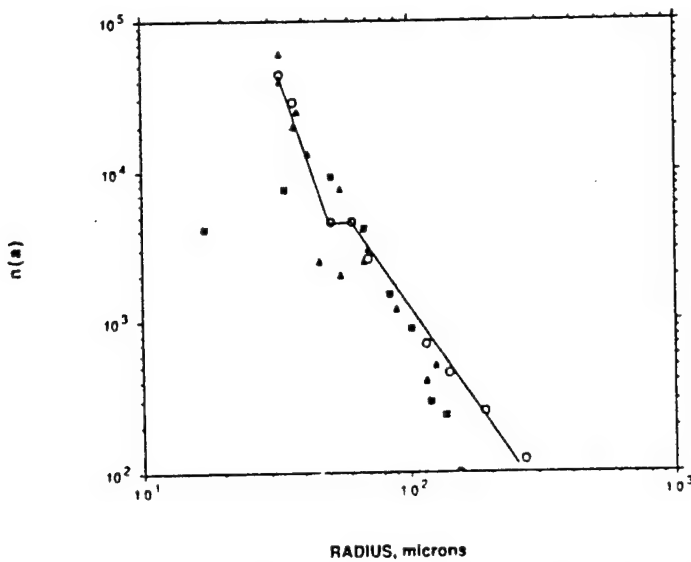


Figure (3). Bubble Concentration Comparison (from Su, et al [1988])



Figure(4). Comparison of Bubble Spectra Under Breaking Waves  
(from Medwin and Brietz [1989]).

Kolovayev [1976]. In laboratory observations of spilling breakers in a controlled test tank, Medwin and Daniel [1990] measured bubbles between 50  $\mu\text{m}$  and 7400  $\mu\text{m}$  acoustically. Cartmill and Su [1993], also using an acoustic resonator measured bubble size distributions in a test tank, ranging in size from 34 - 1200  $\mu\text{m}$ , under both freshwater and saltwater waves.

Cartmill and Su [1993] found that bubble plumes generated in freshwater and saltwater were qualitatively different. Figure (5) shows that although the shape of the distribution curve is similar, bubble production in saltwater yields an order of magnitude more bubbles at a given radius. Saltwater bubbles were far more numerous at a given radius than those measured in freshwater. They found that this was primarily due to the easy coalescence of freshwater bubbles "whereas saltwater bubbles repel each other as a result of their surface physical-chemical properties". Scott [1975] found that bubbles in saltwater have a longer residence time due, in part, to "the mild surface activity of the salt itself. The result of the surface activity is to retard the coalescence of very small bubble produced by breaking waves, decreasing the velocity of rise of the entrapped air and increasing the time during which bubbles are observed to reach the surface and break." Haines and Johnson [1995] found that bubbles produced in saltwater were more numerous, smaller, and resident longer than in freshwater. It was therefore expected that, for a given bubble production rate, the bubble population in a saltwater filled tank

would have a higher concentration at small diameters and a lower concentration at larger diameters.

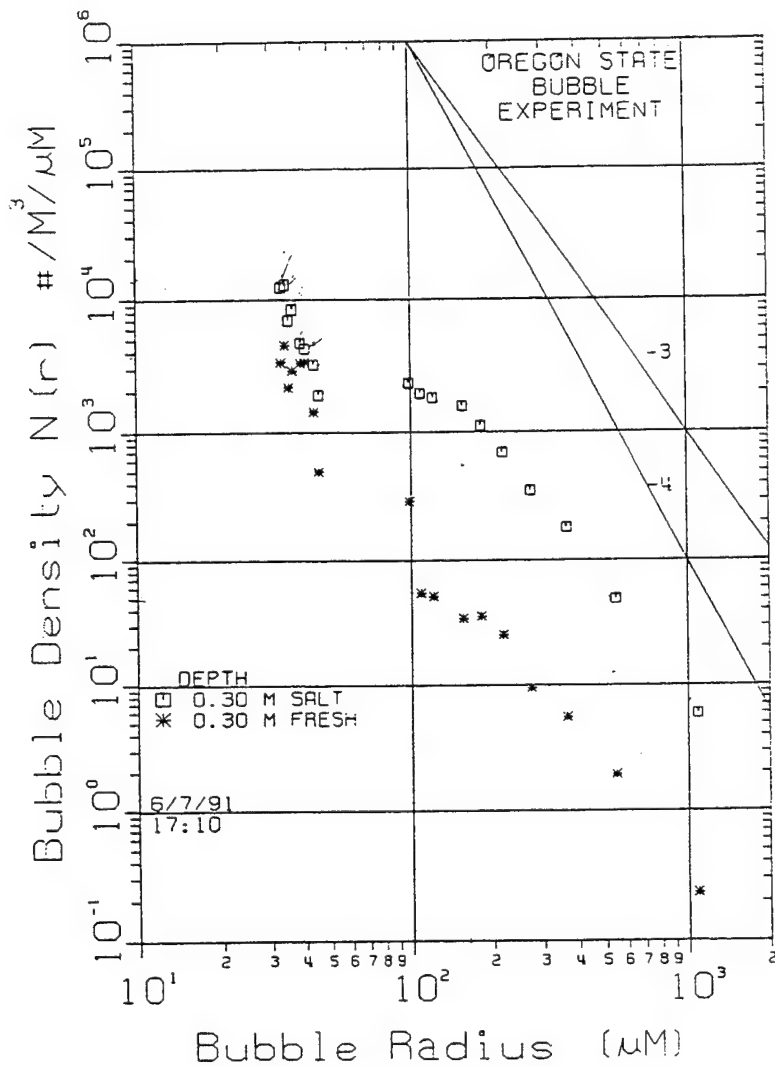


Figure (5). Bubble Size Distribution Comparison, Fresh and Saltwater  
(from Cartmill and Su [1993])

Based on these previously observed bubble size spectra, a size range of 20 - 400  $\mu\text{m}$  was determined to be a representative and desirable range for the bubble production system to be constructed. This size range would closely match the range of diameters

found in field measurements at sea as well as those measured in laboratory experiments in wind wave tanks.

## 2. Ocean Spectra Theory

Bubbles are formed in the ocean primarily due to downward forces generated by breaking wind waves, or by shoaling and breaking waves in the nearshore. Ocean waves break for two reasons: kinematic and dynamic instability. Kinematic instability results when the velocity of individual particles of water within the wave becomes larger than the phase velocity,  $C_{ph}$ , of the wave itself. Dynamic instability results when the acceleration of individual particles becomes greater than the downward force of gravity. In each case the particles separate from the leading edge of the wave and fall. The force of the particles falling as a group onto the leading slope of a wave, as shown in Figures (6a) and (6b), can entrain air bubbles below the surface of the ocean. These entrained bubble clouds remain beneath the surface after the wave travels along and are left to evolve. Koga [1982] stated that "the main mechanism of bubble formation in [wind] waves is intermittent bubble entrainment by an ordered convergent flow on the leading slope near the crest. Koga described this entrainment region as the area in which particles from the breaking portion of the wave impinge upon the leading slope of the wave. Provided that the downward force of these particles is sufficient to overcome the surface tension of the leading edge, bubbles will be entrained under the wave. With this conceptual model, the higher the wave, the greater the force, and the deeper the entrainment. If the area behind the wave entrainment zone is relatively quiescent, as in open ocean conditions, the bubble cloud will disperse relatively quickly as large bubble rise to the surface. If the area behind the breaking wave is highly turbulent, such as in the surf zone, the entrained cloud may be mixed through the water column several times before rising to the surface. This increased residence time can be expected to increase the size spectral levels of small bubbles.

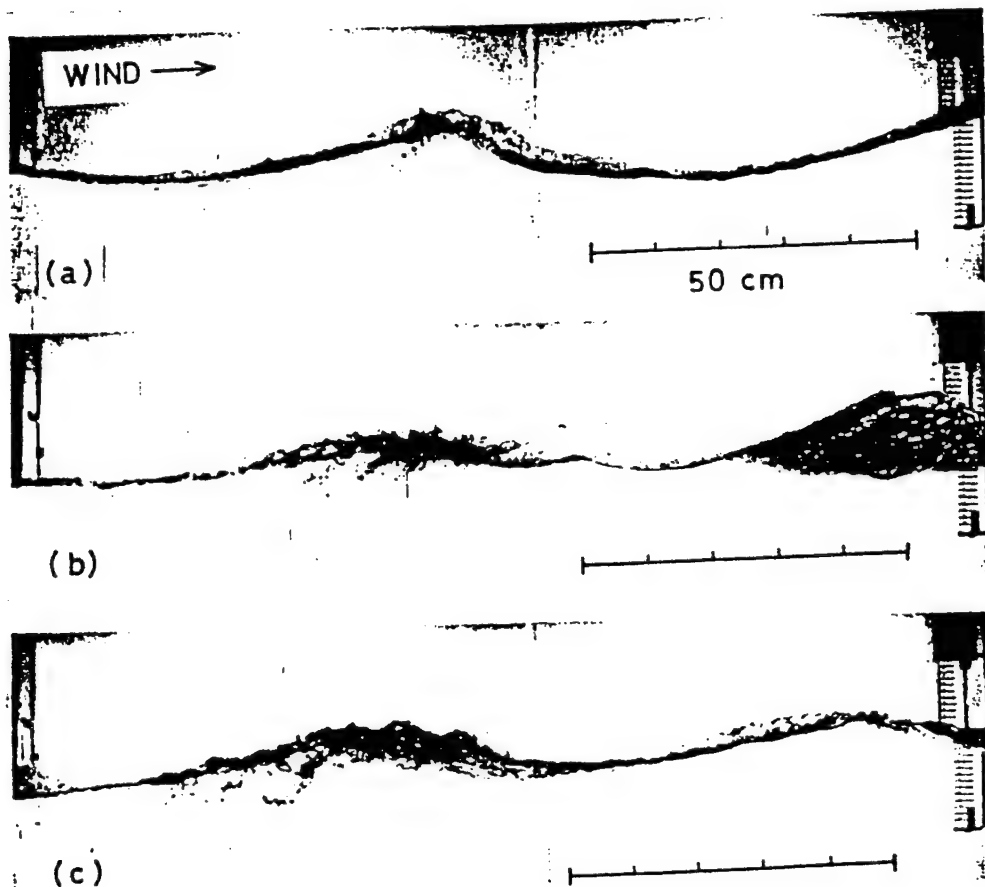


Figure (6a). Breaking Wind Wave Bubble Entrainment Pattern  
 (from Koga [1982])

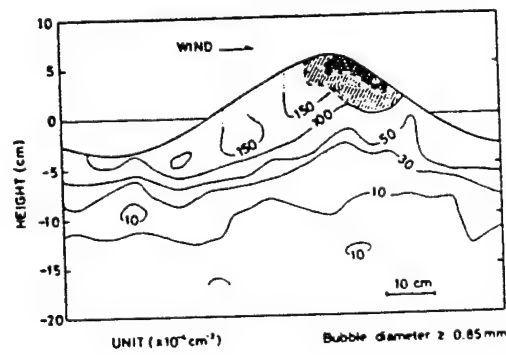


Figure (6b). Mean Distribution of Bubbles along a Representative Wave  
 (from Koga [1982])

### **3. Laboratory Bubble Production Methods**

Many methods of bubble production in a test volume were researched in the literature. Previous experimenters have produced streams using hypodermic needles fed by nitrogen tanks and electrolysis. Bowyer [1992] used measured volumes of water dropped from a height into the test volume. Bubble entrainment has also been accomplished through the use of surface and underwater jets.

#### ***a. Electrolysis and Hypodermic Needles***

Bubble production via electrolysis typically uses a bubble - producing wire wrapped around a rod which sweeps through an arc at the bottom of the tank. This provides a vertically homogenous bubble plume, but bubbles produced at the 'turning points' in the arc of the arm are larger than those formed during the arm's sweep. This method was rejected as not producing a bubble population with significant size range, so it was likely that the bubbles created would not represent a statistically significant simulation of the spectrum estimated to be entrained in the surf zone. Additionally, since electrolysis produces hydrogen ( $H_2$ ) and oxygen ( $O_2$ ) the bubbles will be highly soluble. The gas solubility effects the residence time of individual bubbles and can therefore effect the size distribution of the produced bubble population. Su, et al [1994] used a hypodermic system constructed of several needles mounted on a tube sweeping through an arc at the bottom of the test tank, very similar to the mechanism involved with the electrolysis method. Hypodermic needles do not produce the highly soluble bubbles, but tends to produce a narrow range of source bubble sizes, and was rejected for this reason.

#### ***b. Underwater Jet Air Entrainment***

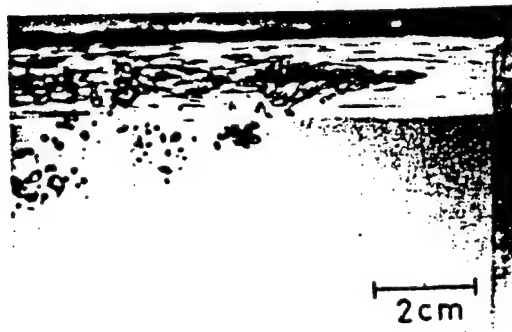
This method utilizes an under water nozzle acting as an eductor which sucks air into a water stream due to the velocity of the water within the nozzle. The entrained air is fed either from a compressed air supply or drawn from a gas reservoir. The size of produced bubbles varies from tens of microns to several millimeters. Authors found that this gave a more continuous bubble density over the range of 30 - 1200  $\mu m$ . This range of radii was attractive as it nearly met the criteria for matching *in*

*situ* measurements of bubble spectra under breaking waves [Breitz and Medwin, 1989]. Hypodermic, Electrolytic and Underwater Jet methods were briefly described by Su, et al (1994) and were used in their comparison of various bubble measurement systems.

### *c. Above Water Jet Air Entrainment*

Open ocean tests have found fairly consistent results showing bubble spectra between 20 - 400  $\mu\text{m}$  [Breitz and Medwin, 1989], as shown in Figure (4). A production method was required which would produce a continuous density, broad spectrum of bubbles which could be mixed to create an homogeneous bubble population. In order to do this, a bubble production method developed by Koga [1982] was chosen. This method involved an above water jet impinging upon the surface of the test tank. The jet entrains air bubbles due to the downward force acting upon the surface of the fluid in the test volume. Bubble entrainment is dependent upon overcoming the surface tension of the fluid. Koga [1982] found that this method, for his experimental parameters, created air bubbles ranging in size from 25 - 4500  $\mu\text{m}$  in diameter. This method is very similar to the under water jet entrainment method noted previously, but does not require an eduction nozzle. It also reduced the complexity and amount of tubing required in our experimental apparatus. Given the nature of set up and the lack of physical space within the test vessel to be used in the laboratory, this was an important consideration. However, production of a bubble cloud is highly dependent upon the angle of impingement of the jet upon the surface, as shown in Figure (7). The figure clearly shows that at shallow incidence angles, as in Figure (7a), the entrained bubble cloud contains many relatively large bubbles, and the entire cloud remains near the surface of the tank. At steep angles of incidence, such as in Figure (7d), very few bubbles are created. Koga found that at moderate angles, the entrained bubble cloud had a broad spectrum of bubble radii, and the produced cloud was allowed to evolve farther below the surface than with shallow angles, which improved mixing within the stirred test vessel. The critical impingement angle was a very real concern, however. Due to the small size of the test vessel, flexibility in selecting an impingement angle would be

constrained. This was overcome through the use of a fairly short rigid nozzle fed by flexible Tygon tubing. This provided the necessary flexibility to select an optimum impingement angle without restricting the use of other apparatus at the surface of the tank due to the size of the nozzle apparatus.



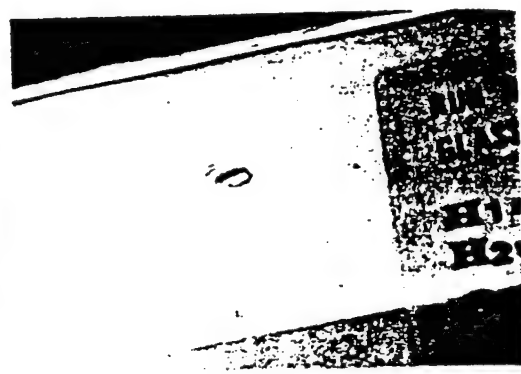
(a)  $\theta = 15^\circ$



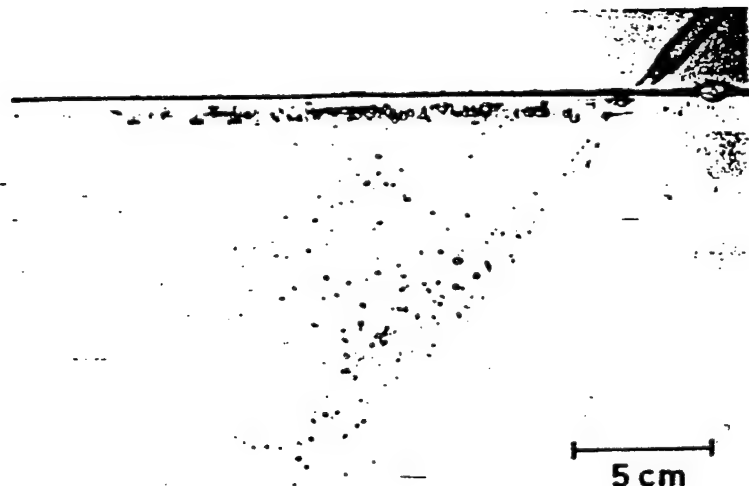
(b)  $\theta = 30^\circ$



(c)  $\theta = 45^\circ$



(d)  $\theta = 50^\circ$



(e)  
Complete view of  
the bubble  
distribution  
 $\theta = 45^\circ$

Figure (7). Bubble Entrainment for Various Nozzle Inclinations (from Koga [1982])

#### 4. Bubble Production System Development

Initial development and design of an above water jet for the production of air bubbles in the test volume closely followed the design used by Koga [1982]. A self priming water pump was initially used to circulate water from the test vessel, through a nozzle and back into the test vessel. Initial tests were conducted by visual inspection of the produced bubble cloud.

Visual testing of the water jet showed that this particular method was both easy to set up and easy to control. Varying the size of the nozzle appeared to alter the spectrum of the bubbles produced by varying the volume of the flow, while adjusting the flow velocity of the jet for a given nozzle diameter with a needle valve, altered the total density of the produced cloud without noticeable affect on the produced spectrum. Initial tests of this system, without direct measurement of the resulting bubble population, used three nozzle diameters as shown in Table (2).

Nozzle Diameter

.046 in (.117 cm)

.082 in (.208 cm)

.183 in (.465 cm)

Table (2). Entrainment Jet Nozzle Sizes for Initial Tests

During tests it was found that the produced spectrum was both dependent on nozzle diameter, and therefore flow velocity, as well as the angle of impingement. These results are consistent with those reported by Koga [1981]. He found that for an impingement angle,  $\theta$ , of 45 degrees, the distribution of the produced spectrum was broader than at  $\theta = 30$  degrees and  $\theta = 50$  degrees. Both of these angles produced a narrower distribution of sizes. In addition to a dependence on  $\theta$ , bubble production was also highly dependent on the height of the jet above the surface of the water. As reported

by Koga [1981], the greater the distance above the water, the more unstable the flow from the jet became and the more confused and unstable the produced bubble population became. It was found that to produce a stable, easily controlled bubble population, the nozzle could be positioned approximately 1 centimeter above the surface of the water. Above this height, the produced cloud contained a great many very small bubbles, but not a large range of bubble sizes. If positioned too near the surface, the nozzle had a tendency to become submerged due to surface agitation brought on by the laboratory stirring apparatus used to produce a homogeneous bubble cloud within the test vessel. The pump used in the initial tests was a March Manufacturing model MDX 115 volt, 1/55 horsepower pump.

Due to the low flow rate of the pump, it was necessary to reduce the interior diameter of the tubing to produce a flow velocity capable of overcoming the surface tension of the water in the test volume. The exit diameter of the pump was 0.5 inches (1.27 centimeters). This was decreased at the nozzle to the diameters shown in Table (2). It was found that the 0.183 inch diameter nozzle produced a low velocity jet which was only capable of producing a narrow spectrum of fairly small bubbles. The 0.082 inch diameter nozzle had a broader spectrum, but produced a very low density of bubbles. Since these initial tests were conducted with the velocity controlling needle valve fully open, it was essential to produce a high density, broad spectrum population in order to have a workable density population at lower flow rates. The final nozzle, 0.046 inches produced a broad spectrum with a high density population. Qualitative observations of the produced bubble clouds revealed that this method produced clouds which had controllable density with a relatively constant size spectrum. The critical requirement was to produce broad spectrum clouds which had controllable density but which maintained a constant spectral range, unaffected by flow velocity. A diagram of the production system and associated apparatus is shown in Figure (8).

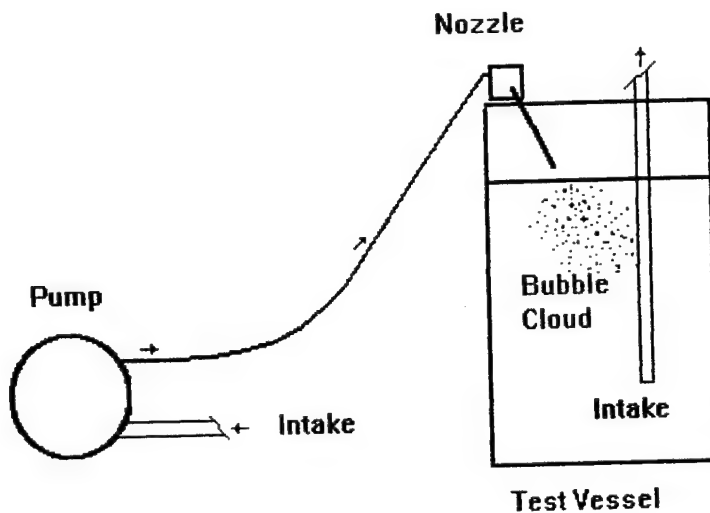


Figure (8). Above Water Jet Entrainment Apparatus

### 5. Bubble Size Spectra Measurement

Several criteria needed to be met in selecting a method of bubble size spectra measurement. The measurement method had to be capable of measuring bubbles without disturbing the bubble cloud. This would restrict the use of any method which physically trapped a single bubble, or disrupted the natural evolution and rise of any individual bubble within the population. The sizes of the measured bubbles should not be restricted by the physical limitations of the selected equipment. Perhaps most important among the considerations were those of cost and ease of implementation. The system had to be relatively inexpensive and simple to operate and install. Several methods of bubble measurement were investigated in a literature search, including: Light Scattering Bubble Counters (LSBC), Photographic Bubble Imaging System (PBIS), Acoustic Resonator Arrays (ARA), and Laser Holography and Coulter Counters. LSBC, PBIS and ARA systems were compared for use in sizing bubbles by Su, et al (1994). The goal was to select a measurement method which was robust, easily implemented, had a large sampling volume, had the ability to measure bubbles of 20 - 500  $\mu\text{m}$  radius accurately, quick response time and could sample the bubble cloud accurately using automatic data analysis. Additionally, the method would preferably have the ability to be

deployed in the field to obtain *in situ* measurements. A review of methods described in the literature follows.

#### *a. Light Scattering Bubble Counter*

The Light Scattering Bubble Counter system uses dark field specular reflection for detection of microbubbles. White light is reflected by the air - gas interface of the bubble with the surrounding water. Typically, bubbles are drawn into a sampling volume by a pump, and reflected light intensity is detected by a photomultiplier at a predetermined scattering angle with respect to the incident light. Figure (9) shows a diagram of the apparatus used by Su, et al [1988]. With this particular set-up, Su, et al [1988] chose a scattering angle of 125 degrees in order to detect a strong forward scattering portion of the light energy scattered by particles within the sample volume.

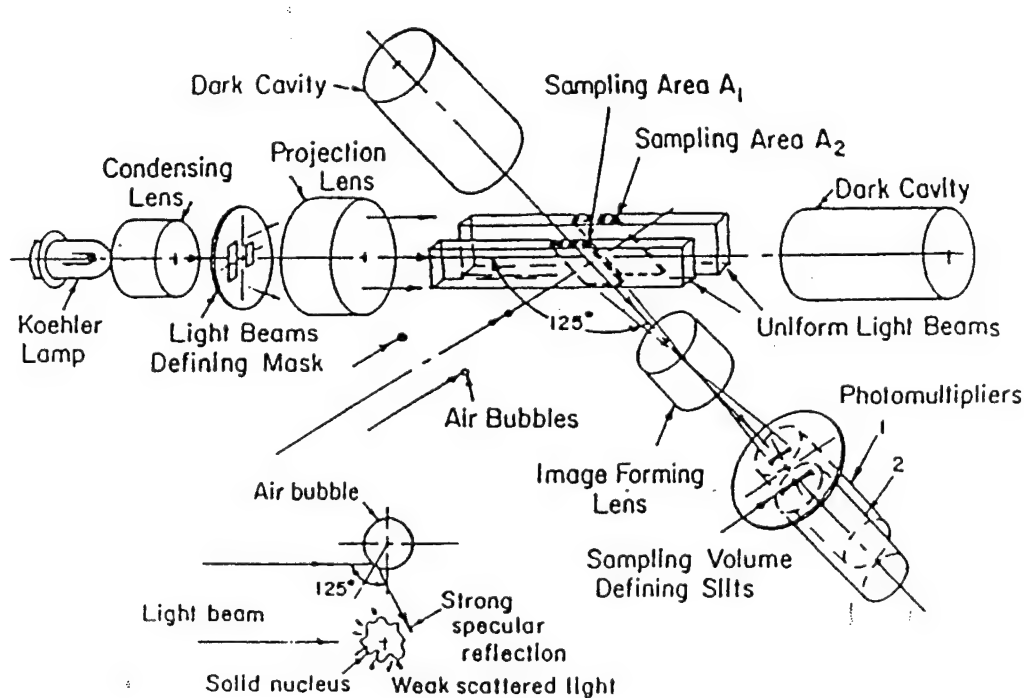


Figure (9). Light Scattering Bubble Counter (from Su, et al [1988])

The intensity of the reflected light, as detected by the photomultiplier, is proportional to the square of the bubble's radius. Su, et al [1994] calibrated his system by determining the size of the individual test bubbles from their terminal rise velocity. This system, as reviewed by Su, et al [1994], was limited by its inability to sample bubbles of greater than 200  $\mu\text{m}$  radius due to the physical size of the intake of the sampling volume. This limitation could easily be alleviated by changing the size of the sample volume entry. This system was rejected for a variety of reasons. The limited size range of the bubbles measured, 10 - 150  $\mu\text{m}$ , and the small sampling volume were problematic, but its inability to sample more than a single bubble simultaneously was seen as severely limiting in its application to the high bubble densities to be generated in the laboratory tank measurements. There was also a concern that the method of pump sampling bubbles into the sampling volume might distort not only individual bubbles, but the overall spectrum by breaking up large bubbles in order to receive them in the sampling volume. Ling and Pao [1988] used a similar apparatus to measure micro bubbles in the North Sea. With a selected scattering angle of 125 degrees, they detected a pattern of specularly reflected light on the surface of air bubbles which they called "hot spots". They determined that the size of this reflected light spot was directly dependent upon the size of the bubble and was related to the selected scattering angle. Figure (10) shows the geometric optical scattering pattern as seen by the photomultipliers mounted on Ling and Pao's equipment.

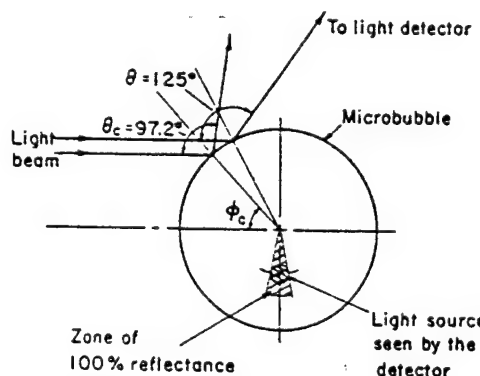


Figure (10). Specular Reflection off the Surface of an Air Bubble in Water  
(from Ling and Pao [1988])

### ***b. Photographic Bubble Imaging System***

Su, et al [1994] used a Photographic Imaging System in a comparison of several measurement techniques. This system uses photographic images of bubbles illuminated by a combination of three strobes, separated by 120 degrees. This provides three bright points around the circumference of each individual bubble. Figures (11) and (12) show the orientation of the camera and strobes and the pattern of strobe reflections upon the bubble's surface respectively. In each image of a bubble, the three dots occur due to specular reflection of the photographic strobes. The sample volume was determined by the width and length of the image, and the depth of field of the lens.

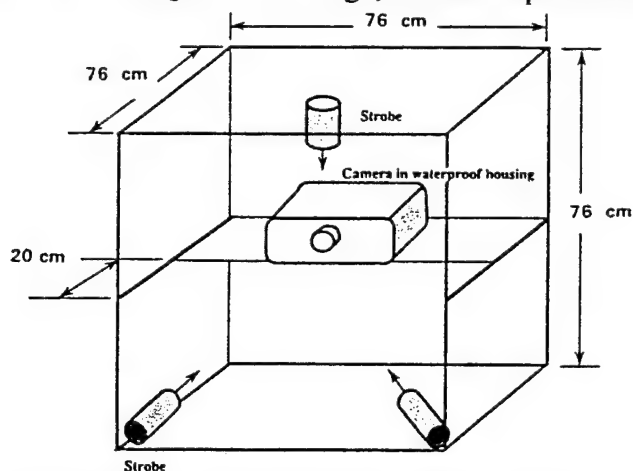


Figure (11). Photographic Bubble Imaging System (from Su, et al [1994])

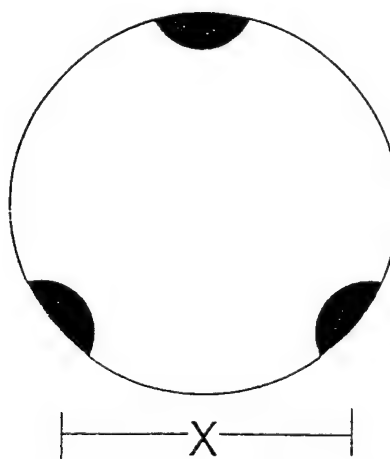


Figure (12). Strobe Pattern on a Bubble's Surface (from Su, et al [1994])

Manual counting and measuring of bubbles is performed with a microscope. Although this system is capable of sizing bubbles of up to 500  $\mu\text{m}$ , a lower bound of 50  $\mu\text{m}$  is imposed by the finite resolution of the microscope, the sensitivity of the photographic system and the graininess of the film used in the photographic process. The upper bound is due to the low statistical probability of encountering a bubble larger than 500  $\mu\text{m}$  within a sampling volume, and the limited number of samples due to the laborious visual analysis of the photographs. This spectral range was limited, as expected, as much smaller radii ( $\sim 10 \mu\text{m}$ ) bubbles would be encountered both during laboratory experiments and during *in situ* measurements. However, the lower bound could have been improved by using a more powerful microscope. Results obtained by Su, et al [1994], using this system in the laboratory, correlate with the *in situ* findings of Walsh and Mulhearn (1987). This system does not seem to disturb the flow of the bubbles, but Su, et al found it only practical for calibrating other systems in the lab due to the extremely labor intensive manual microscopic measurements of the photographic negatives.

### *c. Acoustic Resonator Array*

The Acoustic Resonator Array provides a continuous distribution of bubble sizes without tedious manual counting and microscopic measurements. The system developed by Breitz and Medwin [1989] consisted of a transducer and reflector plate separated by 20 cm. When a broadband acoustic source excites the volume between the plates, standing waves arise due to a series of harmonic resonances governed by the relationship:

$$f_n = n c / 2 L$$

Equation (1)

where  $c$  = speed of sound,  $n$  = number of the acoustic harmonic and  $L$  = distance between the plates. This results in a cavity fundamental frequency of approximately 3

kHz, dependent upon the speed of sound in the water, with multiple harmonics over the bandwidth of the white noise transmitted into the cavity. This yields 1 fundamental and 32 harmonics over a 100 kHz band. Resonant bubble frequency is given by:

$$f_o = (1/a) \sqrt{(3\gamma P_o / \rho_o)}$$

Equation (2)

where  $a$  = bubble radius,  $\gamma$  = ratio of heat capacities,  $P_o$  = hydrostatic pressure and  $\rho_o$  = the density of the water. Over the 100 kHz white noise range, this relationship covers bubble diameters from 1200  $\mu\text{m}$  down to 34  $\mu\text{m}$ , corresponding to resonant frequencies between 3 and 99 kHz. Higher frequencies could be used, but the extinction cross section,  $\sigma_e$  is no longer due simply to the resonance of the individual bubbles but to the increasing viscous effects in smaller bubbles. The separation between the plates could also be altered to expand the range, but then the resonance quality factor,  $q$ , is lowered. The bubble size distribution is given by the formula

$$\eta_o(a) = (2\pi \Delta f) / (c \sigma 10^6 \delta a)$$

Equation (3)

where  $\eta_o$  = bubble density,  $c$  = speed of sound, and  $\Delta f$  = the change in resonance width calculated from the sound frequency spectrum comparison with bubbles present and absent. A similar system, as described by Su, et al [1994], is capable of sampling bubble radii of 34 - 1200  $\mu\text{m}$ . It also samples the bubble cloud with a volume of 1250 cc, a much larger sampling volume than any of the other systems investigated. Both of these factors, coupled with the ease of use both in the field and the laboratory made this highly attractive. Unfortunately, the equipment necessary to employ this method was unavailable for the laboratory portion of the experiments, and the small test vessel precluded using borrowed existing field systems.

#### *d. Laser Holography*

O'Hern, et al [1988], used a pulsed ruby laser directed through a sampling volume to obtain holographic images of scatterers within the volume. A portion of the beam is diffracted by particles, while the remainder passes through the volume. High resolution film records the interference pattern of the diffracted and undiffracted laser light, and the image is subsequently analyzed to size particles illuminated within the sampling volume. The developed hologram is illuminated with a He-Ne laser beam. This image provides a three dimensional representation of the illuminated bubble cloud. Particles are discriminated from bubbles by visual observation. Bubbles are brighter, more rounded and have a central dark spot due to internal focusing of the laser light. This central dark spot is due to the fact that O'Hern viewed the illuminated bubbles along the axis of the beam. Due to the design of our laboratory tank, and the many complexities of laser holography, this method proved to be impractical. O'Hern's laser holography system has extremely good object resolution, approximately 5  $\mu\text{m}$ . Again, the analysis of produced images would be very tedious as objects within the sample volume would be sized by visual measurement only, rather than an electronic, or automated means. During ocean tests of this system, O'Hern, et al, found holographic techniques to be a reliable method of bubble measurement, but surprisingly no bubbles larger than 50 microns were detected.

#### *e. Coulter Counters*

Coulter Counter systems detect changes in conductivity as particles, or bubbles, in a fluid pass through a detection volume. The amplitude of the signal is nearly proportional to the volume of the particle, as long as the particle dimensions are less than 40% of the orifice diameter. O'Hern, et al [1988] used a Coulter Counter apparatus with an orifice diameter of 140  $\mu\text{m}$ , limiting the maximum diameter of measured bubbles to approximately 50  $\mu\text{m}$ . It is, of course possible to use a larger orifice diameter to enable larger bubbles to enter the counter. A Multi-Channel Analyzer sized incoming signals and sorted them into 128 separate channels. It was noted by O'Hern that Coulter

Counters may suffer an order of magnitude error in estimation in particulate content. This is possibly due to the disintegration of the particles as fluid is drawn into the measurement volume, therefore, the measured spectra of bubbles would not necessarily be accurately represented. Large bubbles could easily be broken up as they passed through the orifice to be counted, making it an unattractive option.

## **6. Measurement Apparatus**

Following this literature review and careful consideration, a bubble measurement system was decided upon which consisted of a hybrid of several of the previously noted systems. The measurement system consisted of a high intensity laser beam which was to be used to illuminate individual bubbles within the bubble cloud, a microscope and video camera assembly, and framegrabbing software. This system utilized the bubble illumination theories of the Light Scattering Bubble Counter (LSBC) system. By capturing a video image, Photographic Bubble Imaging System (PBIS) fundamentals are exploited, but analysis was enhanced through the use of automated image processing software. The narrow beam, high intensity of a laser was utilized without the cumbersome nature of holographic imagery and the complexity of holographic apparatus. The bubble population would not be disturbed and would evolve without physical constraints as noted in research of bubble traps, Light Scattering Bubble Counters and Coulter Counters. Lasers have been used in many instances to measure bubbles and other suspended objects in laboratory and field experiments as previously noted. In most cases, however, lasers have been used to measure single objects rather than large groups or clouds of objects.

Initially, a beam spreader was mounted on the head of the laser to create a fan of light spread over 30 degrees, with a depth of 0.3 mm. This fan of light was to be reflected by a mirror apparatus as shown in Figure (13). It was thought that this geometry would provide bubble images similar to those obtained using a Photographic Bubble Imaging System and as shown in Figure (12). Only bubbles within the fan of light would be illuminated, but none outside of it. This provided a well defined sample

light would be illuminated, but none outside of it. This provided a well defined sample volume and high illumination intensity for the video camera and microscope. The laser was aimed down through the surface of the test vessel with the camera positioned to view the illuminated cloud normal to the plane of illumination. However, it was found that the surface disturbance created by the stirring action within the test vessel coupled with the reduced light intensity caused by the beam spreader made this set up ineffective. Additionally, within the turbulent, high density bubble cloud within the test vessel, there were many instances where each bubble did not have three distinct specular "hot spots" in the captured image. This was primarily due to the interference of other bubbles blocking the light rays from striking the surface of another bubble. Therefore, bubbles recorded by the video camera had between one and three "hot spots". The random nature of the representation of a bubble by "hot spots" resulted in this optical geometry being rejected. Instead, a single beam of light was projected into the side of the tank without the attachment of either a beam spreader or the mirrors. This prevented the surface interference, light intensity and random "hot spot" problems without eliminating the ability to attain a 90 degree scattering angle within the test vessel.

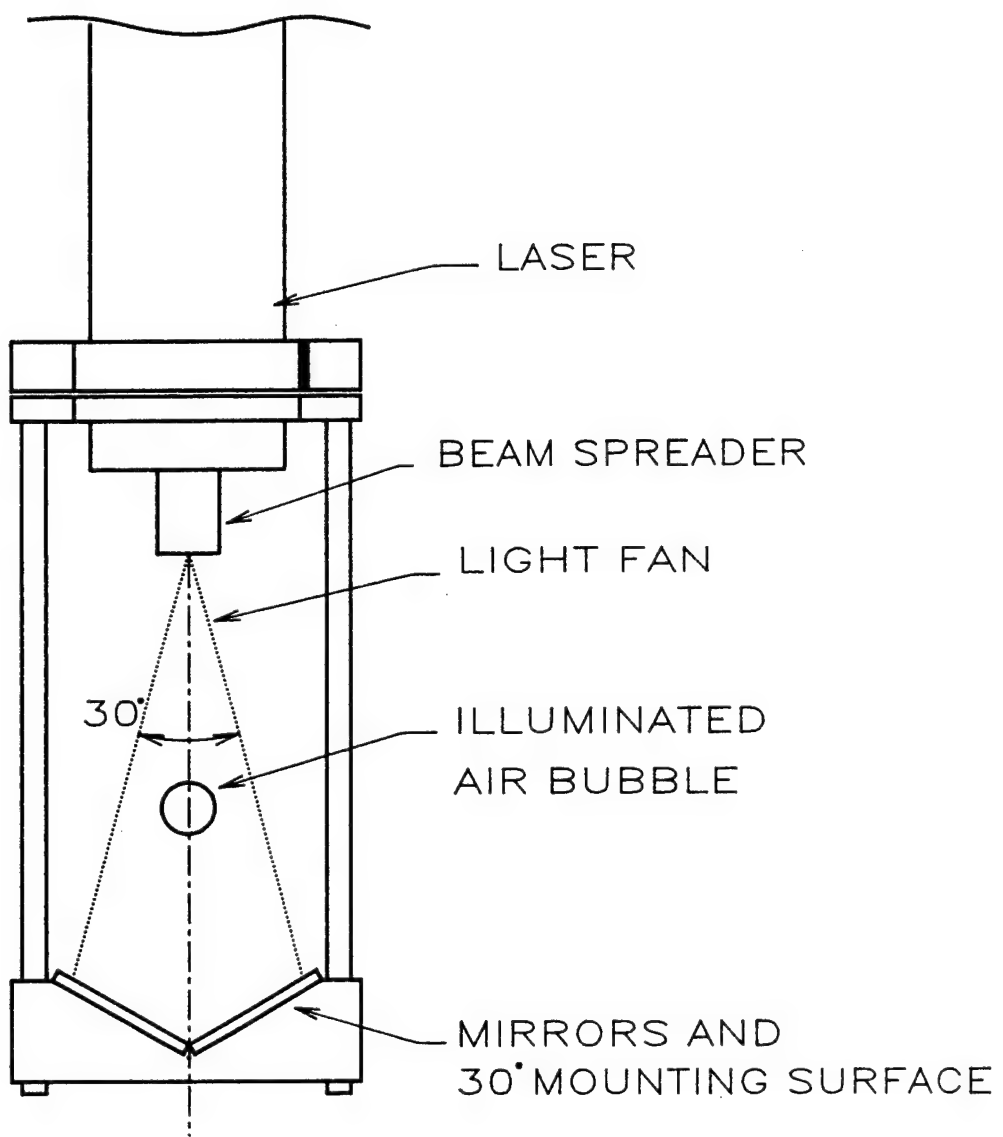


Figure (13). Laser and Mirror Assembly

## 7. Optics Theory

A simple model of the reflection of an incident plane of light on an air bubble suspended in a volume of water on a ray of incident light was developed to understand the imaged reflection measured by the laser / microscope system described in section 6. When a light ray strikes the surface of a spherical, clear, or transparent object, some of the energy is reflected at an angle equivalent to the incident angle,  $\tau$ . In this case,  $\tau = 90$  denotes central incidence and  $\tau = 0$  denotes grazing incidence. Figure (14), from Van de Hulst [1957], illustrates the effect of a single ray of light incident upon the surface of an

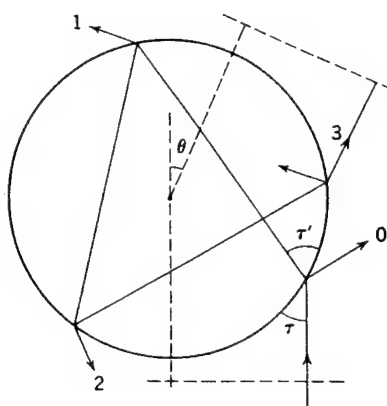


Figure (14). Single Light Ray Trace for an Air Bubble in Water  
(from Van de Hulst [1957])

air bubble in water. On a sphere, where the slope of the surface becomes increasingly steep as one travels outward from the center, this means that parallel light rays striking the surface are scattered over a wide range, as shown in Figure (15). This figure shows a two dimensional slice of an air bubble in water. The incident light rays have been generated by a distant source, and all rays are assumed to be parallel. Most of the incident energy is reflected, as shown in Table (4). The remainder of the light energy is transmitted into the bubble and refracted prior to striking the interior surface. A portion of this energy is, in turn, internally reflected, and a portion is transmitted out of the

bubble, refracted again by the surrounding fluid. The energy departs the bubbles surface at an angle equal to the incident angle,  $\tau$ . Energy refracted in the interior of the

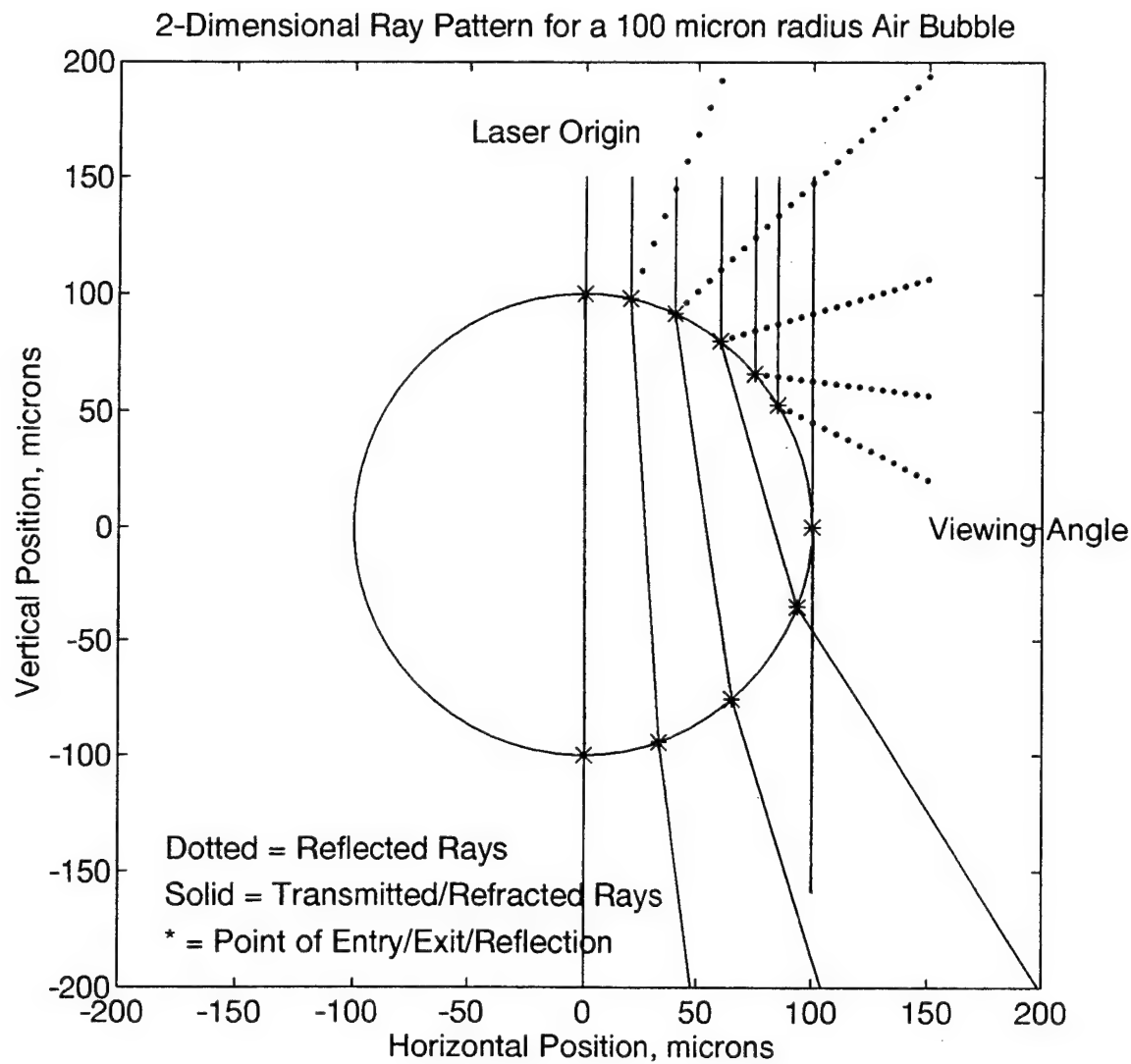


Figure (15). Multiple Light Ray Trace for an Air Bubble in Water

bubble follows Snell's Law:

$$\cos \tau' / n_2 = \cos \tau / n_1$$

Equation (4)

where  $\tau'$  is the internal refraction angle,  $n_1$  and  $n_2$  are the indices of refraction of water and air respectively. Van de Hulst gives this relationship as:

$$\cos \tau' = (1/m) \cos \tau$$

Equation (5)

where  $m$  is the ratio of the indices of refraction,  $m = n_2 / n_1$ . For an air bubble in water, Van de Hulst gives the index ratio,  $m$ , the value 0.75. Halliday, et al (1993), give the index of refraction for air and water as follows:

Medium	Index of Refraction, n
Air (STP)	1.00029
Water (20 degrees C)	1.33

Table (3). Indexes of Refraction for Light in Air and Fresh Water  
(after Halliday, et al [1993])

These values result in a value of  $m$  equal to 0.752. This physical relationship for internal refraction holds until the angle of incidence becomes equal to or greater than the critical angle for the given index of refraction. The critical angle,  $\theta_{\text{crit}}$ , as defined by Halliday, et al [1993], is the angle of incidence above which total internal reflection occurs, i.e. for angles of incidence greater than  $\theta_{\text{crit}}$ , rays will experience no refraction, only reflection.

Critical angle is given by the relationship

$$\theta_{\text{crit}} = \arcsin(n_2 / n_1) = \arcsin(m)$$

Equation (6)

For a bubble of given radius,  $r$ , assumed to be a perfect sphere, the angle of incidence for a beam of parallel light rays is dependent on the slope of the exterior surface of the sphere. If one considers the case of a vertical light ray, normally incident on the bubble's surface at the center of the bubble, the critical angle occurs at 0.75 ( $r$ ). Light rays emitted from a laser without divergent optics are all considered to be parallel. Given that the ratio of the indices of refraction,  $m$ , has a value of 0.75 [Van de Hulst, 1957], the critical angle is 48.59 degrees. A sphere of radius,  $r$ , cut directly through the center by a plane forms a circle of radius,  $r$ . For this circle, described by the equation

$$x^2 + y^2 = r^2$$

Equation (7)

or

$$y = \sqrt{r^2 - x^2}$$

Equation (8)

the slope of the surface at any point displaced from the center of the bubble by a

horizontal distance,  $x$ , given as a function of  $x$  as

$$\frac{dy}{dx} = -x * (\sqrt{r^2 - x^2})^{-1}$$

Equation (9)

For a vertical ray of light, the angle of incidence,  $\tau$ , at a distance 0.75 ( $r$ ), measured from the center of the bubble, is exactly 48.59 degrees. Therefore, any light energy incident upon the surface of the bubble from 0.75 ( $r$ ) to the edge will be completely reflected, as shown in Figure (15). Figure (15) shows a bubble viewed from the side, that is, viewed from an angle normal to the viewing angle of the microscope / video camera assembly. The parallel ray source producing the light rays is above the bubble, and all rays incident upon the surface of the bubble are vertical and parallel in this viewing plane. Since the camera will only see light scattered toward it, only the front half of the bubble is shown to be scattering light energy. In reality, the bubble would scatter energy from every point on its upper surface in addition to refracting energy through the entire lower half. This figure does not account for rays which are internally reflected one or more times and then exit the bubble toward the camera, since rays experiencing multiple interior reflections and refractions are strongly attenuated.

Total reflection, no refraction	43.8%
External reflection with refraction	3.7%
Refracted twice	49.7%
One internal reflection	2.3%
Two internal reflections	0.3%
Three internal reflections	0.1%
> Three internal reflections	0.1%

Table (4). Light Energy Distribution for an Air Bubble in Water  
 (after Van de Hulst [1957])

Table (4), above, clearly shows that most of the light energy incident upon the surface to a bubble is either specularly reflected or refracted twice, exiting the bubble as shown in Figure (15). These rays account for the distribution of 93.5% of the incident energy. For this reason, other rays, those experiencing internal reflection, or more than two refractions, were neglected in preliminary optical ray tracing efforts. With the degree of magnification required, the amount of reflected and refracted energy becomes a concern due to the sensitivity of the camera. The addition of a video microscope also affects the amount of light required to be received by the camera. The shutter speeds required to freeze bubble movement in the image (between 1/1000 th and 1/10,000 th seconds), also require much brighter images than an unshuttered camera. As Figure (15) shows, light is scattered in many different directions as rays strike the surface of the bubble. Depending on the width of the viewing field of the camera, however, only a few of the rays are actually imaged by the camera. Figure (16) shows the predicted pattern of total specular reflection from a sphere. It should be noted that this figure does not show any energy which is transmitted through the interior of the bubble, but only the specular reflection of light energy off the upper surface of an air bubble.

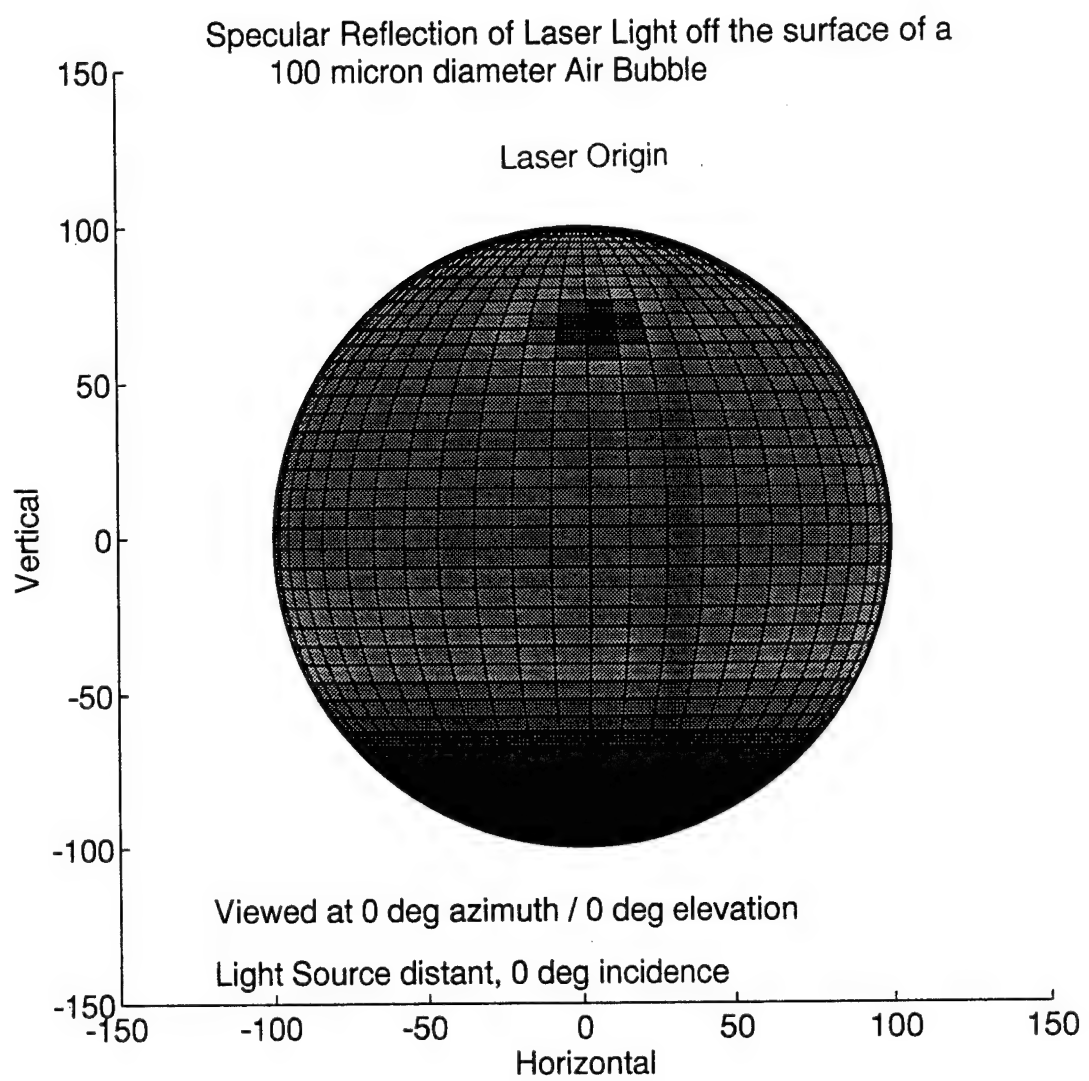


Figure (16). Specular Reflection of Light Energy Incident on a Bubble

Energy refracted twice through the interior of the bubble would not be detected by the camera, as none of it is predicted to scatter in the direction of the camera.

Given the theoretical scattering patterns of the light rays, it was predicted that the image produced of the illuminated bubble with a single illumination source would be a bright dot representing an area of specular reflection off the top surface of the bubble only. In order for the automatic sizing and counting software to detect bubble images, it would be necessary create an image of a bright dot which was easily distinguished from the background.

## 8. Geometrical Optical Approximations

Air bubbles suspended in water have been measured by a variety of methods, as previously discussed. The majority of the methods rely on physical measurement of the actual bubble, either via void fraction volume, photographic image or rise velocity measurements, to name a few. Measurements using scattered light have often relied on illuminating a single bubble with strobe lights, such as in the Light Scattering Bubble Counter [Su et al, 1994]. All of these methods are only applicable for single bubbles, and would not be appropriate in a high density cloud of bubbles typical of the surf zone, or which could be simulated under laboratory conditions. The use of light scattering method under these conditions requires a technique capable of sizing individual bubbles within a population. For this reason, a single direction illumination source was used, and the size of the specular reflection spot was determined from the captured video image. In order for the theory of geometrical optical approximation to apply, as described by Van de Hulst [1957] and Baldy and Bourguet [1985], the following restrictions are required

$$\pi \left( \frac{d}{\lambda} \right) \gg 1$$

Equation (10)

where  $d$  is the diameter of the air bubble and  $\lambda$  = the wavelength of incident light, and,

$$\Delta \alpha \geq 10^\circ$$

Equation (11)

where  $\Delta\alpha$  is the solid angle subtended by the optic aperture of the viewing apparatus. In the size range prescribed by the first assumption, bubbles are characterized by a scattered light "hot spot" which is smaller than the bubble. The size of the "hot spot" is directly proportional to the size of the bubble (Baldy and Bourguet [1985] and Ling and Pao [1988])

$$d_{\text{hotspot}} \approx c_s d_{\text{bubble}}$$

Equation (12)

where  $d_{\text{hotspot}}$  is the diameter of the scattered light "hot spot",  $d_{\text{bubble}}$  is the diameter of the bubble and  $c_s$  is a constant of proportionality which is a function of the scattering angle,  $\theta$ , and the radius of the bubble. If the scattering angle is equal to the angle of incidence of the light energy, the "hot spot" will appear as a circle. The larger the scattering angle, the more elliptical the shape of the "hot spot" will become. Ling and Pao [1988] discuss the shape of the light source as seen by the detector. In their case, a 125 degree scattering angle was used between the axis of a white light source and a photomultiplier. They found that the diameter of the "hot spot" on the surface was approximately 0.10 times the diameter of the bubble. Therefore, using previous notation,  $c_s = 0.10$ . This value is somewhat larger than that found by Baldy and Bourguet [1985]. They utilized a laser light source with a 90 degree scattering angle and found  $c_s = 0.06$ . Figure (10), from Ling and Pao [1988], shows the relationship between the size of the "hot spot" and the scattering angle. The upper portion of the figure shows a ray trace of the ray scattered at the critical angle and the ray scattered at the selected scattering angle. The

lower portion of the figure shows a representation of the image of the "hot spot" as seen by the observer. This portion of the figure has been rotated in order to simplify the picture.

Figure (10) shows that if a shallower scattering angle, 90 degrees for example, was selected, the image of the "hot spot" would have a much smaller minor axis than the image shown. The more acute the angle between the critically scattered ray and the ray scattered at the selected scattering angle, the smaller the displayed "hot spot" image. This is the primary reason for the difference in the proportionality constant found by Ling and Pao [1988] and Baldy and Bourguel [1985]. Baldy and Bourguel [1985] state that the aperture of the viewing apparatus used was  $\alpha = 14$  degrees. Although Ling and Pao [1988] do not detail the aperture of their photomultiplier, it is safe to assume that it is sufficiently large for them to be able to use the geometrical optical approximation to size bubbles in their experiment.

A detailed description of the methods of video capture and data analysis follows in Chapter V.

### III. COHERENT ACOUSTIC SEDIMENT FLUX PROBE (CASP)

The Coherent Acoustic Sediment Probe (CASP) is a multi-frequency underwater sediment flux sensor capable of measuring both the turbulent scale velocity field and suspended sediment flux. It was initially designed and developed at the Naval Postgraduate School (Stanton, 1993) to conduct studies of turbulence in the oceanic boundary layers. The head of the sensor contains a single 1.4 MHz transducer surrounded by three 5.3 MHz transducers, as shown in Figure (17). The 5.2 MHz transducers are positioned radially around the center transducer, separated by 120 degrees. Two axis tilt sensors and three axis accelerometers monitor sensor orientation and motion. Electronic processing and control modules transmit a high speed data stream to a shore based data collection station.

The acoustic package of the CASP is capable of operating in either a monostatic or bistatic mode. In the bistatic mode, a single 5.2 MHz transducer emits a series of 32 short pulses, while the other two transducers receive backscattered acoustic energy from the water column. Following sampling of all thirty two pulses by the other two transducers, the transmission of the next sequence of pulses is electronically switched to a different transducer head. This sequence is repeated with each of the 5.2 MHz transducers. In the monostatic mode, a series of three somewhat longer pulses, referred to as a triplet, is transmitted from each 5.2 MHz transducer. The transducers switch between transmit and receive mode sequentially to measure backscattered acoustic energy amplitudes in each of a series of 1.68 cm range bins out to a range of 1.2 meters.

For calibration purposes, the CASP was positioned in a 600 gallon acrylic test tank in the laboratory. The test vessel in which bubbles or sediment were contained was positioned such that the acoustic beams transmitted by the CASP head would project through an acoustically transparent window in the side of the vessel. This allowed backscattered energy from within the test vessel to be measured by the transducer head

without nearfield interference problems. Figure (18) shows a schematic of the CASP orientation within the test tank in relation to the test vessel.

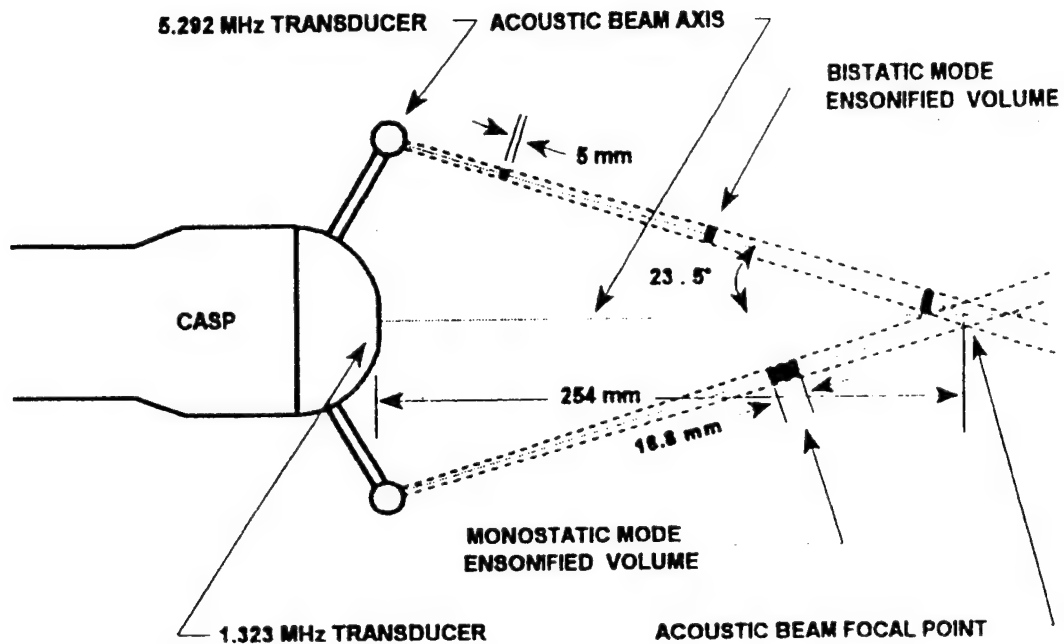
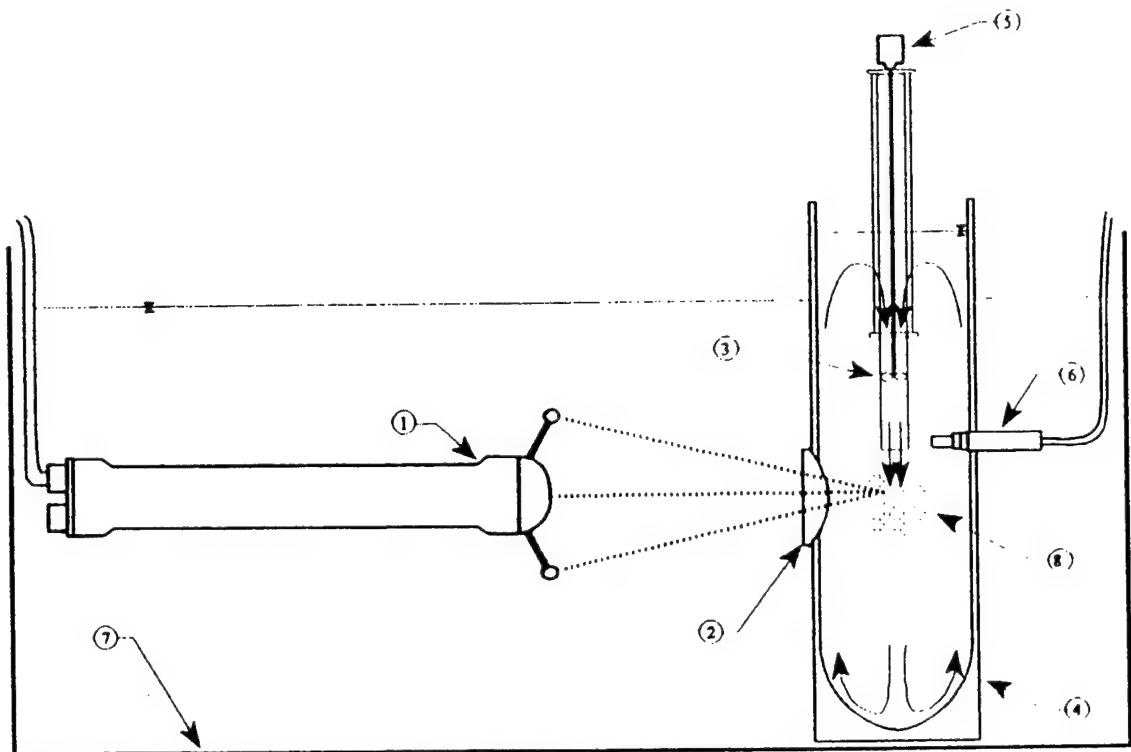


Figure (17). Schematic of CASP System Acoustic Beam Geometry  
(from Stanton [1993])



1. COHERENT ACOUSTIC SEDIMENT PROBE (CASP)
2. ACOUSTICALLY TRANSPARENT MEMBRANE
3. ACRYLIC NOZZLE AND DUCTED PROPELLER
4. ACRYLIC TEST VESSEL
5. VARIABLE SPEED MOTOR
6. OPTICAL BACKSCATTER SENSOR
7. ACRYLIC LABORATORY ACOUSTIC TEST TANK
8. ENTRAINED BUBBLE CLOUD

Figure (18). Schematic of CASP System and Test Vessel (from Stanton [1993])



## IV. ACOUSTIC EFFECTS OF AIR BUBBLES IN WATER

### A. BACKGROUND

Gaseous bubbles occur naturally in the ocean as clouds of air bubbles entrained by breaking surf or falling rain, gas filled bladders in fish and as lung cavities in marine mammals. In general, naturally produced air bubbles occur near the surface when produced by falling rain or breaking waves. The larger of these bubbles rise quickly to the surface, while the smaller bubbles tend to stay resident in the water column for long periods of time, particularly when turbulent mixing is occurring. The presence of high density clouds of bubbles, and therefore a significant amount of air, within a volume can have a profound effect on the speed of sound, and the attenuation and scattering of sound energy due to scattering within that volume. This effect is dependent upon the size distribution and spectral density of the bubble cloud. These influences will be examined in later sections.

### B. SOUND VELOCITY

Air which is dissolved in a volume of water has very little effect upon the speed of sound within that volume, (Urick [1983]). However, air which is present as suspended bubbles has a significant effect upon the speed of sound. Urick states that when the bubbles are much smaller than resonant size, sound speed is dependent upon the density and compressibility of the air and water and the void fraction present within the volume. Void fraction is defined as the amount of air, by volume, present within a sampled volume of water. The simplified relationship for velocity of sound within the mixture is given by Urick as:

$$v = \sqrt{\frac{1}{\rho \kappa}} = v_w \sqrt{\frac{1}{1 + 2.4 \times 10^4 \beta}}$$

Equation (13)

where  $v_w$  = sound speed in water,  $\rho$  = density of the air water mixture,  $\kappa$  = compressibility of the mixture and  $\beta$  = void fraction of air. Even at small void fractions (0.01 percent), the sound speed can be reduced by as much as 53%. At high frequencies, above the resonant frequency of the

smallest bubbles in the cloud, however, the effect of suspended air bubbles on the speed of sound is negligible. Urick gives the relationship between the speed of sound in the mixture,  $c$ , to the speed of sound in water alone,  $c_o$ , as:

$$c^{-2} = c_o^{-2} - \frac{4\pi n a}{(2\pi f)^2}$$

Equation (14)

where  $n$  = the number of bubbles in a unit volume and  $a$  = the radius of the bubble. Bubbles can be considered to be acoustically "large" compared to the resonant size, when all bubbles present within the sampled volume are much larger than the resonant bubble size. This is the case for the surf zone, given previously published studies of bubbles formed due to breaking waves, and the transmitted acoustic frequencies used by the Coherent Acoustic Sediment Flux Probe (CASP). Figure (19) shows a plot of expected surf zone bubble sizes and their corresponding resonant frequencies.

### C. SOUND IN THE OCEAN

Sound propagation in the ocean is effected by a variety of phenomena. As the Coherent Acoustic Sediment Flux Probe (CASP) works over ranges of 1-2 meters at 1.3 and 5.2 MHz, temperature, salinity and pressure can be considered constant and their effects on the speed of sound can be considered negligible. Regardless of range, however, sound energy can be attenuated due to spreading, absorption and scattering within the sample volume. Spreading of sound energy within the water column is considered to be spherical unless boundaries are encountered. Spherical spreading is governed by the relationship

$$TL = 20 \log r$$

Equation (15)

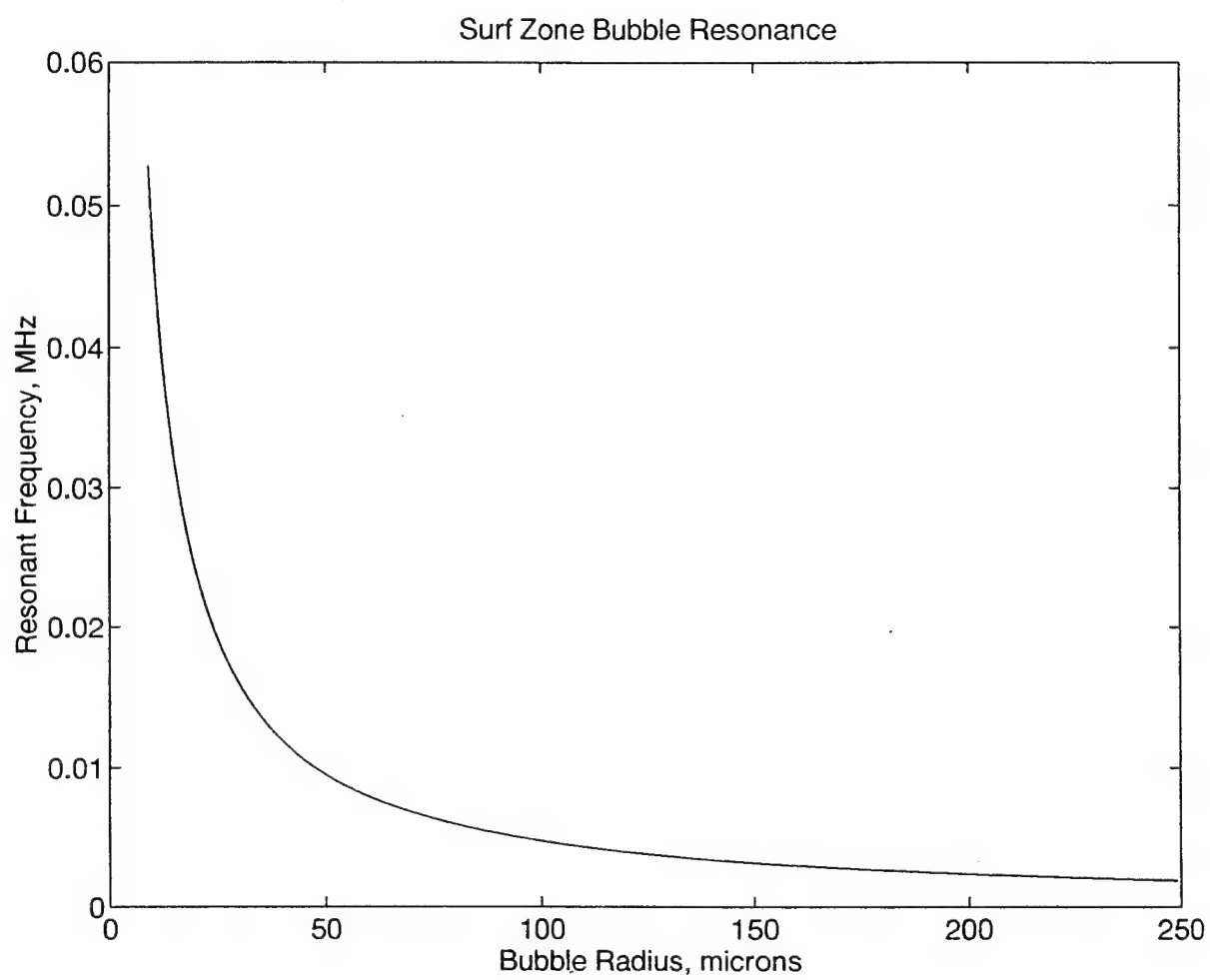


Figure (19). Surf Zone Bubble Resonant Frequencies

where TL is defined as the Transmission Loss experienced by the sound energy due to spreading alone as it travels through the water, and is measured in decibels referenced to 1 micropascal (db re 1  $\mu$ Pa) at a range of one meter from the source on the acoustic axis. When losses due to absorption are included in the spherical spreading law, the relationship becomes

$$TL = 20 \log r + \alpha r$$

Equation (16)

where  $\alpha$  = the absorption coefficient in decibels / meter. The absorption coefficient can be determined using Thorpe's equation

$$\alpha_w = \left( \frac{0.1f^2}{1+f^2} + \frac{40f^2}{4100+f^2} + 2.75 \times 10^{-4}f^2 + 0.003 \right) \times 10^3$$

Equation (17)

where the frequency, f, is in kHz. Sound wave energy attenuation due to the presence of bubbles can be calculated with the relationship

$$\alpha_b = 10 \log \frac{I_1}{I_2}$$

Equation (18)

where  $I_1$  and  $I_2$  are reference intensities measured on the acoustic beam axis one meter apart. If  $n$  resonant bubbles are present within a volume, each with an extinction cross section,  $\sigma_e$  the

attenuation coefficient becomes (The Physics of Sound in the Sea, 1947)

$$\alpha_b = 4.34 n \sigma_e$$

Equation (19)

where the coefficient has the units of decibels per meter. However, since it is assumed that the CASP system will not excite resonance in any of the bubbles found to be resident within the surf zone, this entire term can be disregarded. Given that the CASP is essentially an active sonar emitter, the transmission loss due to range and weak attenuation can be given as

$$TL = 2(20 \log r + \alpha_t r)$$

Equation (20)

where  $\alpha_t = \alpha_s + \alpha_w$ ,  $\alpha_w$  is given by equation (17) and  $\alpha_s$  is the attenuation coefficient due to the presence of scatterers. The factor of 2 arises as the sound energy must travel from the transducer to the "target" and return to the receiver. Scattering losses due to the presence of bubbles and sediment will be covered in a later section.

#### D. RESONANT BUBBLES

Air bubbles suspended in water are subject to resonance due to excitation of the bubble by an incident sound wave. The frequency of bubble resonance is dependent upon the radius of the bubble according to the relationship

$$f_r = \frac{1}{2\pi a} \sqrt{\frac{3\gamma P_o}{\rho}}$$

Equation (21)

where  $f_r$  = resonant frequency of the bubble in Hz,  $\gamma$  = ratio of specific heats of the gas in the bubble (a value of 1.4 for air),  $\rho$  = density of water and  $P_0$  = hydrostatic pressure. For air, at a depth of  $d$  feet under the surface, Urick [1983] simplifies this equation to

$$f_r = \frac{326}{a} \sqrt{1 + 0.03d}$$

Equation (22)

As stated before, and by Urick [1983], only bubbles near resonant size will have an effect on the speed of sound within the water column. At the ultrasonic frequencies utilized by the CASP system, 1.32 MHz and 5.2 MHz, the resonant bubble size, as determined using equation (22) above, is found to be approximately 2.3  $\mu\text{m}$  and 0.627  $\mu\text{m}$ , respectively, for near surface measurements. These bubble radii are far below the size range which has been resolved in previous field measurements, and even if bubbles do exist at the resonant size, viscous effects will probably prevent resonance. Viscous damping is most prevalent at small resonant radii (1 - 10  $\mu\text{m}$ ), but becomes less dominant at radii above 100  $\mu\text{m}$  (Leighton [1994]).

## E. SCATTERING EFFECTS BY OCEAN BUBBLES

Target Strength is defined by Urick [1983] as the echo intensity of incident acoustic energy measured one meter from an underwater target. In essence, target strength, TS, is a measure of the acoustically reflective characteristics of a target. In this case, the targets of interest are clouds of bubbles in the water column. For bubbles at resonance, the scattering cross section,  $\sigma_s$ , and the extinction cross section,  $\sigma_e$ , are approximately three orders of magnitude greater than the geometric cross section, (Leighton [1994]). This can be advantageous when using acoustic vice optical measurement methods. Leighton defines the extinction cross section,  $\sigma_e$ , as the loss of energy from

an acoustic wave resulting from the presence of bubbles. It is given by the relationship

$$\sigma_e = \frac{\frac{4\pi a^2 \delta}{k_r a}}{(f_r^2/f^2 - 1)^2 + \delta^2}$$

Equation (23)

For acoustically "large" bubbles, where  $a \gg \lambda$ , small bubble theory does not apply. In this region, bubbles have an acoustic cross section equal to their geometric cross section, (Urick [1983])

$$\sigma_s = \pi a^2$$

Equation (24)

Quite obviously, the volume scattering strength term is dependent upon the size of the scatterer, in this case, the radius of the bubble. If the bubble population is not made up of uniform sized bubbles, the scattering cross section,  $\sigma_s$  must be determined through integration over the range of bubble radii within the cloud

$$\sigma_v = \int_0^{\infty} n(a) \sigma(a) da$$

Equation (25)

where  $n(a)$  is the density distribution of bubbles in units of bubbles per cubic meter per micron of radius,  $a$ ,  $\sigma(a)$  is the radius dependent scattering cross section and  $da$  is the integration interval.

## F. VOLUME REVERBERATION

Volume reverberation is defined by Urick [1983] as the intensity of sound energy returned to the receiver when a sound source is projected into a volume containing scatterers. These

scatterers can take the form of suspended sediment, zooplankton, phytoplankton or, in this case, air bubbles. The greater the number of scatterers, the greater the amplitude of backscattered energy. Volume reverberation is dependent not only upon the transmission loss through the medium, and the scattering strength of the scatterers within the volume as noted before, but also upon the ensonified volume

$$V = \frac{c\tau}{2} D r^2$$

Equation (26)

where  $c$  is the speed of sound within the medium,  $\tau$  is the pulse duration of the transducer,  $D$  is the half power beam width of the transducer and  $r$  is the range to the ensonified volume. Table (5), below shows the applicable parameter of the Coherent Acoustic Sediment Flux Probe system.

Frequency, MHz	Transducer Radius, cm	Wave-length, cm	Farfield Range, cm	Half Power Beamwidth, degrees	Half Power Beamwidth, cm	Pulse Length, cm
1.323	1.27	0.112	45.2	2.62	1.14	1.68
5.292	0.317	0.028	11.3	2.62	1.14	1.68

Table (5). CASP Monostatic Acoustic Beam Characteristics  
(after Anderson [1994])

The above values are computed for a sound speed,  $c = 1480$  m/s, in fresh water and a pulse duration,  $\tau = 2.26 \times 10^{-5}$  seconds, (Anderson [1994]). Table (6), after Kinsler, et al [1982] shows values of sound speed for fresh and saltwater, for comparison.

Water	Temperature, degrees C	Speed, c, m/s
Fresh	20	1481
Salt	13	1500

Table (6). Sound Speeds in Fresh and Salt Water  
(after Kinsler, et al [1982])

## G. BACKSCATTERED ENERGY

Urick [1983] defines volume reverberation level, RL, as reverberation power measured at the hydrophone. Reverberation is system specific and is given by the relationship

$$RL = SL - TL_{ss} - TL_{sr} + SS + 10\log V$$

Equation (27)

where SL is the source level of the transducer,  $TL_{ss}$  and  $TL_{sr}$  are the transmission loss terms for source to scatterer and scatterer to receiver, respectively. For a monostatic sonar system, these two terms are identical. Although the CASP system can operate in either a monostatic or bistatic configuration, the sound ray paths have equal length, so the transmission loss terms can be combined into a single term. SS is the scattering strength of the scatterers present within the ensonified volume V.

Echo level, EL, is defined as the intensity of the echo reflected from the target measured in the water at the hydrophone. It is given by the relationship

$$EL = SL - 2TL + TS - DT$$

Equation (28)

Urick defines the combination of equations (27) and (28),  $EL - RL$ , as the echo to reverberation ratio. It is the difference between the strength of the echo and the strength of the reverberation due

to scatterers. It is independent of both the source and the medium in which the sound is transmitted. Combining all terms discussed above, the amount of backscattered energy received by the transducer head of the CASP system,  $EL - RL$ , becomes

$$EL - RL = BS_v = TS - (SS + 10 \log V)$$

Equation (29)

where  $BS_v$  is defined as the sound energy backscattered to the receiver by a given volume containing scatterers such as bubbles. This value is still dependent upon the equipment in use, however, the ensonified volume term, shown in equation (26), is dependent upon the bin size, source transmission level, and the sensitivity and directivity of the receiver package. Target strength for a single bubble is given by the relationship

$$TS = 10 \log \frac{\sigma_s}{\pi}$$

Equation (30)

If the scattering cross section  $\sigma_s$  is integrated over the entire distribution of bubbles, as noted previously for the volume scattering term,  $S_v$ , a target strength can be obtained for an entire cloud of bubbles.

## H. VOLUME BACKSCATTER MODEL

In order to obtain a theoretical comparison for laboratory and field measurements, a computer based acoustic model was written using MATLAB. Published bubble density relationships were used in order to determine a theoretical value for backscattered energy, and void fraction measurements. For this model, a variety of bubble densities,  $n(a)$ , were used. These were presumed to be reasonable representations of the expected surf zone size distribution and spectral density. Several bubble size spectra have been reviewed in Section II.B.1. Medwin and Breitz

[1989] found that for bubbles below 60  $\mu\text{m}$  in radius  $n(a) \sim a^{-4}$ , and for bubbles of radius greater than 60  $\mu\text{m}$ ,  $n(a) \sim a^{-2.7}$ . Averaged over the entire distribution, Medwin and Breitz found that  $n(a) = 7.8 \times 10^8 a^{-2.7}$ .  $N(a)$  has the units of bubbles per cubic meter per micron radius. Cartmill and Su [1993] found that the number of bubbles per cubic meter per micron,  $n(a) \sim a^{-3}$ , while Su, Ling and Cartmill [1988] found the dependence to be  $n(a) \sim a^{-4.3}$ . Figure (20) depicts bubble density from 10 to 500  $\mu\text{m}$  using Medwin and Breitz's average density relationship. Figure (21) depicts a plot of theoretical backscattered energy values expected during laboratory experiments using the CASP system's 5.3 MHz transducer, over a range of zero to 1.2 meters, neglecting the backscattered energy received as a result of the test vessel's presence within the large tank. Figure (22) shows the backscattered energy predicted for a bubble cloud contained within the test vessel. For these calculations, acoustic system parameters are shown in Table (5) for the 5.3 MHz CASP frequency. Environmental and bubble size spectral parameters are shown below in Table (7).

Sound Speed	1500 m/s
Bubble Spectral Density	$n(a) = 7.8 \times 10^8 (a^{-2.7})$
Radius Increment	$da = 10 \mu\text{m}$

Table (7). Volume Backscatter Model Parameters

The radius increment,  $da$ , shown in Table (7) above, is used in equation (25) in order to determine the scattering cross section of the modelled bubble population. Figure (23) shows a theoretical attenuation curve for the modelled bubble population. For this model, the theoretical void fraction was found to be  $8.05 \times 10^{-6}$ . This value corresponds well with published void fraction values. Leighton [1994], from Monohan, et al [1987] stated that estimates of void fraction under breaking waves suggest values of  $10^{-4} \%$  to  $10^{-5} \%$ . Lamarre and Melville [1992] from Walsh and Mulhearn [1987] and Farmer and Vagle [1989] found void fraction measurements to be within the range of  $10^{-6}$  to  $10^{-8}$ . It should be noted that Monohan, Walsh and Mulhearn, and Farmer and Vagle conducted open ocean measurements, rather than surf zone measurements. Table (8) shows a summary of field measurement conditions for comparison purposes.

Investigator	Mean Wind Speed	Sample Depth	Void Fraction
Monohan	10 m/s	10 m	$10^{-4}$ - $10^{-5}$ %
Lamarre and Melville	4.5 - 14.9 m/s	0.2 m	above 0.3 %

Table (8). Field Void Fraction Measurement Conditions

Lamarre and Melville's impedance probe was incapable of measuring void fractions lower than 0.3%. The data shown above is a clear illustration that void fraction decreases rapidly with depth. At a depth of 10 meters, entrained bubbles due to wind action are likely to be very small, as larger bubbles would have risen to the surface before deep entrainment was accomplished. Near the breaking surface of the wave, as in Lamarre and Melville's experiment, the void fraction is expected to be much higher, with a broader spectrum of bubble sizes. Of interest, Lamarre and Melville [1992] state that at void fractions above 0.3%, temperature effects on the impedance of the surrounding water are negligible.

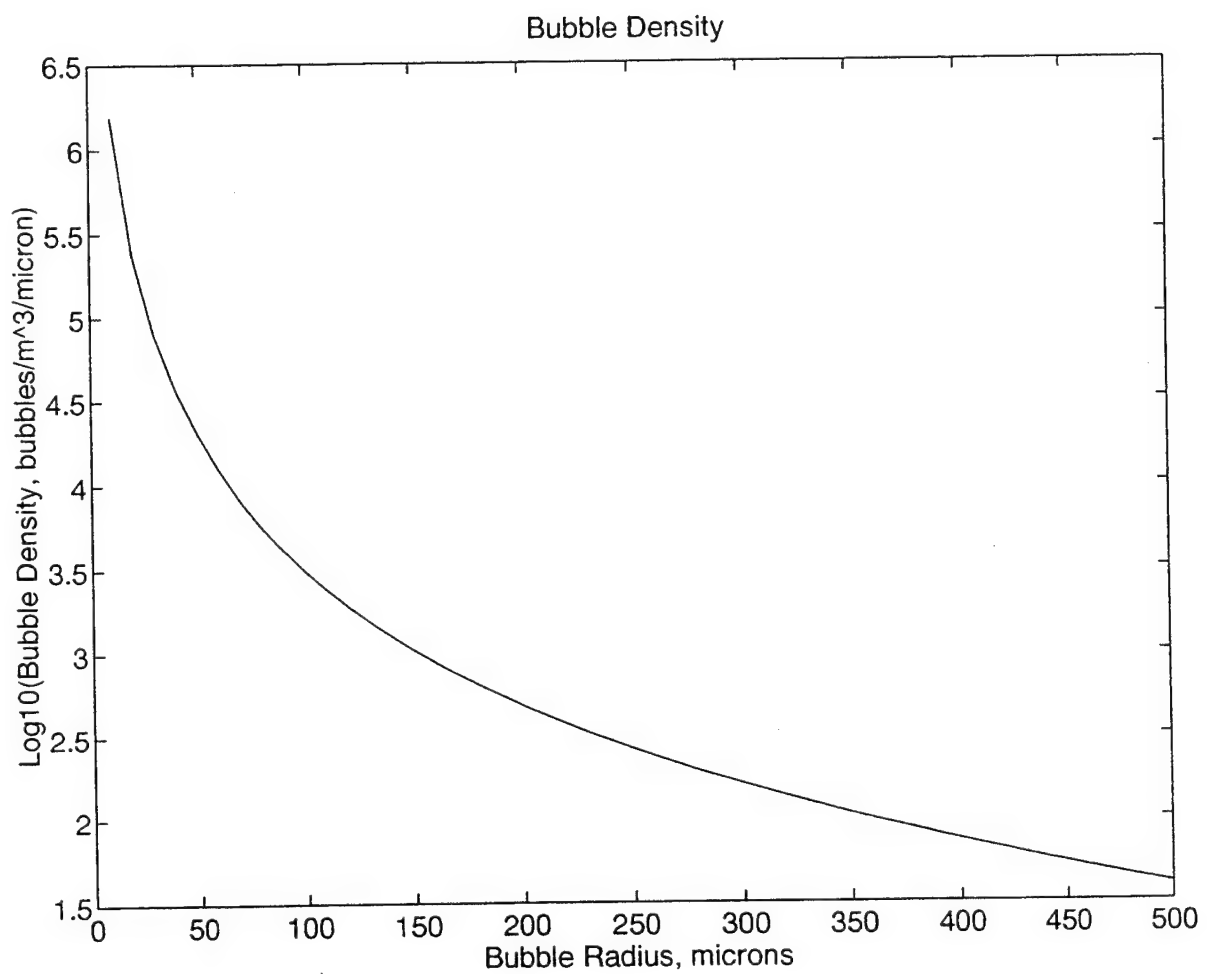


Figure (20). Modelled Bubble Spectral Density, 10 to 500  $\mu\text{m}$  Radius

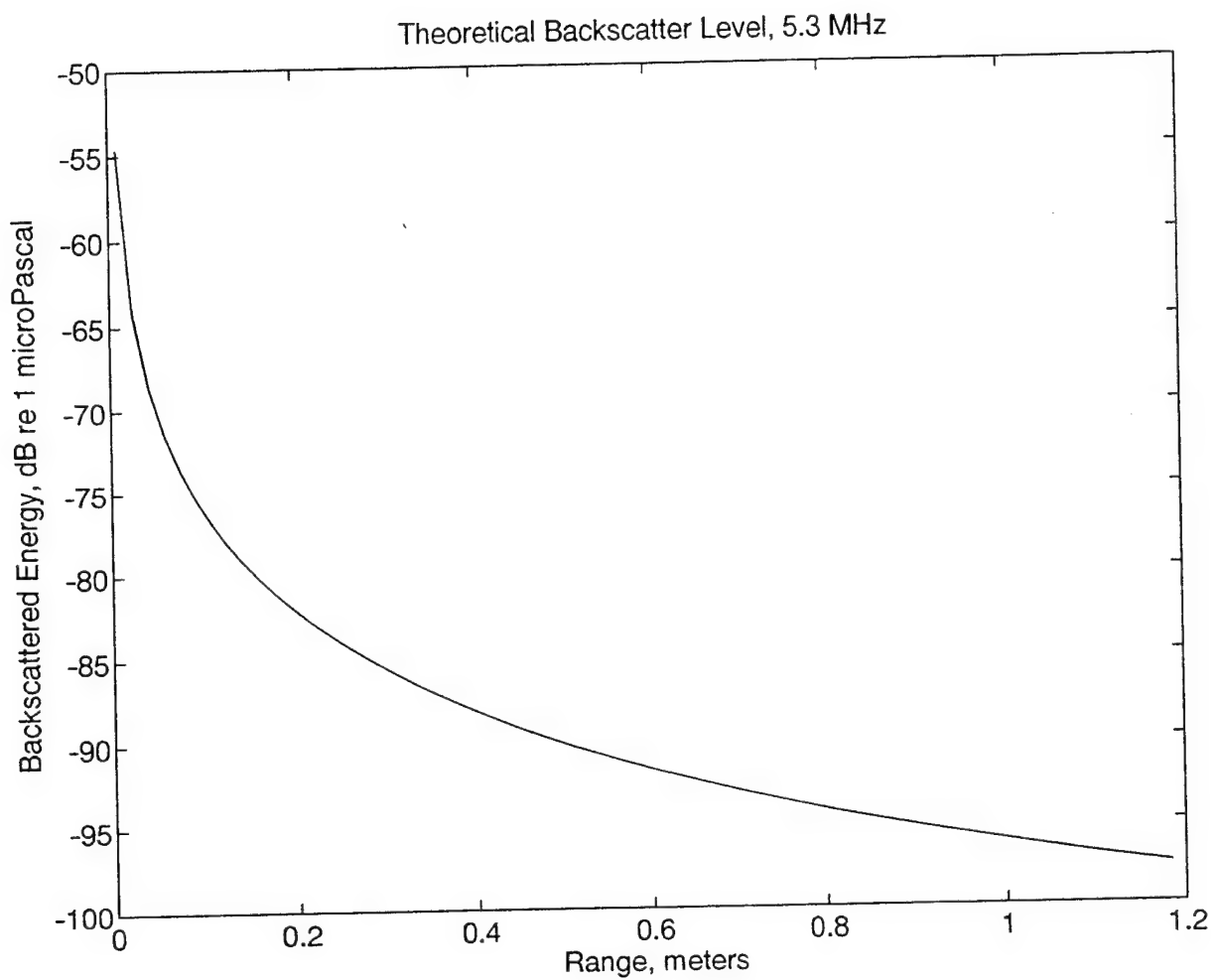


Figure (21). Modelled Backscattered Energy for 5.3 MHz CASP Frequency

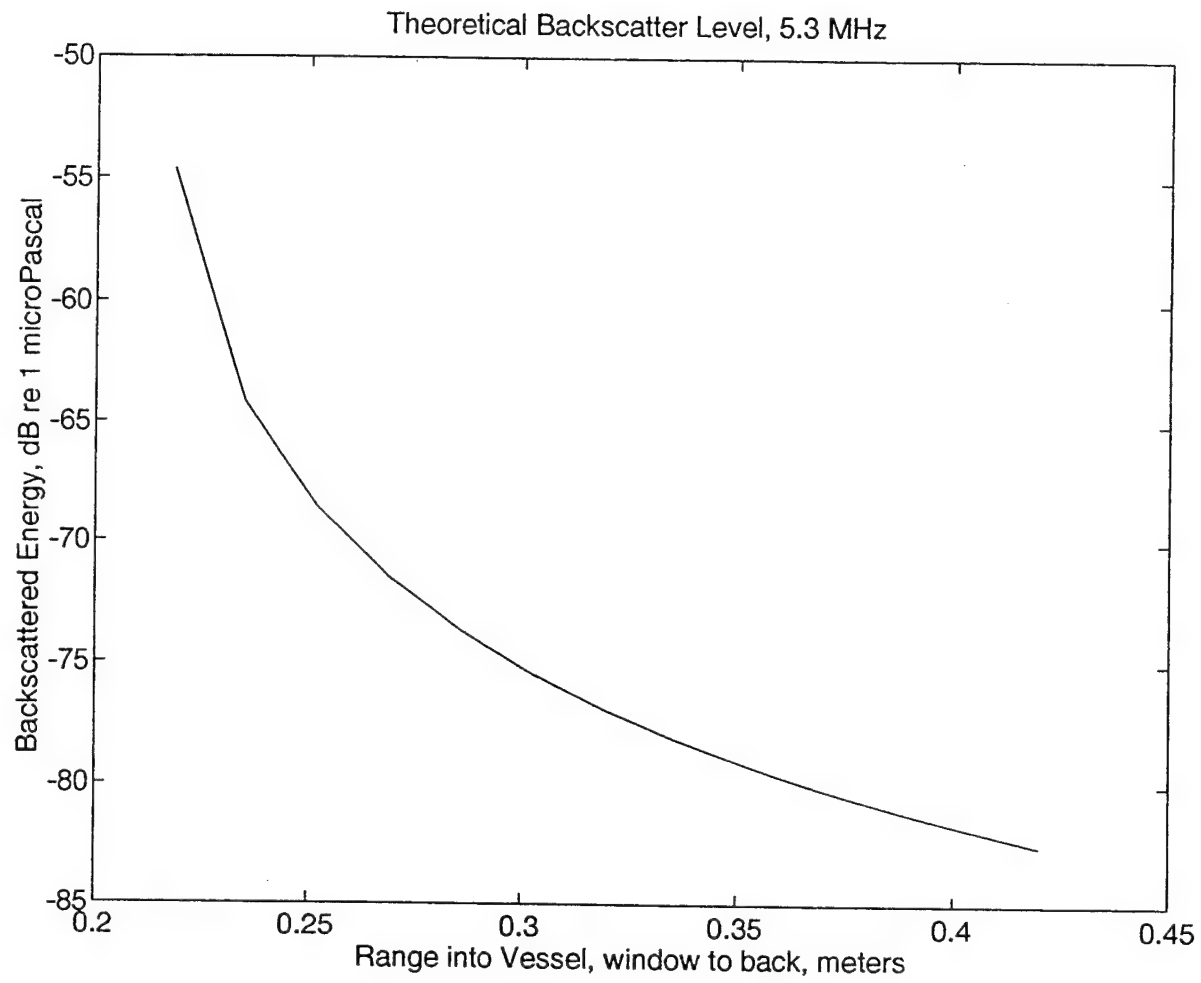


Figure (22). Modelled Backscattered Energy for 5.3 MHz CASP Frequency in Test Vessel

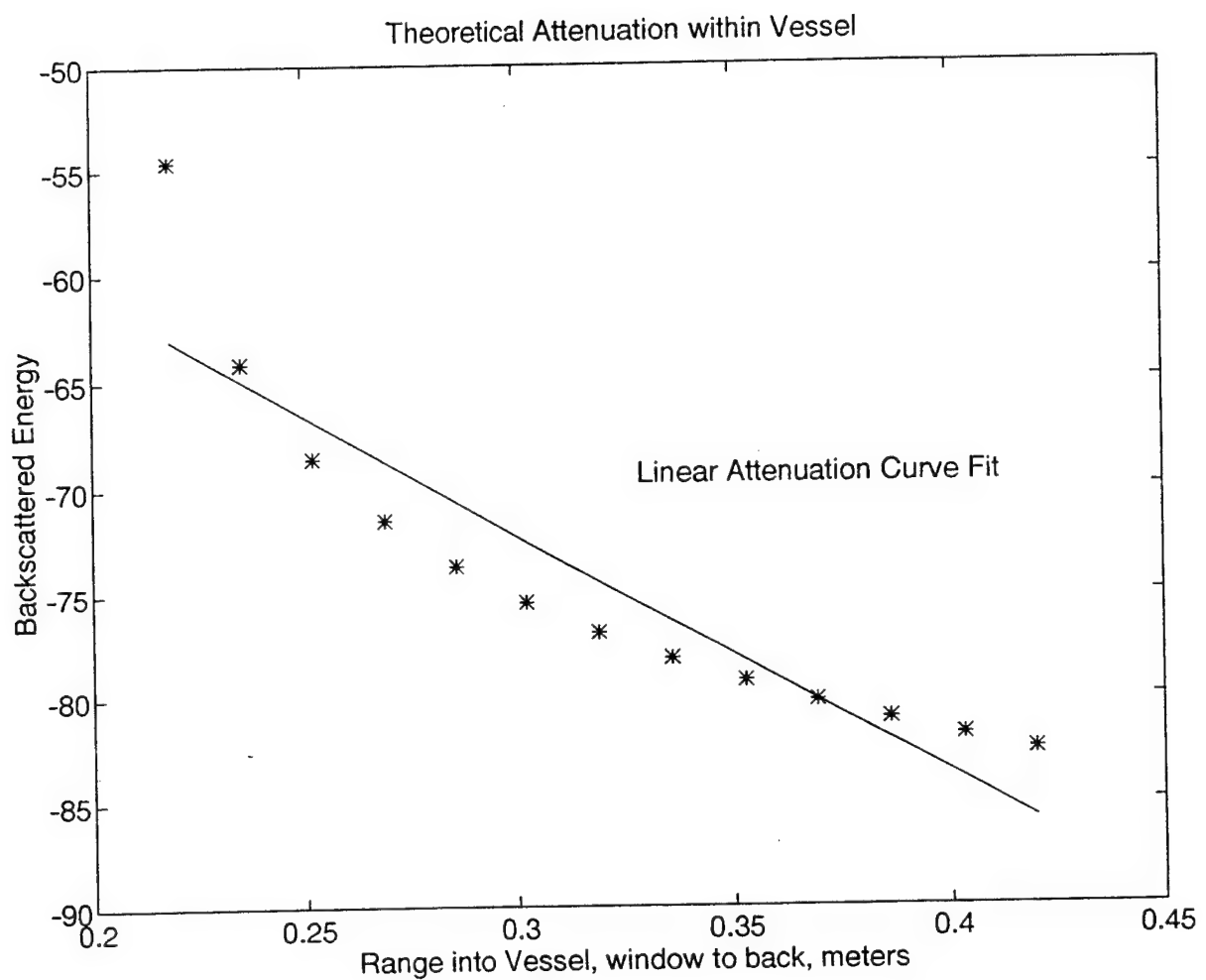


Figure (23). Estimated Attenuation Curve

## V. INITIAL EXPERIMENTAL TESTING

### A. SINGLE NITROGEN BUBBLE TESTS

In an effort to visualize the laser light scattering effects of air bubbles in water and to realize potential illumination problems, a simple, controlled experiment was conducted. The apparatus used included the laser and mirror arrangement previously discussed in addition to the camera and microscope assembly used to videotape the results. Bubbles were produced using a single hypodermic needle fed by a pressurized nitrogen tank. The needle was submerged in the test volume with the exit point positioned just above the vertex of the two mirrors suspended below the laser and was placed at an angle in order to ensure that the needle itself would not interfere with either the laser light fan or the free rise of the bubbles. The flow of nitrogen from the tank was controlled using a metering valve to reduce the flow so that single bubbles were viewed in each frame. With a turbulent cloud of air bubbles in the test volume, it was very difficult to distinguish individual bubbles and therefore difficult to determine the spectral density of the population. With a single bubble, the specular reflection pattern could be easily studied. Additionally, the hypodermic needle produced a stream of uniformly sized bubbles which simplified the study of the reflective patterns. Equipment parameters are shown in Table (9).

Metering Valve Inlet Pressure	Bubble Flow Rate	Camera Shutter Speed
24 psi	5 / sec	1 / 1000 sec

Table (9). Single Nitrogen Bubble Test Equipment Parameters

Figure (13) showed the orientation of the laser head in relation to the mirrors. The laser was fitted with a beam spreader which produced a fan of light 0.3 mm deep spread 15 degrees

either side of centerline. This arrangement essentially functioned as three light sources, with the laser illuminating bubbles from above and the two mirrors illuminating the bubble from below. Theoretically, this would produce three "hot spots" on the surface of each bubble. The beam spreader significantly reduced the laser light intensity, which required selection of a shutter speed which would provide sufficient illumination of the bubbles. It was found that shutter speeds slower than 1/1000 th of a second resulted in smearing of the images of bubbles as the bubbles rose.

Resultant images of bubbles showed a distinct pattern of three bright dots on the surface of the bubble. These "triples" represented the reflected images of the laser light incident upon the surface of the bubble. The image was quite similar to that shown in Figure (10), from Figure (4) of Su, et al [1994]. In their image, three dots, produced by photographic strobes, appeared on surface of the bubble. The spacing of these dots was then used to determine the size of the bubble.

With a single bubble present within a viewing frame, it is simple to perform the required measurements. Due to a bubble's position within the light fan, some would only display one or two "hot spots", rather than three. Obviously, a single hot spot could not be used to determine the bubble's size as detailed by Su, et al [1994]. Two "hot spots" could be used in this manner to provide a somewhat less robust result. However, with a cloud of bubbles present within a viewing frame, there was no simple method to separate individual bubble triples either visually or through the use of computer automated image analysis. In cases where an individual bubble displayed more than one "hot spots", the spots were often of different intensities. This was found to be a function of the orientation of the laser apparatus in relation to the camera. In order to achieve uniform illumination, the camera viewing plane and light fan had to be precisely parallel with the fan of light produced by the laser. To overcome these limitations a different approach had to be undertaken.

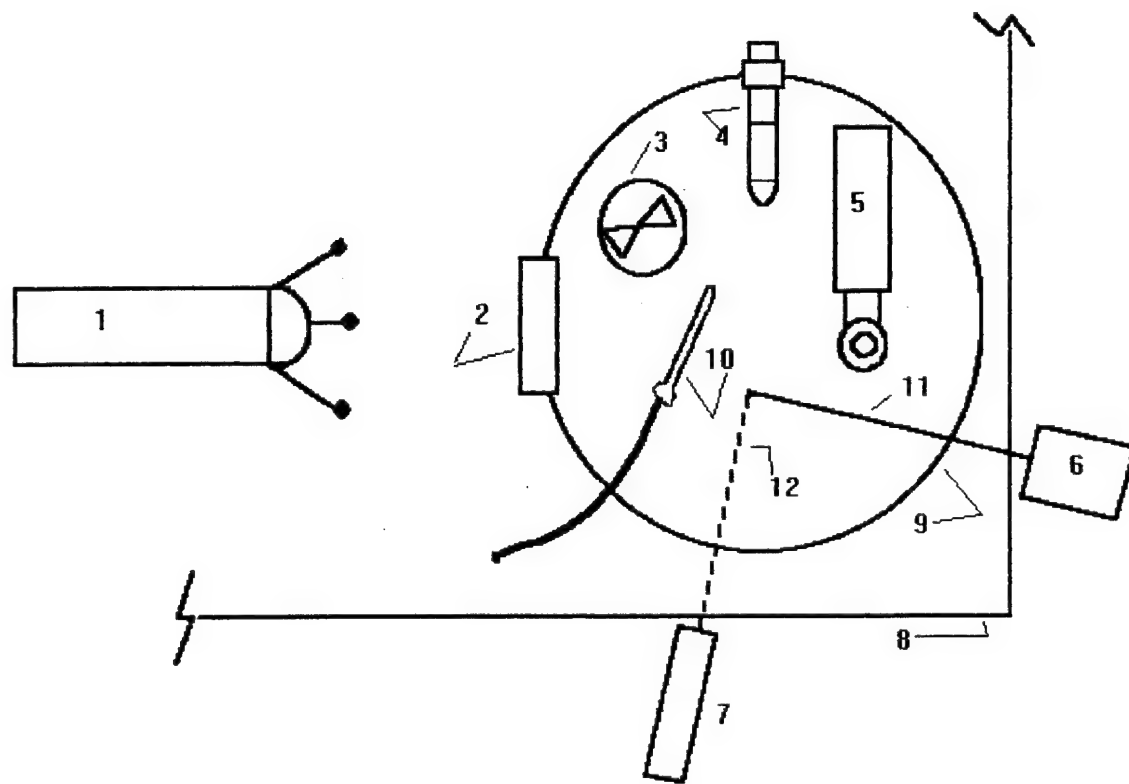
## B. SINGLE REFLECTION METHODS

There was no guarantee that each individual bubble would display three "hot spots" of equal intensity due to its position in the light beam. Statistically, this would pose a problem if a small number of bubbles were imaged and a large number of those displayed only one or two "hot spots". In single bubble tests, this theory was easily tested. Visual analysis of captured video images revealed that even in this controlled bubble flow, the number of hotspots displayed varied from bubble to bubble. For this reason, and given the turbulent nature of the test vessel during stirring, a single source illumination method was selected for use with a 90 degree scattering angle.

During the laboratory runs described above, the brightness of the captured bubble image was dependent upon both the intensity of the incident laser light, and the shutter speed of the camera. In order to increase the resolution of a single "hot spot", to reduce image smearing, the shutter speed of the camera was reduced to 1/4000 th second. To further increase the resolution, the magnification of the microscope was doubled, which required a quadrupling of the incident light intensity to sufficiently illuminate the surface of the bubble. In order to increase the intensity of laser light, the beam spreader was removed to produce a narrow beam which was of much higher intensity than the fan of light produced with the beam spreader installed. Although the light energy distribution across the beam was considered to be Gaussian, this unmodified beam had a nominal diameter of 0.35 mm, and was considered to be cylindrical. The increased light intensity produced by this beam allowed for the use of a 1/4000 th second shutter speed selection on the camera. This would prove critical during bubble illumination in a turbulent tank in order to reduce video image smearing caused by illumination of high velocity bubbles.

Figure (24) shows a plan view of the relative orientation of the equipment used during final experimental runs, which will be discussed in greater detail in Chapter VI. As can be clearly seen, there was very little unused space within the test vessel during experimentation. This was a primary factor in selecting a ninety degree scattering angle

rather than any other. The camera / microscope assembly was oriented so that the viewing axis was perpendicular to the axis of the laser beam inside of the vessel. This orientation took into account the refraction of the beam as it passed through both the plexiglass walls of the tank and vessel and the water.



1. CASP
2. Acoustic Window
3. Laboratory Stirrer
4. Optical Backscatterance Sensor
5. Conductivity Cell
6. Laser
7. Camera and Microscope
8. Laboratory Tank Wall
9. Test Vessel Wall
10. Above Water Jet
11. Laser Beam
12. Camera Viewing Axis

Figure (24). Laboratory Apparatus Tank Orientation

### C. IMAGE PROCESSING

The illuminated bubble cloud was imaged with a microscope and electronically shuttered video camera. Specifications for both the camera and microscope are shown in Tables (10) and (11).

Video Camera	Type	Electronic Shuttering
Cohu 4915	Monochrome HAD	to 1/10000 sec

Table (10). Video Camera Specifications

Microscope	Field of View (FOV)	Aspect Ratio
Infivar Video Scope	2 cm	1 : 1.067

Table (11). Microscope Specifications

The aspect ratio is based on the viewing plane dimensions (512 x 480 pixels). Initially, a commercial image processing software package was sought to analyze video images in order to size and count the bubbles and to estimate a size spectrum. Several different packages were investigated, but each of these packages were rejected due to limitations in the scripting language needed to automatically size the bubbles. The software was required to automatically size and count a wide range of bubble radii within the test vessel, often sizing several objects within the same frame simultaneously. In order to achieve the required flexibility, a C-callable routine was developed "in-house" which wrote object sizes to an ASCII file which could later be analyzed using a MATLAB algorithm.

Recorded video images were played back through a Matrox MVP framegrabbing package to capture individual video frames. Captured frames were analyzed for the presence of bright areas within the frame above a specified threshold level. These recorded images were measured and counted using a C-callable algorithm which measured both the width and height of the images within a captured frame. Careful selection of a threshold

level was required in order to ensure an accurate depiction of the spectrum of bubble images. Low threshold values resulted in a great deal of "noise" present within the frame while too high a value resulted in very few detected objects. Secondary external reflections, internal refractions and reflections are ignored using this method as the intensities of these bright areas are significantly lower than the primary hotspots. This is shown quantitatively in Table (4), from Van de Hulst [1957].

The sizing routine sampled roughly 100 frames per minute, freezing each frame and performing the searching and sizing algorithm. While the sizing routine measured both width and height, it was found that the height was an unreliable value due to the presence of blank horizontal lines of video data interlaced between each valid line of data when the camera was used in the shuttered mode. As described in Section II.B.8, the laser illuminated bright areas within each frame were not images of the entire exterior surface of the bubble, but were the specular reflection of the laser light off the exterior surface of the bubbles as seen by the video camera and microscope assembly.

## VI. EXPERIMENTAL RESULTS

### A. BUBBLE PRODUCTION MEDIUM

Experimental runs were conducted with both fresh and seawater in the test vessel. As different bubble spectra were expected, both fresh water and salt water runs were conducted. The plan was to evaluate data sets to not only confirm the produced bubble spectrum, but to determine the acoustic effects of bubble clouds within the test vessel. Using the chosen bubble production method of above water jet entrainment, bubbles were illuminated using a 45 milliwatt, 532 nanometer laser and counted and sized with the algorithm discussed in Chapter V. Optical Backscatterance Sensors provided a qualitative means to analyze the resident bubble population. Void fraction was estimated through the use of a conductivity cell. Additionally, the Coherent Acoustic Sediment Flux Probe (CASP) was used to produce acoustic backscatter levels for each bubble population. A detailed description of each of the above noted experimental steps follows.

#### 1. Fresh Water

Fresh water experiments used fresh deionized and filtered water. Following deionization, the water was filtered through a 20  $\mu\text{m}$  and a 1  $\mu\text{m}$  filter, in succession. These precautions were taken in an effort to minimize the amount of contaminants present within the test vessel. These contaminants could have taken the form of suspended particles, biotic particles, oils and other surfactants which would each have a potential effect on the produced bubble spectrum, and the backscatter properties of the medium. Additionally, the laser imaging system could not discriminate between bubbles and suspended particles.

#### 2. Simulated Sea Water

Salt water runs were conducted utilizing simulated sea water. Salt water runs were necessary in order to simulate the conditions experienced in the surf zone as closely as possible. Sea water would effect the conductivity of the medium, as well as the distribution

and size of the resident bubble population, as discussed in Chapter IV. Bubbles produced in salt water are, in general, more numerous and more persistent than in fresh water. Table (12), below, shows the constituent breakdown of the sea salt used to create the simulated sea water. The salt used in the experimental process was produced by the Lake Products Company of Maryland Heights, Missouri, under the product name, "Sea Salt".

<u>Chemical Constituent</u>	<u>Percentage</u>
NaCl	58.49
MgCl <sub>2</sub> - 6H <sub>2</sub> O	26.46
Na <sub>2</sub> SO <sub>4</sub>	9.75
CaCl <sub>2</sub>	2.765
KCl	1.645
NaHCO <sub>3</sub>	0.477
KBr	0.238
H <sub>3</sub> BO <sub>3</sub>	0.071
SrCl <sub>2</sub> - 6H <sub>2</sub> O	0.095
NaF	0.007

Table (12). Chemical Constituents of Sea Salt

According to the manufacturer, "Sea Salt" is a simulated sea salt mix containing elements found in natural sea salt in quantities greater than 0.004%. In order to produce a simulated sea water, 41.953 grams of sea salt were added to each liter of fresh water to produce sea water, or for the test vessel, 600 grams of salt were added to approximately 14.5 liters of deionized fresh water. Table (13) shows the conductivity readings obtained using an AutoSal machine to determine the salinity of the water used during simulated sea water runs.

Trial Number	(2x) Conductivity Ratio	Salinity, ppt
1	1.3766	23.08
2	1.37661	23.0802
3	1.3766	23.08

Table (13). AutoSal Salinity Test Results of Vessel Water

It should be noted that all three above trials were conducted at 24 degrees centigrade. Although the salinity of the sample tested was much lower than actual seawater, it was sufficient for the conductivity cell to operate effectively. As stated previously, deionized water and the sea salt were used in an effort to reduce the amount of contaminants within the test vessel, rather than actual sea water which could introduce biologic and other particles into the test volume.

## B. BUBBLE POPULATION VARIATION

Two experimental runs were conducted using salt water, and one using fresh water. Fresh water was expected to produce larger bubbles when compared to the finer, smaller bubbles produced in salt water. In order to effectively validate the results, two salt water runs were necessary. During each run, four bubble production rates were attempted by using a needle valve to control the flow of water from the pump through the above water jet apparatus. Water flow was controlled in one half turn steps. Following approximately ten minutes zero bubble unstirred data, the vessel was stirred for five minutes prior to bubble production. The valve was opened one half turn, producing a low flow rate through the jet. With this jet flow, the corresponding bubble population produced within the test vessel was allowed to stabilize for ten minutes. The valve was then opened an additional half turn for an additional ten minutes. This procedure was continued for two more half turn steps, each for ten minutes. It was hoped that each of these steps would produce a bubble cloud of increasing population density without altering the spectrum produced. A discussion of the

spectrum produced follows in section E. Table (14) shows point indicators and the corresponding needle valve setting. These indicators apply to all time series plots in following sections for saltwater experimental runs conducted on 03 and 07 August 95.

Point Indicator	Needle Valve Setting
A	0.5
B	1
C	1.5
D	2
E	Off

Table (14). Time Series Point Indicators

### C. OPTICAL BACKSCATTER RESULTS

Optical backscatter results were obtained using the Optical Backscatterance System (OBS) manufactured by the D & A Instrument Company of Port Townsend, WA. A specification sheet for this system is included as appendix (A). The OBS system is designed to be used for turbidity measurement in water and is not advertised as having the capability to detect bubbles. Bubbles, apparently, do not have the proper opacity to be effectively detected by the system. Despite this, it was felt that this system would provide another means of detecting changes in bubble population density, even if this was only on a qualitative basis. It was not expected that this system would provide accurate quantitative data with respect to bubble populations produced within the test vessel. Figures (25) and (26) show the optical backscatter voltage time series produced during two separate salt water experiments. The upper plot is the time series decimated to a 1 hz sampling rate, while the lower one shows a time series decimated to a 0.05 Hz sampling rate. This has the effect of

removing perturbations caused by large bubble transients. In each of these figures, the open circles denote times during the run where the jet flow was increased.

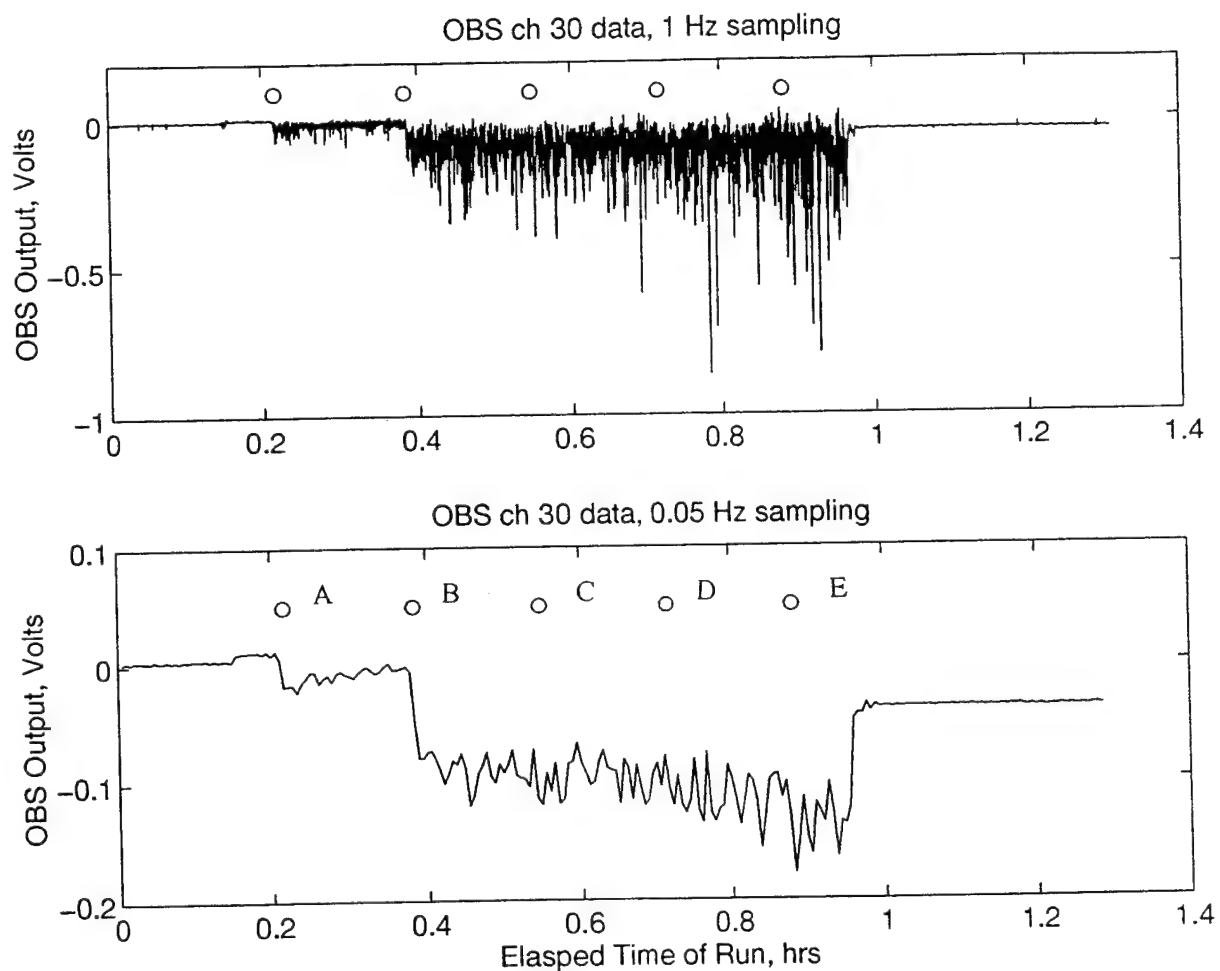


Figure (25). Optical Backscatter, 03 August 95

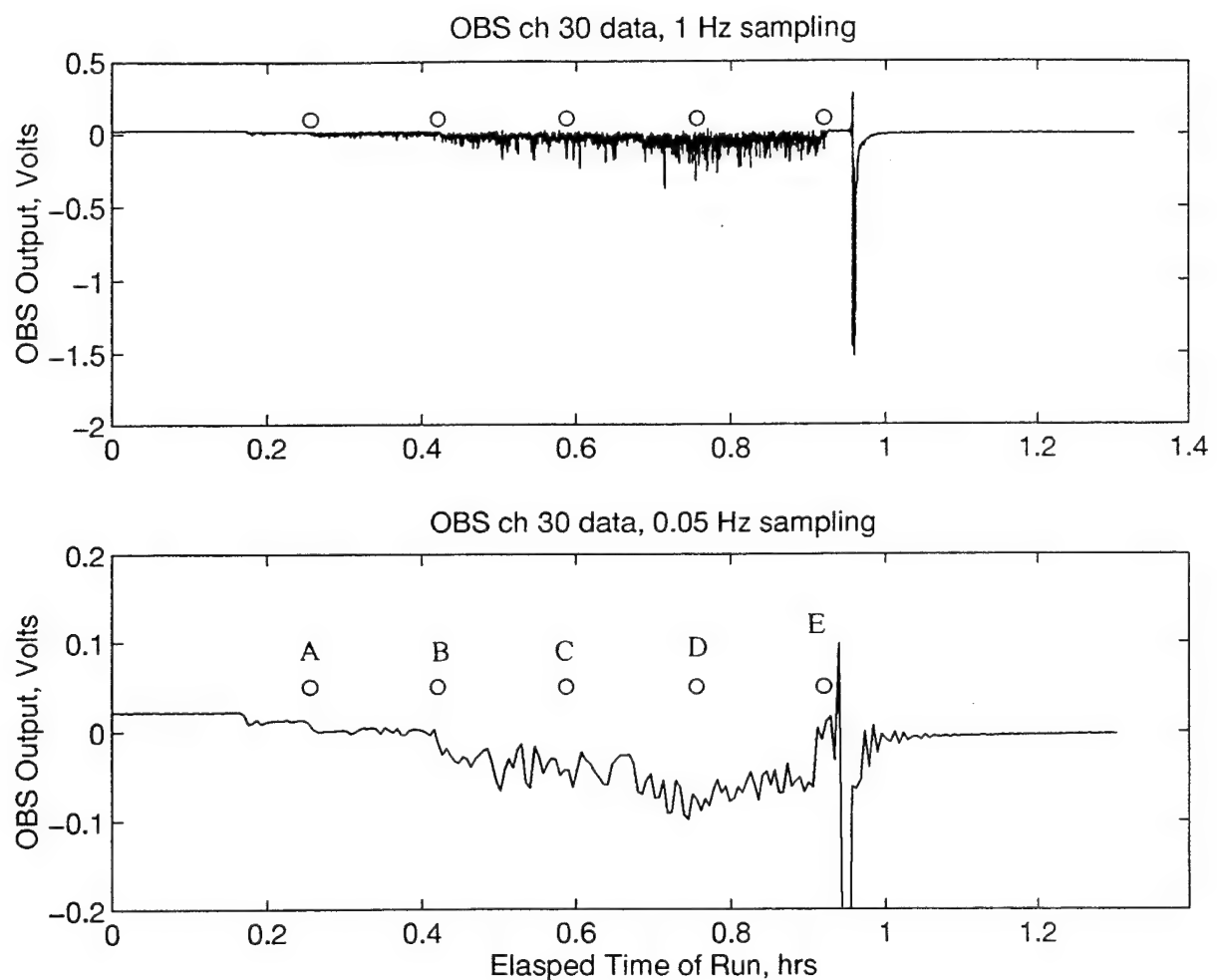


Figure (26). Optical Backscatter, 07 August 95

As can be clearly seen from these two figures, there is a definite increase in the signal following the initial opening of the valve, approximately 0.2 hours into the experimental run in Figure (25) and approximately 0.25 hours into the run in Figure (26). An increase is again apparent at point (B). Subsequent increases in flow rates, at points (C) and (D) are less distinct in these figures. This not only indicates that the OBS system is at least partially capable of detecting bubbles within a volume, but more importantly, that the bubble density was, in fact, changing with increases in flow rate through the jet, at least through point (C). The large perturbation in Figure (26), near point (E) was caused by high speed agitation of the test volume with the laboratory stirrer mechanism. This was done in an effort to check the effects of a completely saturated environment on the sensors in use. During this agitation, the vessel contained a very high void fraction and was nearly opaque. The degree of the opacity is apparent from the OBS signal.

#### **D. CONDUCTIVITY CELL RESULTS**

Void fraction was estimated from the conductivity of the fluid within the test vessel during each experiment. Since the presence of air in the fluid decreases the electrical conductivity as the number of bubbles within the vessel increases, the fluid's conductivity decreases. An inductive conductivity cell produced by the Falmouth Scientific Company was used in the tank.

##### **1. Calibration**

The conductivity cell was calibrated with an autocell to understand the relationship between counts (representing digitized voltages within the CASP), volts, and mmohs / cm, units of conductivity. A specification sheet on the conductivity cell is included as appendix (B). Calibration data for the conductivity cell used in the experiments is shown below in Table (15), and voltage calibration of the analog input was determined by connecting a precision voltage source and measuring the resulting digitized counts. Each voltage setting

Conductivity Calibration Results 8/8/95

Instrument type: Conductivity      Manufacturer: NPS  
 Model: FSI      Serial number: 1494  
 Sensor: Conductivity  
 Sensor interface: 1637800592      Sensor serial number: 1494

Standard serial number: Y2      Bridge serial number: 1027  
 Calibrator: BRUCE  
 Comments: PRE COPE EXPERIMENT

Point #	X Volts	Y Conductivity, mMohs/cm	X stddev	Y stddev	Quality
1	1.10590	51.68650	0.00E+00	0.00E+00	0
2	1.10580	51.69000	0.00E+00	0.00E+00	0
3	.48980	42.46390	0.00E+00	0.00E+00	0
4	.48980	42.48950	0.00E+00	0.00E+00	0
5	.03170	35.22100	0.00E+00	0.00E+00	0
6	.03160	35.23050	0.00E+00	0.00E+00	0
7	-.49820	27.37320	0.00E+00	0.00E+00	0
8	-.49830	27.37460	0.00E+00	0.00E+00	0
9	-.91730	21.45110	0.00E+00	0.00E+00	0
10	-.91720	21.42490	0.00E+00	0.00E+00	0

Conductivity Calibration Results 8/8/95

Instrument type: Conductivity      Manufacturer: NPS  
 Model: FSI      Serial number: 1494  
 Sensor: Conductivity  
 Sensor interface: 1637800592      Sensor serial number: 1494

Standard serial number: Y2      Bridge serial number: 1027  
 Calibrator: BRUCE  
 Comments: PRE COPE EXPERIMENT

Linear model: Y=A+B\*X  
 A= 35.0041021701  
 B= 15.0240280901

X in Volts   Y in deg C (IPTS68)

Fit parameter R=(explained sum of squares/total sum of squares) \*\*1/2 =  
 .999869754126

Table (15). Conductivity Cell Calibration Results

was maintained for 15 seconds before selecting the next step. With a known input voltage, a corresponding response was determined in an effort to obtain a conversion factor between voltage and counts. The results of this calibration are shown below in Table (16).

Input Volts, DC	Cell Response, counts	counts / volts
0	-43.9883	n / a
1	-6378.3	6334
2	-12830	6393
3	-19282	6413
4	-25616	6393
5	-32185	6428
Mean Conversion		6383.18

Table (16). Conductivity Cell Voltage Calibration Data

Taking the initial offset of -44 counts at an input of 0 volts into account, the relationship between input voltage and cell response in counts is linear. Calibration testing resulted in the following relationship

$$C = \left( \frac{46.74 \text{ mmohs/cm}}{\text{volts}} \right) \left( \frac{\text{volts}}{6383.2 \text{ counts}} \right) (\text{counts})$$

Equation (31)

where C is the conductivity of the fluid. As a second test of the conductivity cell's response within the test vessel, several readings were taken with the conductivity cell in a variety of positions, both in and out of the water. Results of this test are shown in Table (17). It should be noted that the readings were fairly consistent throughout the test. Of note, the proximity of the edge of the cell to the wall or other obstructions had little or no effect on

the conductivity reading. However, if the open end of the cell was placed near another piece of equipment or the vessel wall, there was a marked effect, quite similar in magnitude to the reading obtained during the high turbulence stirring portion of the test.

Test Number	Position / Condition	Conductivity, mmohs/cm
1	Out of water / Dry	106.174
2	In water / Center of tank	38.076
3	Out of water / Wet	106.174
4	In water / Center of tank	37.344
5	In water / Touching Wall*	38.076
6	In water / Touching Wall**	40.272
7	In water / Turbulent stirring	40.272
8	Out of water / Wet	107.638

Table (17). Conductivity Cell Position Test Results

Notes - \* Side of cell touching wall, \*\* Opening of cell touching wall

## 2. Conductivity Results

The conductivity cell was used to estimate total void fraction data for each of the produced bubble populations. Void fraction is determined from the relationship

$$\alpha = \frac{1 - \frac{\sigma_{eff}}{\sigma_w}}{1 + \frac{\sigma_{eff}}{\sigma_w}}$$

Equation (32)

where  $\sigma_w$  is the conductivity of the water,  $\sigma_{eff}$  is the effective conductivity of the water

containing bubbles and  $\alpha$  is the void fraction of air within the sample volume. determination of the conductivity and effective conductivity of the water will be discussed in the next section. Figures (27) and (28) show conductivity cell signals plotted against elapsed experimental run time. Once again, the open circles denote times when the flow rate of the entrainment jet was increased. Unlike the OBS data shown in Figures (25) and (26), there is no distinct decrease in the conductivity signal following flow increases. Figure (27) shows the most distinct change in the conductive nature of the medium with an increase in the bubble population after the second increase in flow rate, at point (B). Following that, there is a gradual decrease in conductivity, rather than distinct steps. It is likely that the conductivity cell in use experienced an unknown malfunction as the cell can resolve 0.002 mmohs / cm changes in conductivity. This is confirmed by the fact that after bubble production had ceased, approximately one hour into each run, the conductivity cell readings did not return to the level registered at the beginning of the run. Initially, it was thought that this was a result of bubbles becoming trapped within the conductivity cell's center. This was discounted when the laboratory stirring apparatus was run at high speed momentarily. The result of this effort can be clearly seen in Figure (28), at approximately one hour. The conductivity reading immediately returned to the value registered at the end of bubble production. Data shown in Figure (28) is further corrupted by the presence of suspended particles which will be discussed briefly in the next section. Unfortunately, this prevented void fraction from being accurately estimated using conductivity cell data.

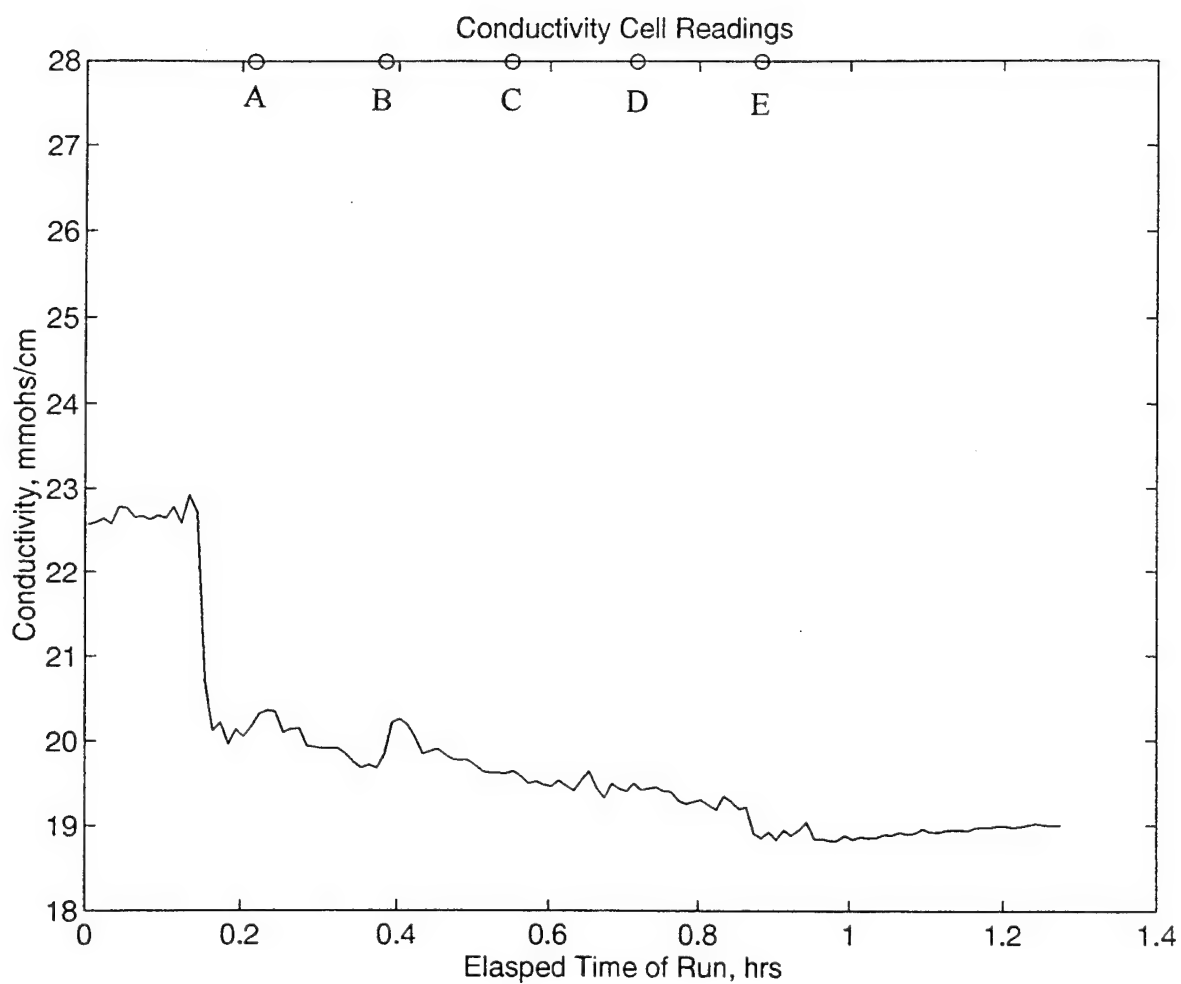


Figure (27). Conductivity Cell Results, 03 August 95

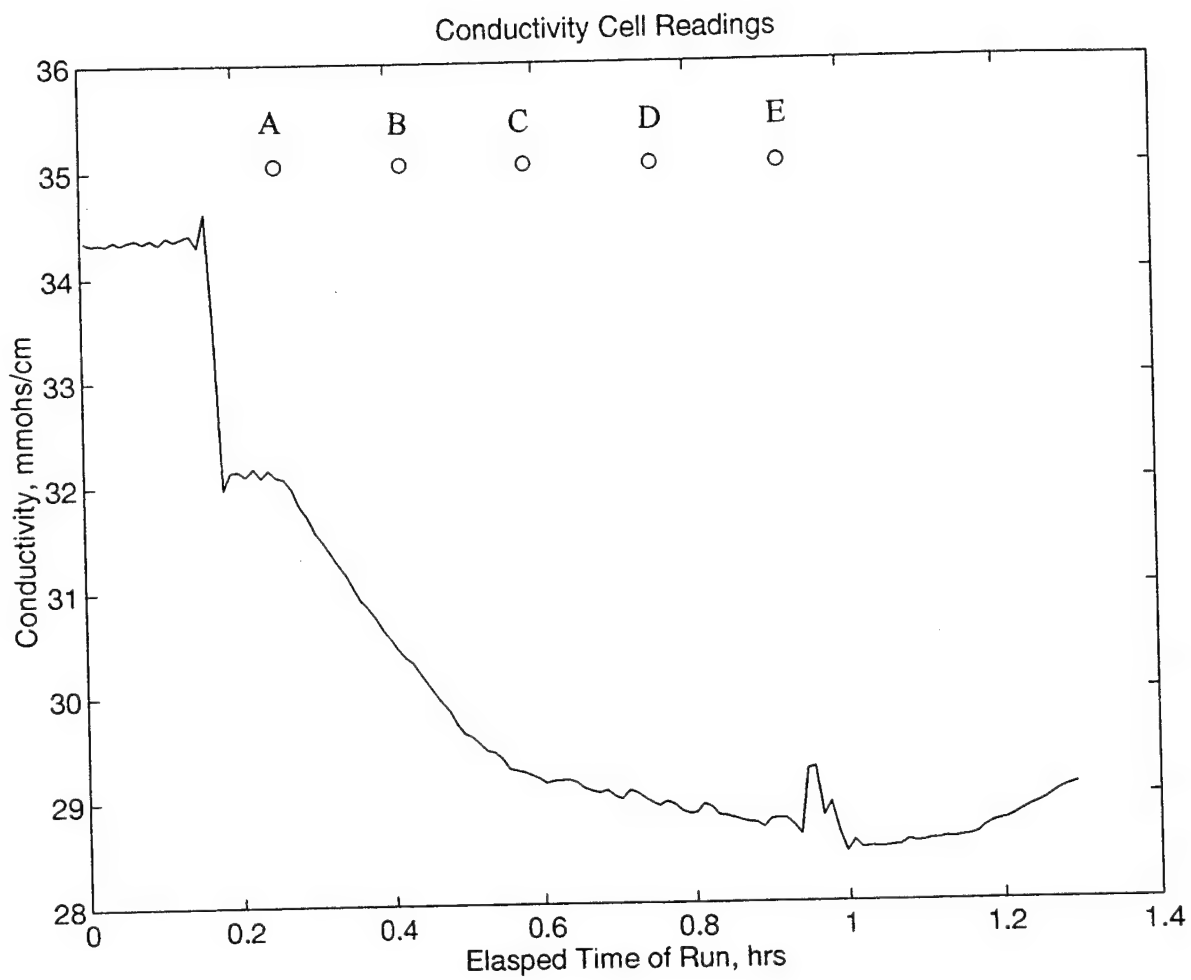


Figure (28). Conductivity Cell Results, 07 August 95

## E. BUBBLE PRODUCTION AND SPECTRA RESULTS

To confirm that the bubble clouds in the test tank represented oceanic spectra, a large effort was made to determine the bubble spectra in the test vessel. The method for sizing bubbles was based on an accurate measurement of the size of the specular "hotspot" on the bubbles surface (see Section II.B.8). From Baldy and Bourguet [1985], the relationship of this specular "hotspot" and the size of the bubble is

$$d_{\text{hotspot}} = 0.06 d_{\text{bubble}}$$

Equation (33)

A major limitation of this method was the finite resolution imposed by the camera pixel size. A calibration of the camera and microscope was made by imaging a target within the test vessel, with results shown in Table (18).

Target Width	Frames Imaged	Mean Target Width	Conversion
0.55 cm	75	333 pixels	16.5 $\mu\text{m}$ / pixel

Table (18). Video Calibration Results

Using the relationship as given in equation (29), this would result in resolution of air bubbles only down to a radius of approximately 138  $\mu\text{m}$ . It was initially hoped that this method would resolve bubble sizes down to 10  $\mu\text{m}$  in radius. The lower limit of bubble radius was determined by the size of a single pixel, and the upper limit was restricted only by the nominal diameter of the laser beam. This resulted in an upper limit of over 2900  $\mu\text{m}$  in radius, with bubbles of larger radius being measured as having a 2900  $\mu\text{m}$  radius. Regardless of these restrictions, however, a portion of the bubble size spectrum should still have been resolved using this method, allowing comparisons of bubble spectra produced within the test vessel with measured ocean spectra reviewed in Sections II.B.1 and 2.

Figure (29) shows results of fresh water bubble production, while Figures (30) through (33) show results of salt water bubble production. Table (19) shows experimental results used in these plots. Bubble size spectral density,  $n(a)$ , (bubbles / radius / meter<sup>3</sup>), is shown as a function of bubble radius. Spectral density is determined by the relationship

$$n(a) = \frac{N}{da * V * i}$$

Equation (34)

where  $N$  is the number of bubbles of a given radius,  $da$  is the radius increment,  $V$  is the sample volume and  $i$  is the number of frames of data which were processed. These plots also depict results published by Cartmill and Su [1993] for comparison. The most notable difference between these data sets is that our laboratory spectral densities are larger by over two orders of magnitude. This suggests that the bubble population in our experiments are far higher than the open ocean measurements reported in the literature. Additionally, the very small sample volume ( $4.247 \times 10^{-9} \text{ m}^3$ ) limits the minimum number of objects of a given radius illuminated during an experimental run. If a single bubble is detected within the sample volume during an experimental run, the bubble population automatically contains 10,000 bubbles  $\text{m}^{-3}$ , when the sample is normalized to a cubic meter. This is clearly shown in Figure (30) which shows a single data point at 1400 microns radius. This plot shows the particle size spectrum present within the vessel prior to bubble production. It is likely that a single suspended particle was present, was illuminated and counted by the sizing routine and became represented as  $10^4$  particles upon normalization. The measurements do, however, show that the observed bubble size spectral levels are much higher than the open ocean values measured by Cartmill and Su [1993], and yet visually better represent bubble densities lighter than those observed in the surf zone.

Date / Nozzle	Water Type	Threshold Level	Frames Imaged	Objects Sized
16 Jun / 1.0	Fresh	25	1793	4376
16 Jun / 2.0	Fresh	25	631	2111
03 Aug / 0.5	Salt	25	1053	2694
03 Aug / 1.0	Salt	25	1054	2572
03 Aug / 1.5	Salt	25	1053	2747
03 Aug / 2.0	Salt	25	1053	2733
07 Aug / 0.5	Salt	25	1059	1130
07 Aug / 1.0	Salt	25	1059	1664
07 Aug / 1.5	Salt	25	1060	1665
07 Aug / 2.0	Salt	25	1058	1591

Table (19). Video Bubble Image Data

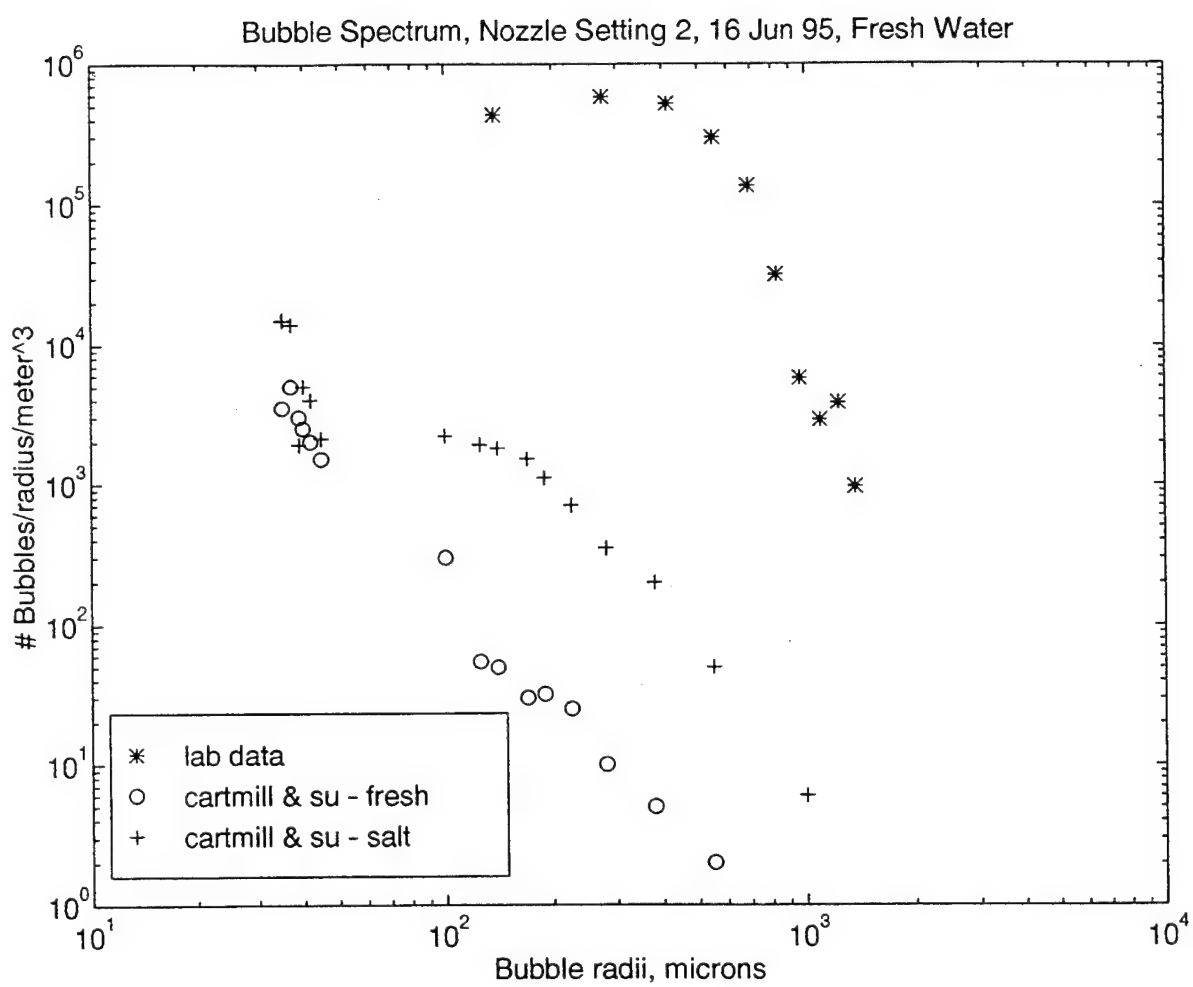


Figure (29). Freshwater Bubble Spectrum

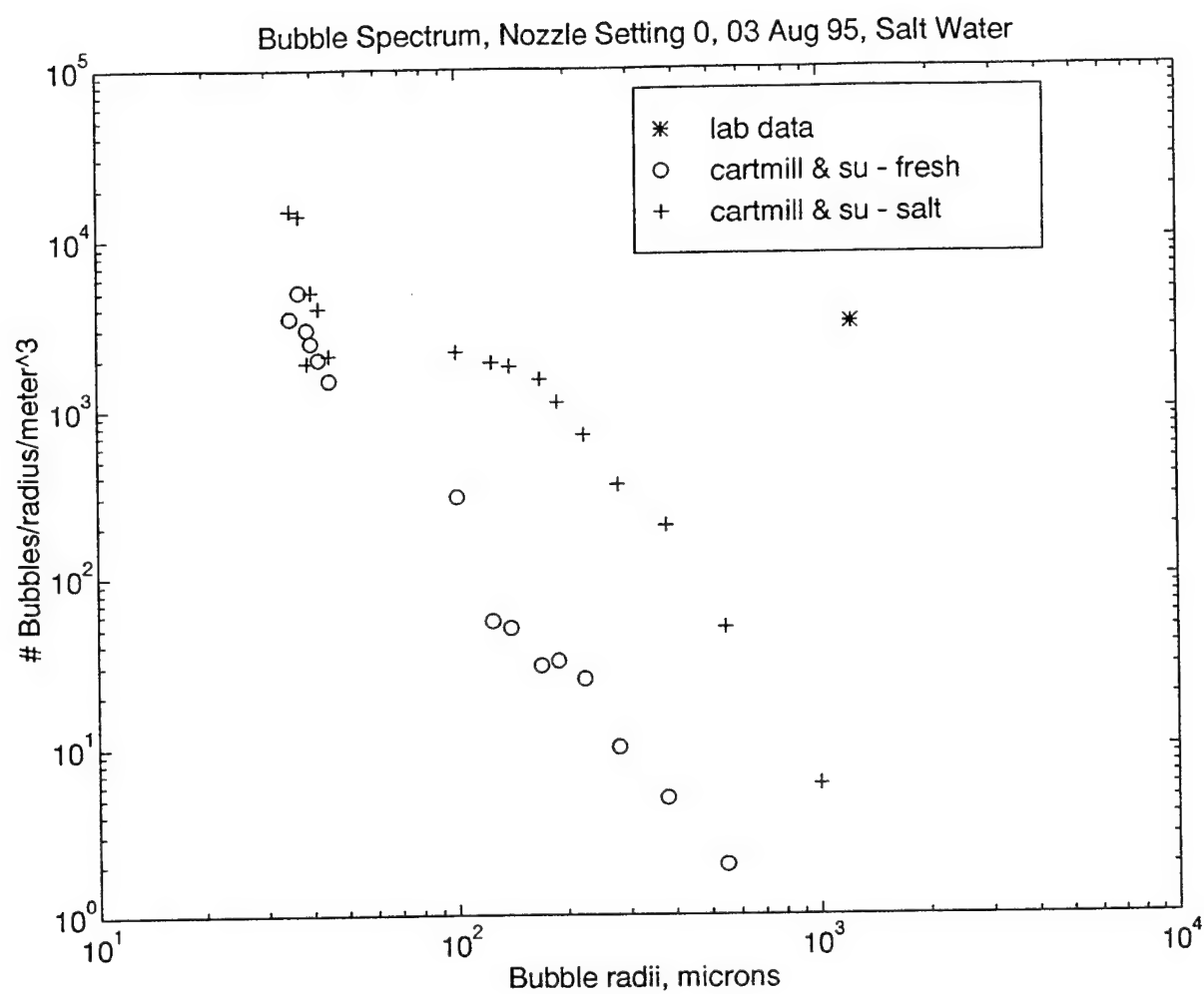


Figure (30). Saltwater Bubble Spectrum, 03 August, No Bubble Production

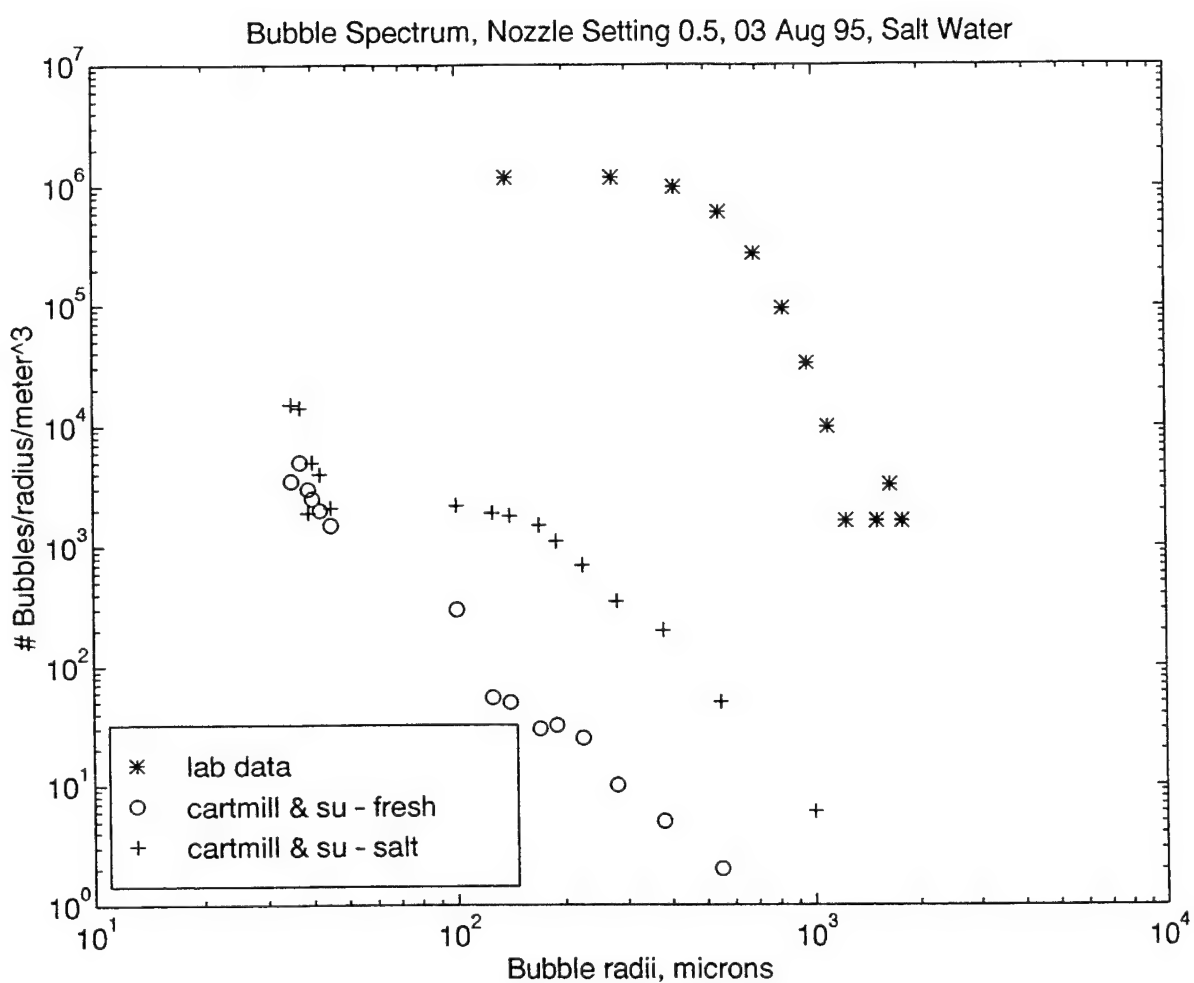


Figure (31). Saltwater Bubble Spectrum, 03 August, Minimum Flow

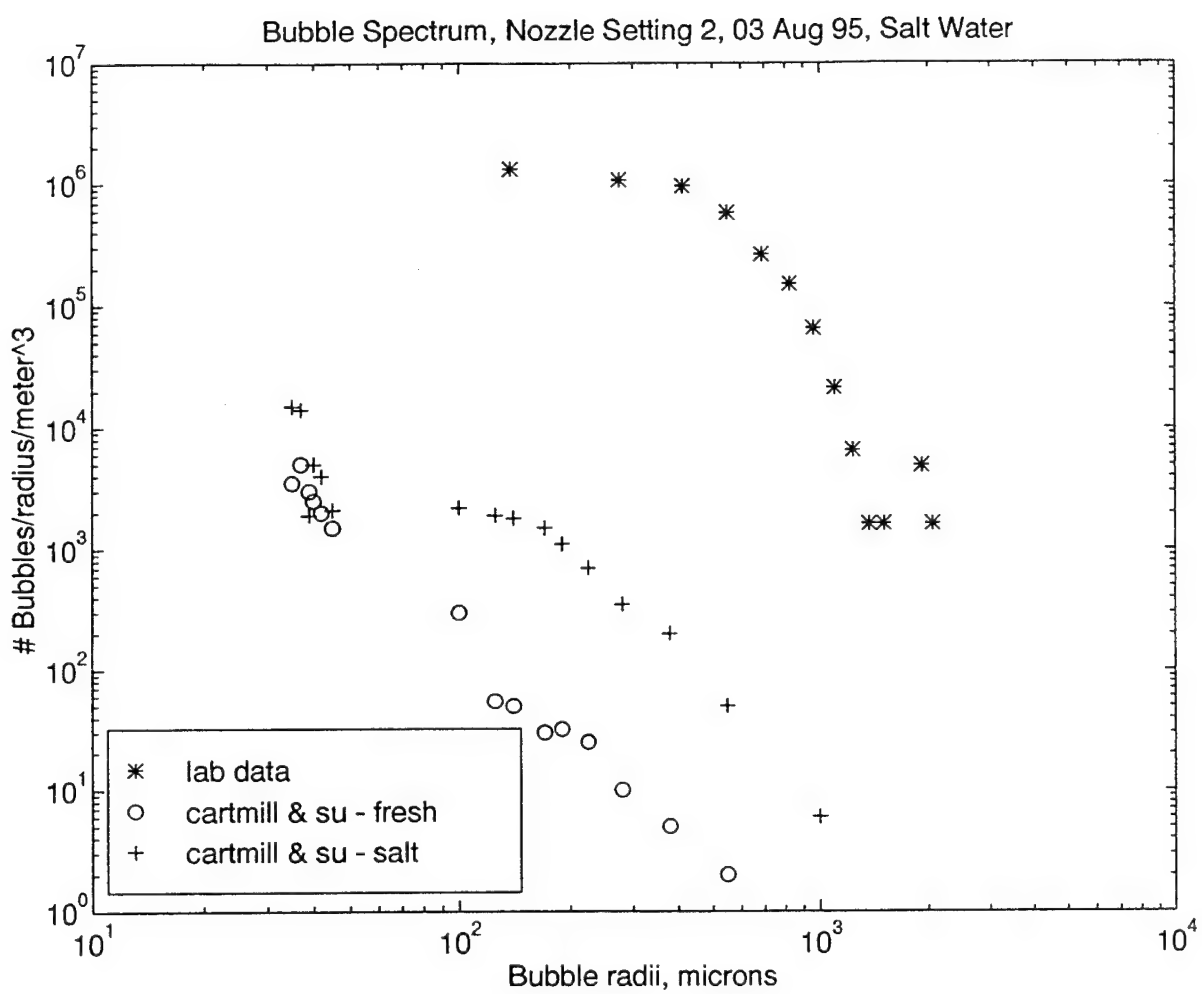


Figure (32). Saltwater Bubble Spectrum, Maximum Flow

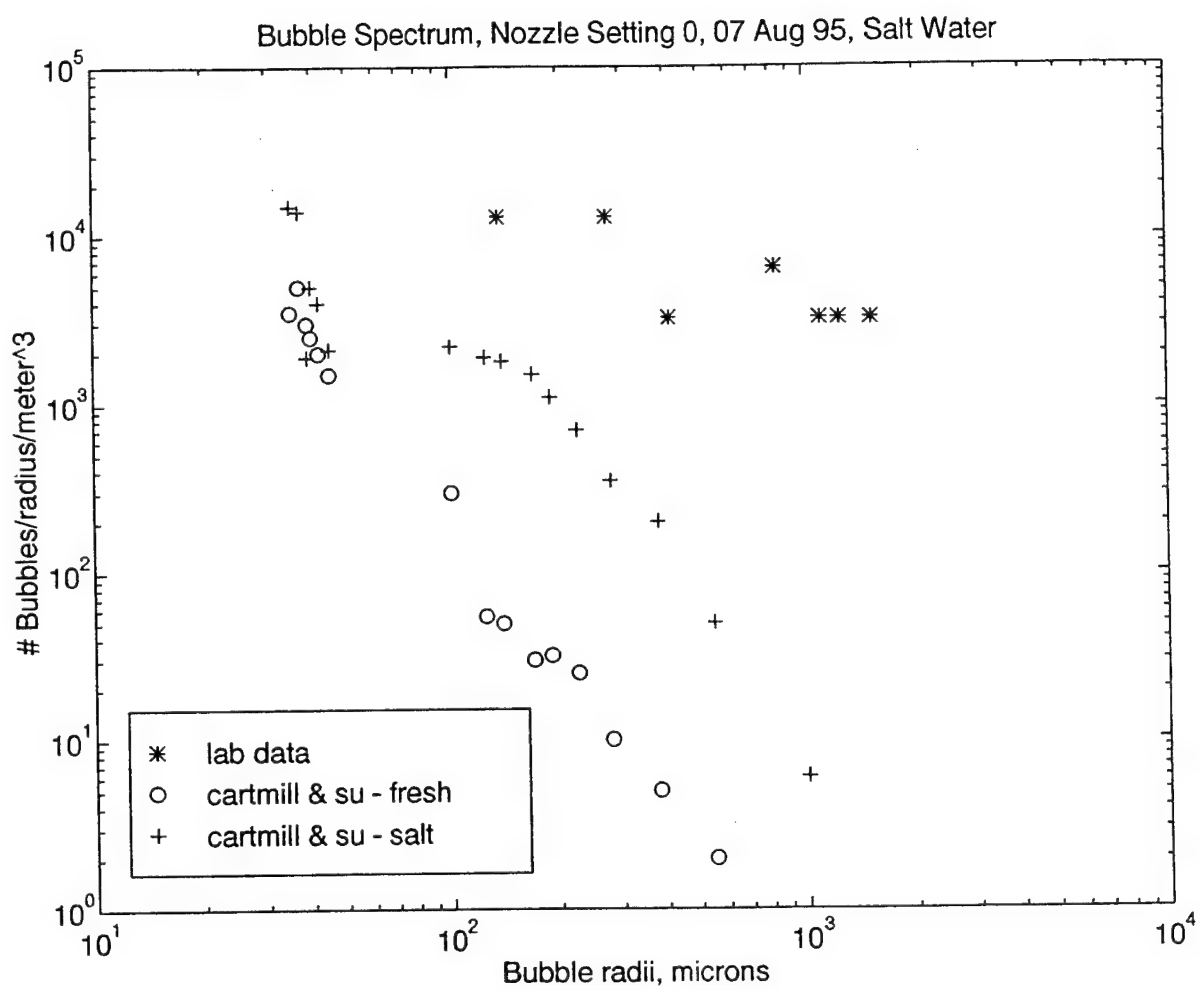


Figure (33). Saltwater Bubble Spectrum, 07 August, Still Conditions

The most disturbing aspect of the laboratory measurements shown in Figures (29), (31) and (32) is that the slope of the curve in all runs is much steeper than that of Cartmill and Su. This is probably an artifact of the measurement method. Despite the choice of an HAD, CCD camera, extremely bright pixels could "bleed" over into adjacent pixels, making the imaged hotspot larger than it is. This phenomenon will be more prevalent in smaller bubbles than in larger ones, and would have the effect of steepening the curve in the region of smaller radii, producing the shape shown. Corruption of spectral data is also apparent in Figure (33) which shows still water conditions with no bubble production and quite a few suspended particles within the vessel. These particles, which could have been biotics produced in the tank during a weekend, could have had an adverse effect on conductivity readings and corresponding void fraction estimation.

## **F. ACOUSTIC DATA**

Coherent Acoustic Sediment Flux Probe data was used to determine the effects of the bubble cloud within the test vessel upon a transmitted acoustic signal. As discussed in Chapter IV, the scattering strength of the bubbles within the test vessel is a function of their geometric cross section integrated over the population's distribution. For this reason, it was expected that the strength of the backscattered energy would be greater with more bubbles in the vessel, and that the attenuation of the CASP signal through the cloud would increase. This was borne out through analysis of the data obtained during the two salt water experiments.

### **1. Backscattered Energy**

The amplitude of the acoustic energy received by the CASP, which is backscattered by the bubble population resident within the test vessel, is dependent upon the scattering

strength (effective cross section) of the bubble population. It was initially hoped that the optical measurement methods employed during these experiments coupled with the bubble sizing algorithm would provide a quantitative basis for determining the effects of the produced bubble size spectra on the backscattered energy. Due to the fact that the optical measurement method and conductivity cell did not function as well as planned, no quantitative verification of the size spectrum was available. As a result, backscattered energy could only be analyzed in terms of the backscatter level, attenuation at two frequencies and the optical backscatter levels without explicit knowledge of the test bubble size spectrum in an effort to determine an attenuation coefficient within the vessel. Figures (34) and (35) show backscattered energy levels at the front and back of the vessel, respectively, for 03 August experimental runs, for nozzle settings A through E. Figures (36) and (37) show similar data for 07 August experimental runs. Energy levels recorded at the front of the vessel are of higher magnitude and display much more distinct changes when bubble production rates are increased. At back wall of the vessel, CASP signal strength is attenuated by the bubble cloud so that raw backscattered levels are nearly constant, regardless of the bubble population. Attenuation results will be discussed in the next section.

## **2. Attenuation**

Acoustic attenuation effects were discussed in Chapter IV. Attenuation coefficients,  $\alpha$ , for each separate bubble population produced was determined as a function of range

within the test vessel. Acoustic pressure as a function of range,  $P(r)$ , is given by the equation

$$P(r) = P_o \left( \frac{r_o}{r} \right) e^{-(\alpha_w + \alpha_s) \Delta r}$$

Equation (35)

where  $P_o$  is the reference acoustic pressure taken at the first bin inside the test vessel. The reference range,  $r_o$  is also taken as the first bin inside of the vessel, while the range,  $r$ , runs from the front to the back of the vessel. For both of these values, the bins containing the walls of the vessel were not used in the calculation. The attenuation coefficient for water,  $\alpha_w$  is a predetermined quantity based on the density of the water and frequency in use. The attenuation coefficient due to the presence of scatterers,  $\alpha_s$ , is given by the relationship

$$\alpha_s = -(\ln(\frac{P}{P_o} + \frac{r}{r_o}) + \alpha_w)$$

Equation (36)

A least squares fit of these data points produced a line whose slope is the attenuation coefficient for that particular population. Table (20) shows a summary of the attenuation values obtained.

Point Indicator	03 August	07 August
A	4.755	4.139
B	12.63	5.222
C	14.51	6.79
D	14.85	7.445

Table (20). Attenuation Coefficients

This data clearly shows that for runs 3 and 4, there is very little difference in the bubble population resident within the test vessel. Comparison with the attenuation curve obtained using the bulk backscattering model in Chapter IV shows a reasonably good agreement given the bubble spectral density used in the model (shown in Table (7)).

### **3. Suspended Sediment Attenuation Comparison**

Kohanowich [1995], during studies of acoustic attenuation due to suspended sediment, confirmed that attenuation of the CASP signal at 1.3 MHz was linearly dependent upon the concentration of scatterers present within the test vessel according to the following relationships

$$\alpha_s = -0.0857 \frac{m^{-1}}{(g/l)}$$

Equation (37)

and the received acoustic power at the 1.3 MHz transceiver was related to the concentration of sediment in grams / liter (up to a concentration of 725 gm / l) is

$$5.2 \times 10^{-8} (g/l) / \text{counts}^2$$

Equation (38)

Therefore, it is a simple matter to determine a sediment concentration which would be required to produce an attenuation coefficient equivalent to those measured due to the presence of bubbles. Results of these calculations are shown in Table (21).

Date / Point Indicator	Attenuation Coefficient, $\alpha_s$	Counts <sup>2</sup> (x 10 <sup>8</sup> )	Equivalent Sediment Concentration, (g/l)
03 August / A	4.755	0.913	4.75
B	12.63	4.29	18.02
C	14.51	6.15	31.98
D	14.85	6.3	32.76
07 August / A	4.14	0.47	2.44
B	5.22	1.71	8.89
C	6.79	2.58	13.42
D	7.45	2.6	13.52

Table (21). Suspended Sediment Equivalence

As can be seen from the above data, even high bubble concentrations, as were produced during experimental runs 3 and 4, are equivalent to relatively low concentrations of sediment. In open ocean measurements, Lamarre and Melville [1992] found void fractions near the surface of breaking waves to be greater than 0.3 %. In the surf zone, void fraction near the surface of breakers could reasonably be expected to be much higher. This value would attenuate rapidly with depth, while the concentration of entrained sediment would increase to a maximum near the bottom. In a position within the water column where both bubbles and sediment are present, the majority of backscatter received by the CASP would be from entrained sediment. Figure (38) shows two plots, both of which compare the attenuation effects of bubbles and sediment. In each plot, \*'s denote laboratory measurements, the solid line is a linear least squares fit of this data, and the dotted line show attenuation information obtained using equations (33) and (34) for entrained sediment.

Clearly, the difference in the slopes indicate that a discriminator could be developed to determine the difference in backscatter levels due to the presence of both air bubble and sediment scatterers with the surf zone.

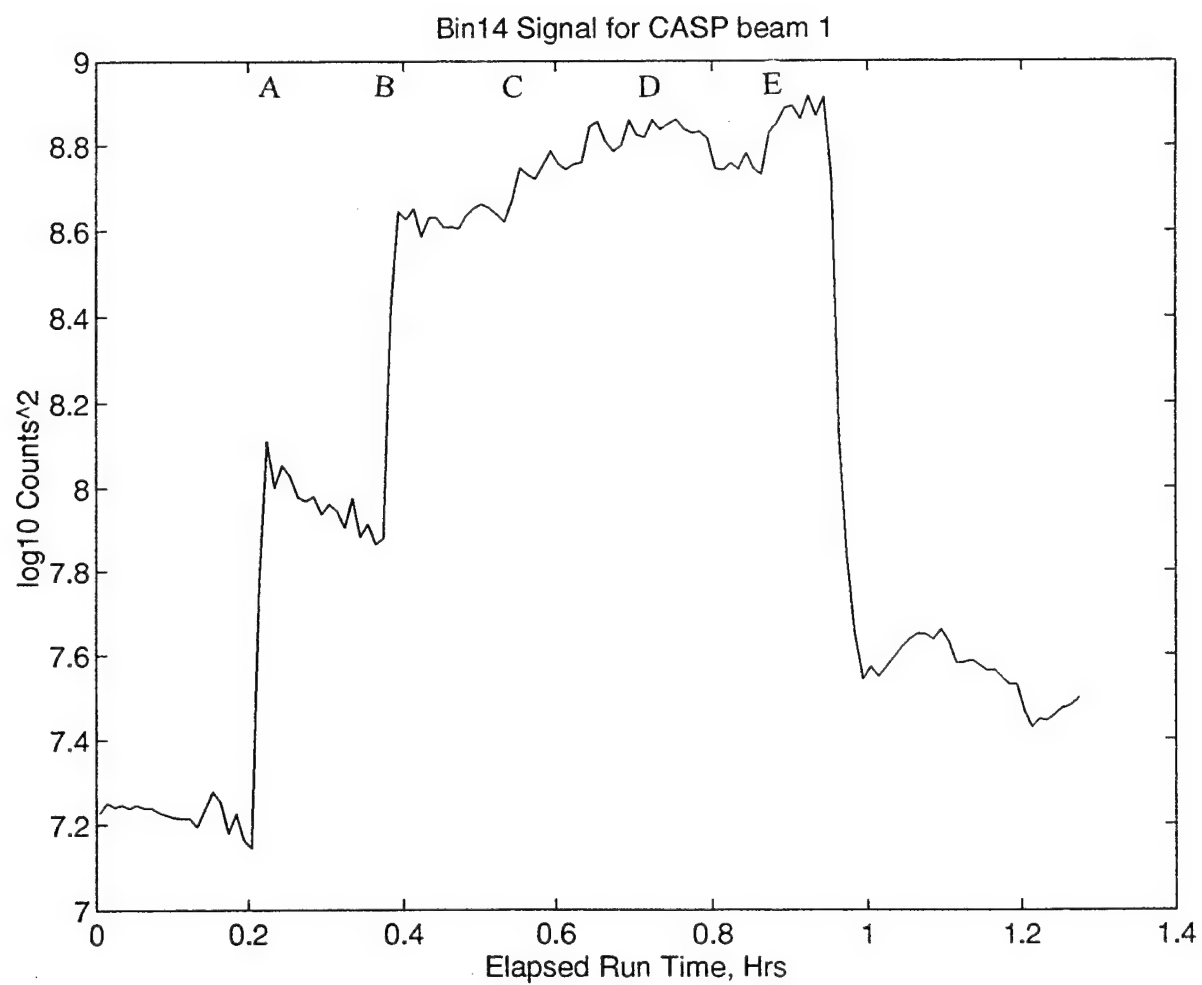


Figure (34). Backscattered Energy, Front of Vessel, Bin 14, 03 August  
Seawater, Nozzle Settings A - E

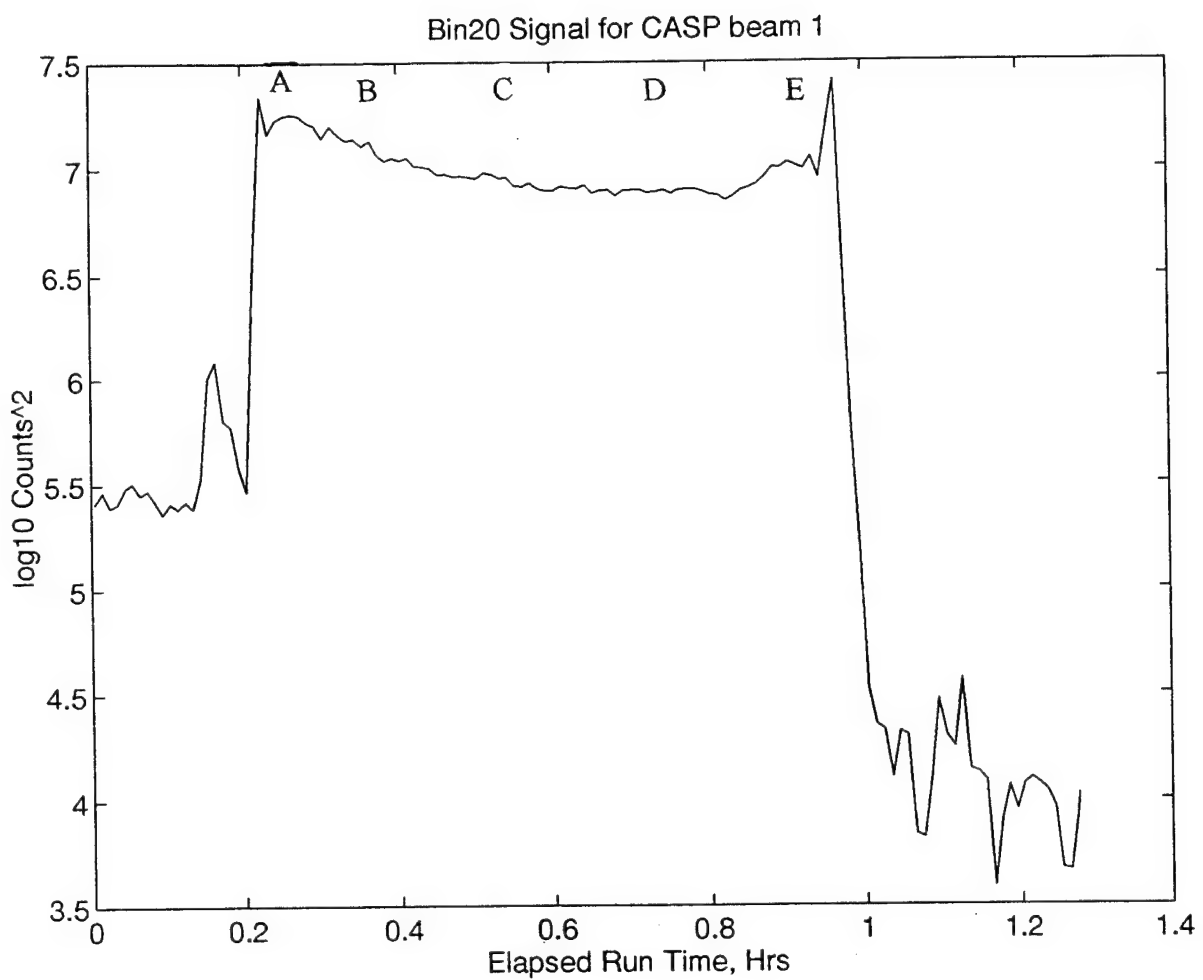


Figure (35). Backscattered Energy, Back of Vessel, Bin 20, 03 August  
Seawater, Nozzle Settings A - E

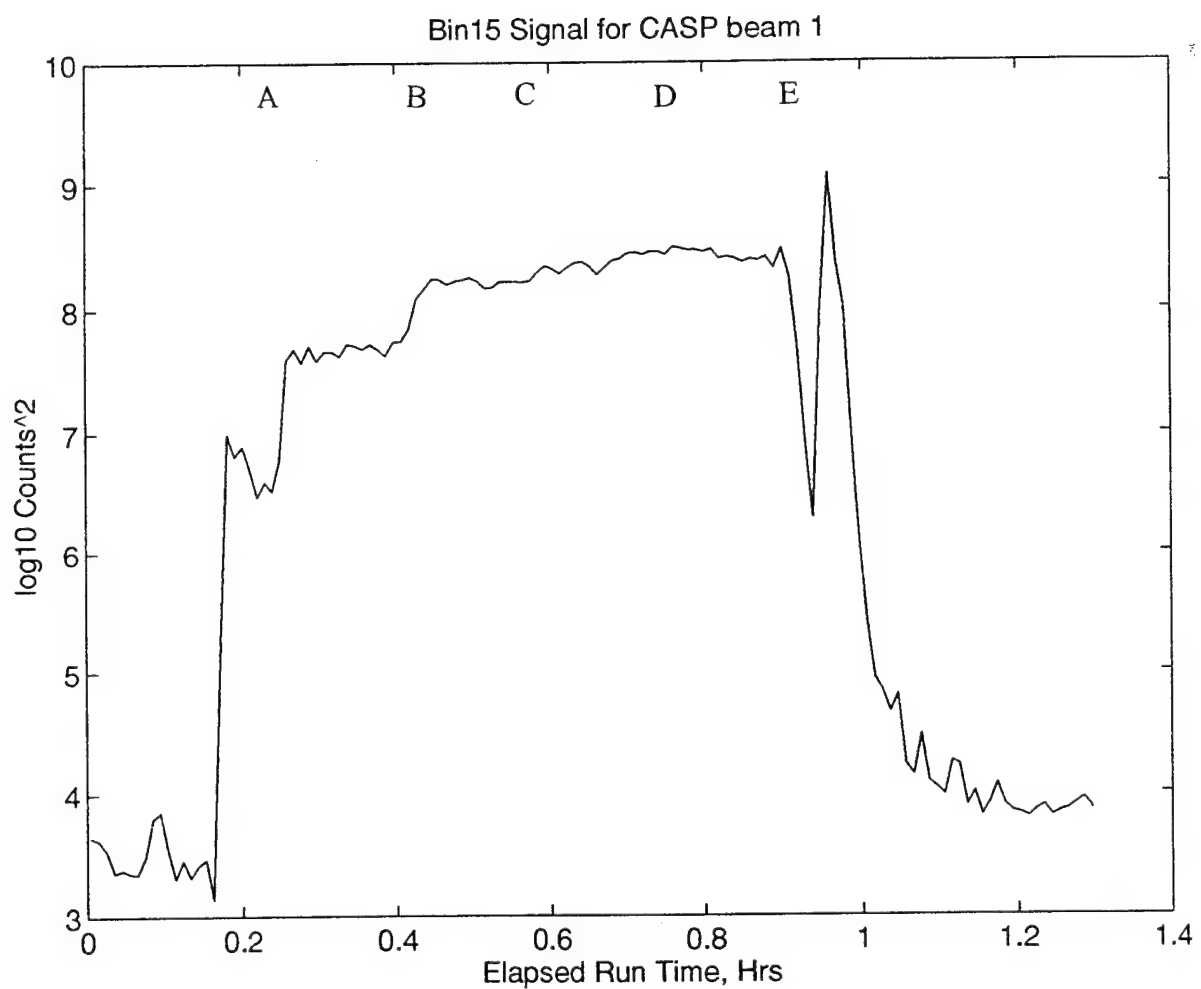


Figure (36). Backscattered Energy, Front of Vessel, Bin 15, 07 August  
Seawater, Nozzle Settings A - E

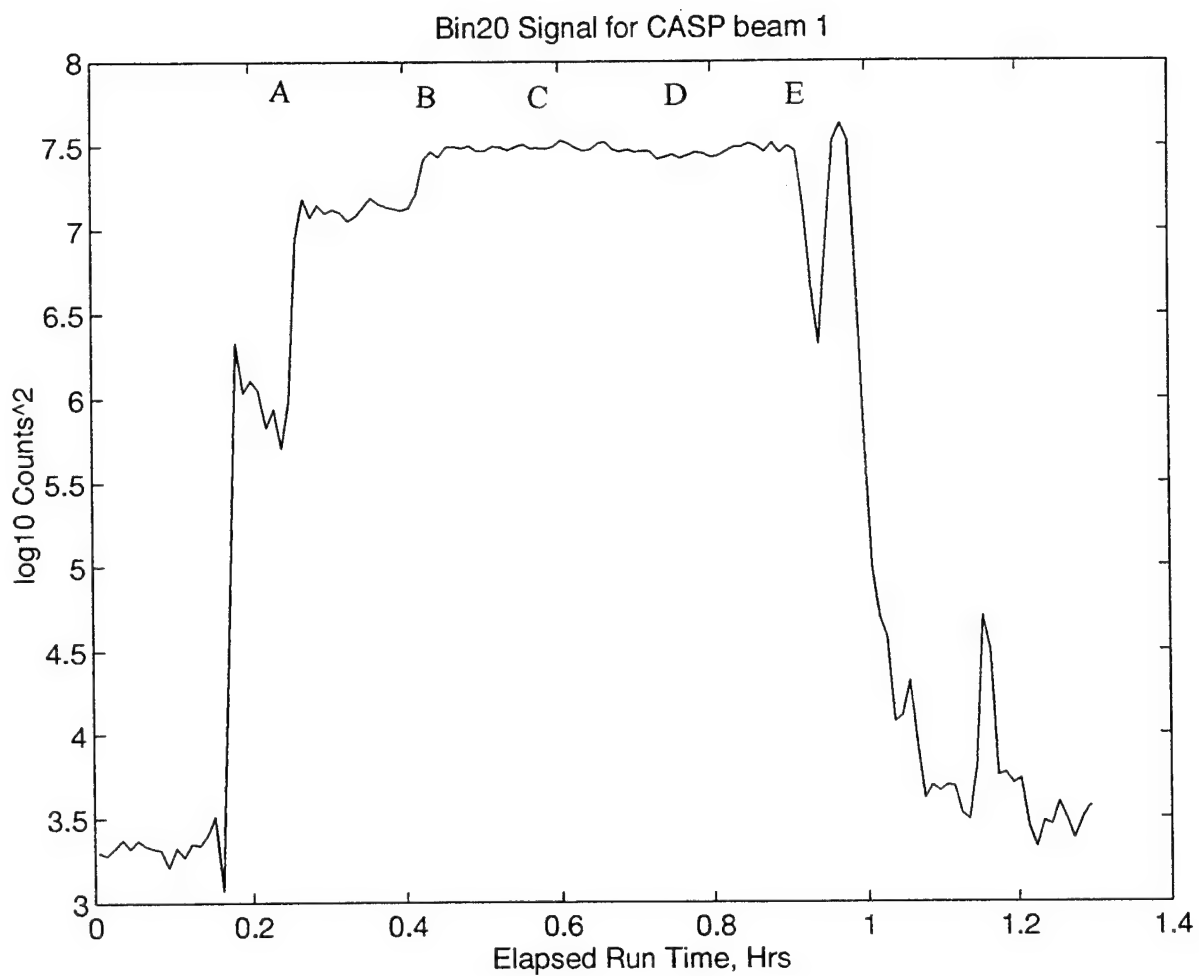


Figure (37). Backscattered Energy, Back of Vessel, Bin 20, 07 August  
Seawater, Nozzle Settings A - E

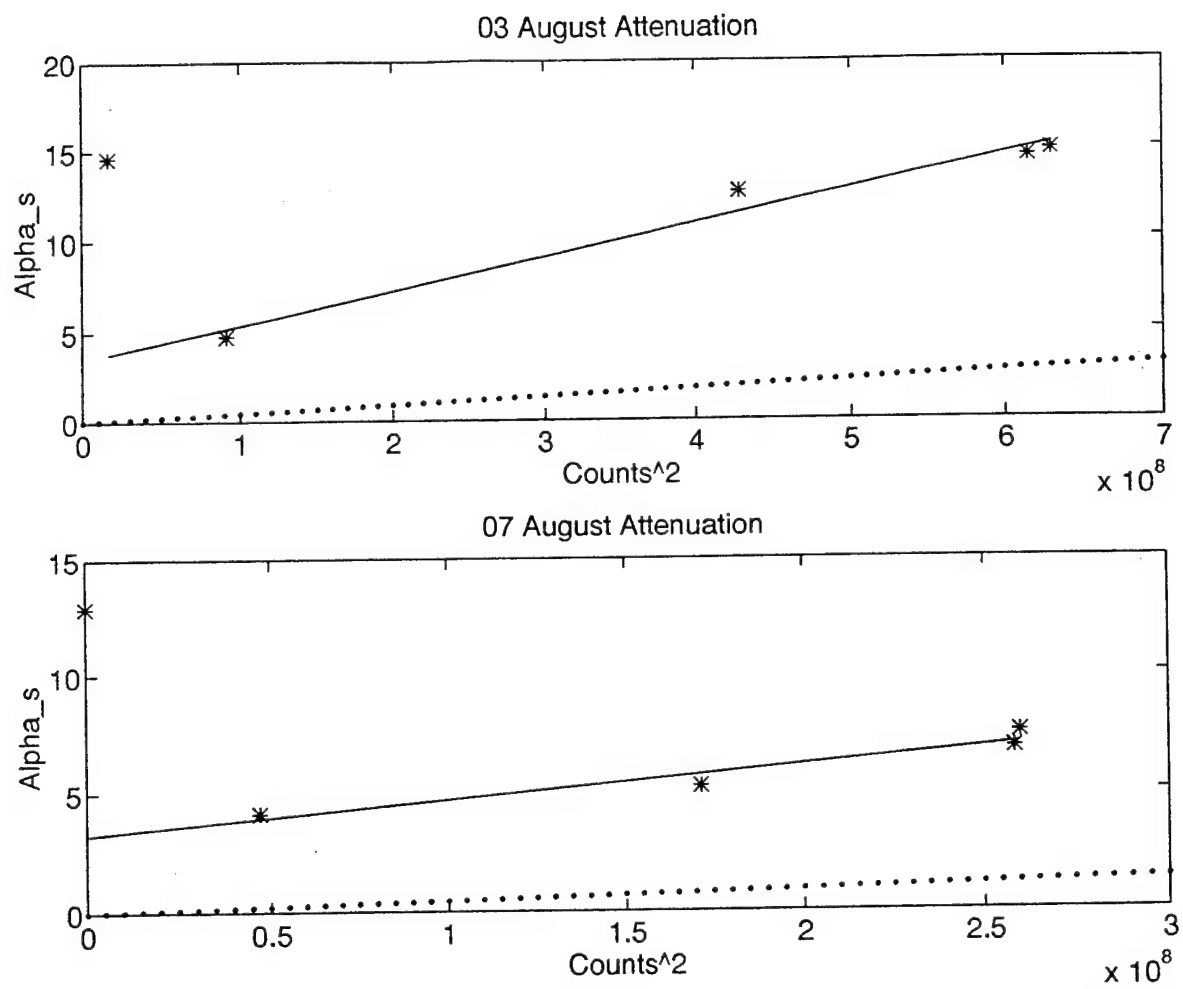


Figure (38). Attenuation Comparison

## VII. CONCLUSIONS

The initial goal was to develop a means by which a bubble population within a test vessel could be accurately counted and sized in order to produce a spectral density similar to that which could be reasonable expected to be encountered in the surf zone, although there were no surf zone observations with which to compare. This representative population would then be utilized to determine the ultrasonic backscatter characteristics of different bubble densities. This data would allow further determinations to be made concerning a method to discriminate between the signal produced by acoustic energy scattered from suspended sediment and the signal scattered by entrained bubbles. The development of this method of measurement was hampered by several influences. Time constraints, complexity and availability of measurement apparatus, and the physical restriction imposed by laboratory equipment all played significant roles in not only the selection of equipment to be used, but also the eventual end of the experimental process.

A significant effort was made to utilize both optical measurement methods and void fraction measurements to assess the bubble population produced within the test vessel. At very low bubble densities, optical measurement methods are very accurate and the data is simple to analyze. As demonstrated during single bubble production testing, measurement and counting of the produced bubbles using laser illumination and video image analysis was quite easy. Bubbles of the size range which are expected to be encountered in the surf zone effect the conductivity of the water they are suspended in only when taken as a bulk measurement. Individually, they are not large enough to have a significant effect on the conductivity. At high bubble densities, regardless of the bubble spectra, conductivity cells function well, and changes in spectral density can be detected. High spectral densities, however, have the effect of making the water nearly opaque, rendering optical measurement methods ineffective. In order to use both of these methods together in the same volume, a "middle ground" spectral density had to be produced that would allow a low enough bubble

density for the use of laser optics to measure the individual bubbles, yet high enough for void fraction to be determined using conductivity. This was nearly accomplished.

The chosen method of bubble production, above water jet entrainment, produced, at least visually, a reasonable bubble spectrum. In view of the shortcomings of the method of measurement, however, this spectrum could not be verified quantitatively.

The method of bubble measurement used appeared to have the ability to measure and size individual bubbles accurately, however, it proved to have one major drawback when used to determine spectral density. Geometrical optical approximations are a well accepted means of determining the size of air bubbles in water, but the extremely small sample volume presented by the laser and camera apparatus used limited the smallest number of objects measured during an experimental run. Additionally, the potential "smearing" of pixels as presented in video images of illuminated bubbles may have induced errors in the measured size of the "hotspots" produced on very small bubbles. Although this method was only capable of sizing bubbles down to 140  $\mu\text{m}$ , this was not viewed as a limitation. Theoretically, this method should still have been capable of resolving some portion of published spectral measurements which were used as a benchmark for this experiment. Limitations imposed by the small sample volume and the resolution capabilities of the video equipment prevented this.

Qualitative analysis of void fraction results showed that although the bubble density was apparently altered through control of the flow through the jet, the equipment in use suffered some sort of malfunction which prevented accurately detecting subtle changes in void fraction. Calibration testing of the conductivity cell revealed very little difference in cell response for zero bubble conditions and saturation of the vessel with bubbles. This is regarded as significant in that variations in spectral density throughout experimental runs were visually quite different, but resulted in imperceptible changes in the conductivity of the medium as registered by the conductivity cell. Additional difficulties may have arisen due to the lack of a completely homogeneous bubble cloud and the restrictive physical

conditions of the vessel which prevented orienting the cell in a manner which would have allowed for free flow of bubbles through the center.

Acoustic backscatter results revealed nothing unusual. Studies of scattering strength and attenuation due to clouds of bubbles are well documented. This series of experiments produced results which did nothing more than validate theories and studies published by several investigators. One interesting result, however, was the validation that the Coherent Acoustic Sediment Flux Probe was quite capable of detecting relatively subtle changes in bubble density. the CASP proved to be far more sensitive than any of the other sensors used in these experiments.

Despite a significant effort, it is clear that the methods chosen for bubble measurement and counting were not the best methods available. From the outset, it was felt that an Acoustic Resonator Array would be the simplest, most accurate and least invasive of previously published methods available. Unfortunately, efforts to obtain or manufacture a resonator proved to be too difficult. In addition to this, the size of the test vessel precluded the use of an array large enough to have a sufficient measurement range of bubble radii. Further efforts in this area should include the use of an acoustic resonator in concert with a conductivity cell.



## APPENDIX A. SPECIFICATION SHEET FOR OPTICAL BACKSCATTERANCE SENSORS

### OBS-3 & OBS-3B SUSPENDED SOLIDS & TURBIDITY MONITOR

#### FEATURES

OBS-3 monitors have field-proven Optical BackScatterance (OBS<sup>®</sup>) sensors, low-power analog circuitry, and switch-selectable gains with fine adjustment. These self-contained sensors are ideal components for CTD's, water quality monitoring and process control systems and can monitor suspended matter in the clearest to most turbid waters in rivers, lakes, and the ocean.

The Model OBS-3 includes an underwater housing rated to 2,000 or 5,000 meters and is available with an optional 4 mA to 20 mA two-wire transmitter. A cable assembly is required to connect the Model OBS-3 to a power supply/data logger. Consult the manufacturer about your cable requirements.

The Model OBS-3B is designed for the system intergrator. It includes a threaded sensor with flexible, color-coded #30 AWG leads for connections to the circuit module. Color-coded #30 AWG leads are also provided for connecting the circuit module to an OEM power supply/data logger.

#### APPLICATIONS

- ▼ OEM component in oceanographic, water quality, and process-control instrumentation
- ▼ Water and wastewater monitoring systems
- ▼ Laboratory measurements
- ▼ River gauging
- ▼ Sediment transport studies

#### SPECIFICATIONS

##### DYNAMIC RANGES

Turbidity	0.02 to 2,000 FTU <sup>1</sup>
Mud	0.1 to 5,000 ppm (mg/l)
Sand	2 to 100,000 ppm (mg/l)

##### FREQUENCY RESPONSE

10 Hz

##### AMBIENT LIGHT REJECTION

Optical filtering and synchronous detection

##### TEMPERATURE COMPENSATION

Solid state temperature transducer

##### NONLINEARITY<sup>2</sup>

Turbidity (formazin, 0 to 2,000 FTU)	2.0%
Mud (0 to 4,000 mg/l)	2.0%
Sand (0 to 60,000 mg/l)	3.5%

##### DRIFT

Time	< -3.5% in 1st 2,000 hrs
Temperature	0.05%/°C

##### SUPPLY VOLTAGE COMPLIANCE

250  $\mu$ V/V

##### SETTLING TIMES

Power-up	<1 s
----------	------

25 °C Step Change in Water

Temperature	15 s
-------------	------

##### OUTPUT SPAN

0 to 5 V

##### OUTPUT IMPEDANCE

< 300 Ohms

##### RMS NOISE AT 0 FTU

< 50  $\mu$ V

##### POWER REQUIREMENTS

+7 to 15 V/14 mA

##### OUTPUT FILTER

20 Hz (-3 dB)

##### PHYSICAL DIMENSIONS

Sensor	length	2 in (51 mm)
	diameter	0.7 in (18 mm)
Housing	length	4.5 in (115 mm)
	diameter	1.2 in (31 mm)
Weight	air	0.4 lb (0.17 kg)
	submerged	0.16 lb (0.07 kg)

##### WORKING DEPTH

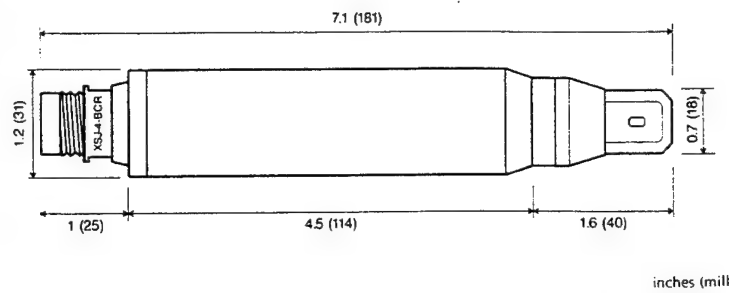
2,000 m or 5,000 m

<sup>1</sup> Formazin Turbidity Unit

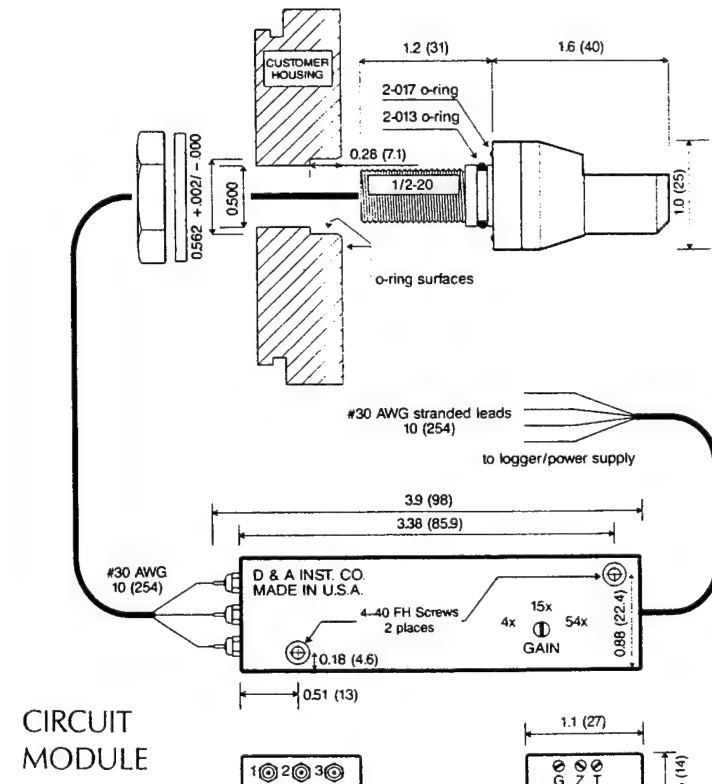
<sup>2</sup> Maximum deviation of response from a straight line, expressed as a percentage of the calibration range.

#### MECHANICAL DATA

##### OBS-3



##### OBS-3B SENSOR



##### CIRCUIT MODULE

1 Coaxial Shield	4 Detector (Coaxial lead)	G Gain
2 Common (green)	5 Temperature Sensor (orange)	Z Offset
3 IRED Anode (red)	6 IRED Cathode (brown)	T Temperature Coe

inches (mm)

DELIVERY: 3 WEEKS ARO

TERMS: COD (except with prior credit approval)



40-A Seton Road  
Port Townsend, WA 98368  
Phone: 800-437-8352  
(206) 385-0272  
Fax: (206) 385-0460



## APPENDIX B. SPECIFICATION SHEET FOR CONDUCTIVITY CELLS

### SPECIFICATIONS MEASUREMENT:

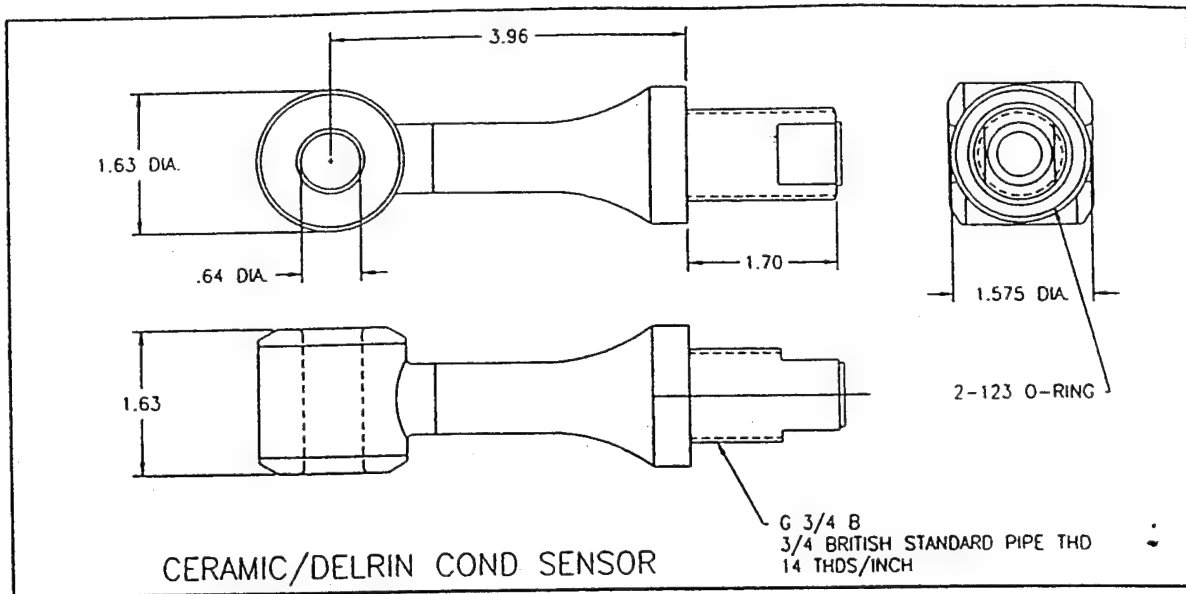
CONDUCTIVITY:	RANGE 0 -> 64 mmho/cm (0 -> 6.5 S/m) ACCURACY +/- .025 mmho/cm (.0025 S/m) STABILITY +/- .005 mmho/cm/month (.0005 S/m)
TEMPERATURE:	RANGE -5 -> 35 Celsius (ITS-90) ACCURACY +/- .050 Celsius STABILITY +/- .002 Celsius/Month

### SPECIFICATIONS ELECTRICAL & MECHANICAL:

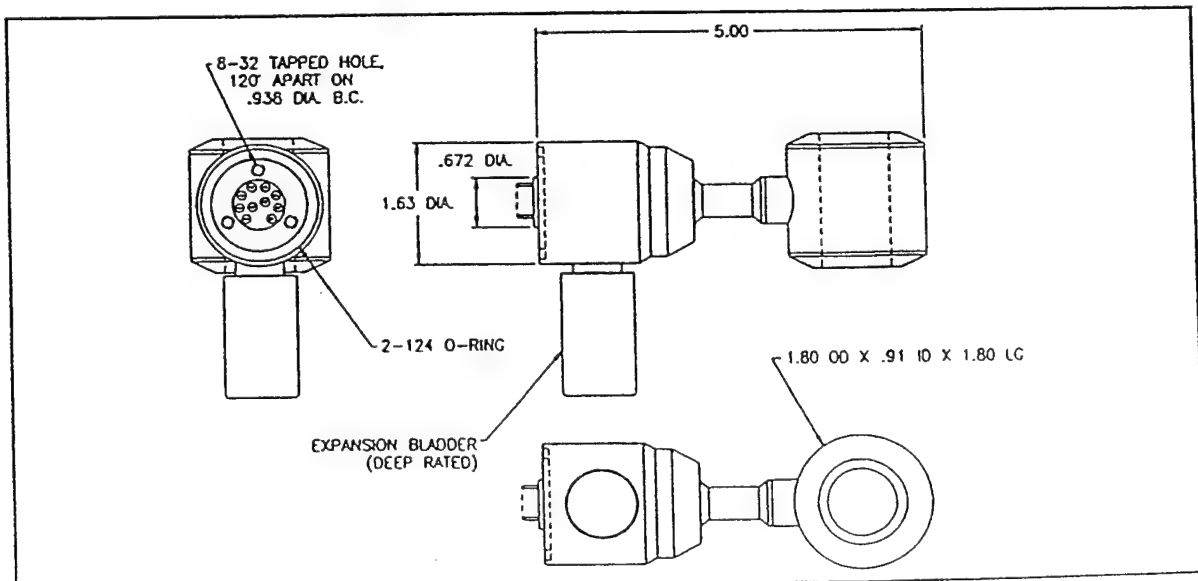
PROBES:	Falmouth Scientific Inductive Conductivity Sensor, Platinum Temperature Sensor
SIZE SENSOR: SIZE CARD:	Max. O.C. 45 mm LENGTH 163 mm Width 50.8 mm, Length 101.6 mm, Height 20 mm
MOUNTING:	3/4" B.S.P. (Witworth Thread)
O-RING:	2-123
MATERIAL:	Sensor (active area): Ceramic
OPERATING: PRESSURE:	1000 PSIA (650 dBAR) ABSOLUTE MAXIMUM
POWER: POWER:	5 VDC +/- 10% JUMPER J1 INSTALLED 7 - 14 VDC JUMPER J1 REMOVED LOAD CURRENT @ 5 mAmps
WARMUP:	100 mSeconds from power up
SAMPLING:	100 mSeconds Between Channel Selections
TIME CONSTANT	10 mSecond Conductivity, 100 Seconds Temp.
CONNECTOR:	Molex 6 Position Housing Type #2695
INPUT LOGIC:	VinL < 0.8 VDC VinH > 1.5 VDC Vmax 5.5 VDC
OUTPUT:	0 -> 2.5 Volts Nominal **

\*\* Consult factory for optional output voltage ranges.

## SENSOR OUTLINE DRAWINGS



## STANDARD C-T SENSOR



LARGE CONDUCTIVITY ONLY (EXTERNAL TEMP) SENSOR

## LIST OF REFERENCES

Anderson, W. J., Calibration and Sediment Load Algorithms for an Acoustic Sediment Flux Probe, Naval Postgraduate School Thesis, 1994.

Baldy, S., and M. Bourguet, 'Measurements of Bubbles in a Stationary Field of Breaking Waves by a Laser-Based Single Particle Scattering Technique', Journal of Geophysical Research, Vol 90, No C1, pp 1037-1047, 1985.

Bowyer, P. A., 'The Rise of Bubbles in a Glass Tube and Spectrum of Bubbles Produced by Splash', Journal of Marine Research, Vol. 50, pp 521-543, 1992.

Breitz, N., and H. Medwin, 'Instrumentation for in situ measurements of bubble spectra under breaking waves', Journal of the Acoustical Society of America, (2), pp 739-743, 1989.

Cartmill, J. and M.Y. Su, 'Bubble size distribution under saltwater and freshwater breaking waves', Dynamics of Oceans and Atmospheres, Elsevier Science Publishers, New York, pp 25-31, 1993.

Dolan, R. and H Lins, 'Beaches and Barrier Islands', Scientific American, July, 1987.

Farmer, D. M., and S. Vagle, "Waveguide propagation of ambient sound in the ocean surface bubble layer", Journal of the Acoustical Society of America, Vol. 86, pp 1897-1908, 1989.

Glantschnig, W. J. and S. Chen, 'Light scattering from water droplets in the geometrical optics approximation', Applied Optics, Vol 20, pp 2499-2509, 1981.

Glotov, V.P., P. Kiolovayev, and G. C. Neuimin, 'Investigation of the scattering of sound by bubbles generated by an artificial wind in sea water and the statistical distribution of bubble sizes', Soviet Physics - Acoustics 7, pp 341-345, 1962.

Haines, M. and B. Johnson, 'Injected bubble populations in seawater and freshwater measured by a photographic method,' Journal of Geophysical Research, Vol 100, C4, pp 7057-7068, 1995.

Halliday, D., R. Resnick and J. Walker, Fundamentals of Physics, fourth ed., John Wiley & Sons, N.Y., pp 1012-1020, 1993.

Holve, D. and S. A. Self, 'Optical particle sizing for in situ measurements, 1,2', Applied Optics, Vol 18, pp 1632-1658, 1979.

Johnson, B. D. and R. C. Cooke, 'Bubble Populations and Spectra in Coastal Waters: A Photographic Approach', Journal of Geophysical Research, Vol 84, pp 3761-3766, 1979.

Kinsler, L. E., A. R. Frey, A. B. Coppens, and J. V. Sanders, Fundamentals of Acoustics, John Wiley and Sons, New York, 1982.

Koga, M., 'Bubble Entrainment in Breaking Waves', Tellus 34, pp 481-489, (Munksgaard, Copenhagen), 1982.

Kolovayev, D. A., 'Investigation of the Concentration and Statistical Size Distribution of Wind Produced Bubbles in the Near-Surface Ocean', Oceanology, english translation, Vol 15, pp 659-661, 1976.

Lamarre, E. and W. K. Melville, 'Instrumentation for the Measurement of Void-Fraction in Breaking Waves: Laboratory and Field Results', IEEE Journal of Oceanic Engineering, Vol. 17, No. 2 , 1992.

Leighton, T. G., The Acoustic Bubble, Academic Press, New York, 1994.

Ling, S.C. and H. P. Pao, 'Study of Microbubbles in the North Sea', Sea Surface Sound, B. R. Kerman, ed, Kluwer Academic Publishers, pp 197-210, 1988.

Medwin, H., 'In Situ Acoustic Measurements of Bubble Populations in Coastal Ocean Waters', Journal of Geophysical Research, Vol 75, 599-611, 1970.

Medwin, H., 'In Situ Acoustic Measurements of Microbubbles at Sea', Journal of Geophysical Research, Vol 82, 971-975, 1977.

Medwin, H., and A. C. Daniel, jr., 'Acoustical measurements of bubble production by spilling breakers', Journal of the Acoustical Society of America, pp 480-492, 1990.

Medwin, H., and N. Breitz, 'Ambient and Transient Bubble Spectral Densities in Quiescent Seas and Under Spilling Breakers', Journal of Geophysical Research, Vol 94, No. C9, pp 12751-12759, 1989.

Monohan, E. C., J. P. Kin, M. B. Wilson and D. K. Woolf, "Oceanic whitecaps and the marine microlayer spanning the boundary separating the sub-surface bubble clouds from the aerosol laden marine atmosphere", Whitecap Report 3, Univ of Connecticut, 1987.

O'Hern, T. J., L. d'Agostino and A.J. Acosta, 'Comparison of Holographic and Coulter Counter Measurements of Cavitation Nuclei in the Ocean', Transactions of the ASME, Fluids Engineering, Vol. 110, 1988.

Physics of Sound in the Sea: Part IV, Acoustic Properties of Waves, Nat. Def. Res. Comm. Div. 6 Sum Tech. Rep. 8, pp 460-474, 1947.

Puttermann, S. J., 'Sonoluminescence: Sound into Light', Scientific American, pp 46-51, 1995.

Scott, J.C., 'The role of salt in whitecap persistence', Deep Sea Research, Pergamon Press, Vol 22, pp 653-657, 1975.

Stanton, T. P., The Coherent Acoustic Sediment Flux Probe, Naval Postgraduate School, 1993.

Su, M. Y., D. Todoroff and J. Cartmill, 'Laboratory Comparison of Acoustic and Optical Sensors for Microbubble Measurement', Journal of Atmospheric and Oceanic Technology, Vol 44, No 1, 1994.

Su, M.Y., S.C. Ling and J. Cartmill, 'Optical Microbubble Measurements in the North Sea', Sea Surface Sound, B.R. Kerman (ed.), Kluwer Academic Associates, 1988.

Van de Hulst, H. C., Light Scattering by Small Particles, John Wiley & Sons, N.Y., pp 220-222, 1957.

Walsh, A.L. and P. J. Mulhearn, 'Photographic Measurements of Bubble Populations from Breaking Waves at Sea', Journal of Geophysical Research, pp 14553-14565, 1987.

Wu, J., 'Bubble Populations and Spectra in Near Surface Ocean: Summary and Review of Field Measurements', Journal of Geophysical Research, Vol 86, No C1, pp 457-463, 1981.

Yamamoto, T., Y. Egawa, Y. Shirasawa, Y. Ozaki, K. Sato, Y. Yatomi, and K. Hume, 'A laser light scattering in situ system for counting aggregates in blood platelet aggregation', Measurement Science and Technology, Vol 6, pp 174-180, 1995.

## **INITIAL DISTRIBUTION LIST**

1. Defense Technical Information Center Cameron Station Alexandria, VA 2234-6145	2
2. Library, Code 52 Naval Postgraduate School Monterey, CA 93943-5002	2
3. Chairman, Department of Oceanography Code OC/Bo Naval Postgraduate School Monterey, CA 93943	1
4. Timothy P. Stanton Code OC/St Naval Postgraduate School Monterey, CA 93943	3
5. Dr. Edward B. Thornton Code OC/Th Naval Postgraduate School Monterey, CA 93943	2
6. LT Trevor A. McIntyre 300 Arloncourt Road Seaside, CA 93955	2
7. Library Scripps Institution of Oceanography University of California, San Diego La Jolla, CA 92093	1